

AARHUS UNIVERSITY

MASTERS THESIS

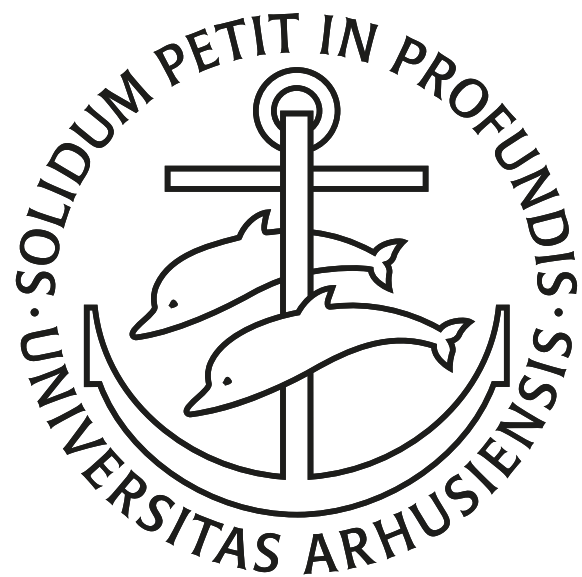
Gradient-Based Optimal Control of Quantum Many-Body Systems in Optical Lattices

Author:

Frederik S. Møller
201303717

Supervisor:

Jakob F. Sherson



Quantum Measurement and Manipulation Group
Department of Physics and Astronomy

May 9, 2018

Gradient-Based Optimal Control of Quantum Many-Body Systems in Optical Lattices

by Frederik S. Møller
201303717

Abstract

The Thesis Abstract is written here (and usually kept to just this page). The page is kept centered vertically so can expand into the blank space above the title too...

Acknowledgements

The acknowledgments and the people to thank go here, don't forget to include your project advisor...

Contents

Abstract	iii
Acknowledgements	v
1 Ultracold Quantum Gases in Optical Lattices	1
1.1 Optical Lattice Potentials	1
1.1.1 Trapping of Neutral Atoms	1
1.1.2 Optical Lattices	3
1.1.3 Band Structure	3
1.1.4 Localized States	4
1.2 Bose-Einstein Condensates	5
1.2.1 Non-Interacting Particles	6
1.2.2 Weakly Interacting Particles	7
1.3 Bose-Hubbard Model of Interacting Bosons in a Lattice	8
1.3.1 The Bose-Hubbard Hamiltonian	9
1.3.2 Phases of the Bose-Hubbard Model	10
1.3.3 Quantum Phase Transition	13
2 Quantum Optimal Control Theory	17
2.1 The Gradient-Ascent Pulse Engineering Method - GRAPE	17
2.2 Gradient-Optimization Using Parametrization - GROUP	22
2.2.1 Alteration of constraints through GROUP	23
2.3 Interior Point Method	23
2.3.1 Karush-Kuhn-Tucker conditions	24
2.3.2 Barrier Problems	24
2.3.3 Primal-Dual Interior Point Method	25
2.4 Quantum Speed Limit	26
3 Matrix Product States	29
3.1 Entanglement in Quantum Systems and Area Laws	29
3.2 Construction of an MPS	30
3.3 Canonical Forms	32
3.3.1 Left-canonical matrix product state	33
3.3.2 Right-canonical matrix product state	33
3.3.3 Mixed-canonical matrix product state	34
3.3.4 Bringing a matrix product state into canonical form	35
3.4 Overlaps and Efficient Contractions	35
3.5 Matrix Product Operators	36
3.5.1 Applying an MPO to an MPS	37
3.6 Correlation Functions and Measurement of Local Properties	38
3.6.1 Correlation length	38

4 Tensor Network Algorithms	43
4.1 Variational Ground State Search	43
4.1.1 Efficient Application of a Hamiltonian to an MPS	43
4.1.2 Iterative Ground State Search and the DMRG Algorithm	46
4.2 Time Evolution of Matrix Product States	50
4.2.1 The tDMRG Algorithm	50
4.2.2 Modified Time Evolution Algorithm for Optimal Control	52
5 Results	59
5.1 Characterization of Methods on a Small System	59
5.1.1 Boundary Conditions	60
5.1.2 Seed Selection	60
5.1.3 Determining the Quantum Speed Limit	61
5.1.4 Optimized Ramp Sequences	62
5.1.5 Control Basis Size	64
5.2 Optimal Control of Large Lattice Systems	65
Bibliography	67
A Example: Quantum Speed Limit in Landau-Zener Model	73
B Diagrammatic Representation of Matrix Product States	75
C Example: Building an MPO from a Hamiltonian	77
D Calculation of Condensate Fraction using DMRG Algorithm	79

Chapter 1

Ultracold Quantum Gases in Optical Lattices

Ultracold atoms present an extremely powerful tool in quantum research. At the scale of nanokelvins thermal effects no longer destroy the otherwise fragile quantum systems. Thus, quantum phenomena, previously known only from theory, can be studied directly. Atomic physics experiments with such ultracold, quantum degenerate gases offer some unique features: (i) a wide range of Hamiltonians can be mapped to the systems making experiments highly customizable. This can in part be attributed to (ii) the very high degree of control achievable through the manipulation of external fields. Many different configurations of magnetic and optical traps achievable in which the cold atoms can be manipulated very precisely. Furthermore, the collisional properties of the atoms can be tuned through magnetic Feshbach resonances, and the properties of the gas can be probed through interactions between internal energy levels of the atoms and laser light [28, 5].

At temperature scales around $\approx 100\text{nK}$ many-body phenomena such as Bose-Einstein condensation takes place, where the ground state of the system gains a macroscopic populations. Ever since the first realisation of a Bose-Einstein condensate in 1995 [3], the special properties of this macroscopic quantum state have been used in a wide range of experiments. A powerful tool in the cold-atoms toolbox is the optical lattice, which is an array of potentials created through the atoms dipole interaction with laser beams. The cold atoms are loaded into the highly controllable lattice from where one can perform quantum simulations of various systems, such as spin chains [61], Dirac cones [66], and artificial gauge fields [13]. Furthermore, the properties of cold atoms in optical lattices are very favourable for experiments in quantum information, where quantum gates can be realised through controlled collisions [30] or Rydberg atoms [56].

1.1 Optical Lattice Potentials

Cold atoms can be trapped in potentials generated by their own dipole interaction with light. Thus, superimposing laser beams allows one to create optical potentials in various shapes and forms. Such dipole traps realised using far-detuned light have important properties, as (i) they are capable of trapping neutral atoms, and (ii) the optical excitation from the trap is very low resulting in only small losses [22].

Optical lattices are a central component of many experiments, as they not only trap the atoms, but also determine important properties of the system.

1.1.1 Trapping of Neutral Atoms

Consider a two level atom in the presence of a time-varying electric field

$$\mathbf{E} = \epsilon E_0 \exp(i(\mathbf{k}\mathbf{r} - \omega_L t)) , \quad (1.1)$$

where E_0 is its amplitude, ε is its polarization vector, \mathbf{k} is its wave vector and ω_L is its frequency. The interaction between the atom and the electric field causes a perturbation of the atoms energy levels, otherwise known as the AC Stark-shift. The Hamiltonian describing this interaction is

$$\hat{H}_{int} = \hat{d}\mathbf{E}, \quad (1.2)$$

where $\hat{d} = -e\hat{\mathbf{r}}$ is the electric dipole operator.

Consider eq. (1.2) as a perturbation to the Hamiltonian of the atom. To first order the non-degenerate, time-independent perturbation of the energy of state i reads

$$E_i^{(1)} = \langle i | \hat{H}_{int} | i \rangle. \quad (1.3)$$

However, all first-order contributions vanish due to the symmetry of the Hamiltonian (1.2). To second order the perturbation of state i is given by

$$E_i^{(2)} = \sum_{j \neq i} \frac{|\langle j | \hat{H}_{int} | i \rangle|^2}{\varepsilon_i - \varepsilon_j}. \quad (1.4)$$

The states $|i\rangle$ and $|j\rangle$ and their corresponding energies, ε_i and ε_j , are of the dressed state picture, where one considers the combined system of the atom and the light field [12]. The state $|i\rangle$ represents the atom being in its ground state, while the light field contains n photons. Thus, the energy of the combined state is $\varepsilon_i = n\hbar\omega_L$, when setting the energy of the atomic ground state to zero. Meanwhile, state $|j\rangle$ is when the atom has been excited by absorbing one of the photons of the field. Hence, the energy of this state is $\varepsilon_j = \hbar\omega_0 + (n-1)\hbar\omega_L$. Defining the detuning $\Delta = \omega_L - \omega_0$ allows writing the perturbation in the form

$$E_{g/e}^{(2)} = \pm \frac{|\langle e | \hat{d} | g \rangle|^2}{\Delta} |E_0|^2, \quad (1.5)$$

where the upper sign is assigned to the atomic ground state $|g\rangle$. This can be rewritten in order to reflect properties of the atom and the field, by considering the intensity of the light, $I = 2\epsilon_0 c |\mathbf{E}|^2$, and the decay rate of the atom, $\Gamma = \frac{\omega_0^3}{3\pi\epsilon_0 c^3} |\langle e | \hat{d} | g \rangle|$. Thus, equation (1.5) can be written as [22]

$$E_{e/g}^{(2)} = \pm \frac{3\pi c^2}{2\omega_0^3} \frac{\Gamma}{\Delta} I \quad (1.6)$$

This is the AC-Stark shift, which constitutes the dipole potential. For red detuning ($\Delta < 0$) the ground state will experience a negative shift leading to an attractive potential with depth depending on the intensity of the laser. Oppositely, a blue-detuned laser ($\Delta > 0$) will repel the atom. An illustration of this can be seen in figure 1.1. Since the sign of the perturbation is reversed for the excited state, the effect of the detuning becomes opposite, whereby it is important that the atom remains in the ground state. Thus, one has to minimize the scattering with the optical potential. The scattering rate is given as [22]

$$\Gamma_{sc} = \frac{3\pi c^2}{2\hbar\omega_0^3} \left(\frac{\omega}{\omega_0} \right)^3 \left(\frac{\Gamma}{\Delta} \right)^2 I. \quad (1.7)$$

As the detuning becomes small, the laser becomes resonant with the atom causing a large increase in scattered photons. Therefore, one has to choose a large detuning in order for the potential to remain conservative. However, this comes at the cost of a weaker potential. To compensate this, a high laser intensity must be used for the potential to reach sufficient depth. In practice there will be a limit to the laser power available, however, for most

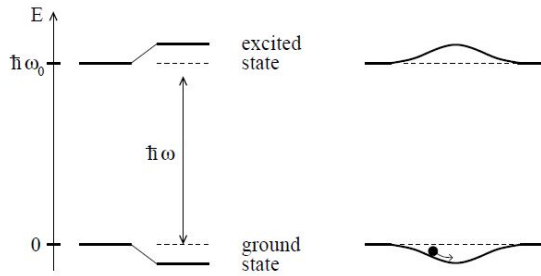


FIGURE 1.1: *Light shifts of a two-level atom. Left-hand side, red-detuned light ($\Delta < 0$) shifts the ground state down and the excited state up by same amounts. Right-hand side, a spatially inhomogeneous field like a Gaussian laser beam produces a ground-state potential well, in which an atom can be trapped. Figure and caption are adopted from [22].*

alkali-metal atoms the detuning is typically chosen to be large compared to the excited-state hyperfine structure splitting, which provides enough depth while being sufficient to suppress scattering events [6].

1.1.2 Optical Lattices

The dipole potential in equation (1.6) scales with the intensity of the laser. Thus, superimposing laser beams enables a multitude of different potentials through the interference patterns of the lasers. A standing wave from two counter-propagating light fields will lead to an array of potential wells

$$V(z) = -V_0 \cos^2 kz, \quad (1.8)$$

where $V_0 = |\frac{3\pi c^2}{2\omega_0^3} \frac{\Gamma}{\Delta} 4I_0|$ is derived from eq. (1.6). In practice, the one-dimensional lattice structure of eq. (1.8) is created by shining a single laser beam at a mirror, whereby it interferes with itself. Adding another standing laser beam in a different direction creates a periodic two dimensional potential. For orthogonal polarization of the two lasers, the resulting potential is purely the sum of the sinusoidal standing wave potential, as no interference term is present [38]. Note, the lattice is only well defined for distances much smaller than the waist of the laser beams, as the lattice is only present within the overlap of the two beams. Various shapes of the lattice can be achieved by adjusting the angle between the beams, however, the most common setup is using two orthogonal beam creating a square lattice of one dimensional tubes, as seen in figure 1.2. In order to create a three dimensional lattice, as seen in figure 1.2, an additional third perpendicular laser beam is needed. In the center of the trap, the lattice potential is then given by

$$V(x, y, z) = -V_0 (\cos^2 kx + \cos^2 ky + \cos^2 kz), \quad (1.9)$$

for distances much smaller than the beam waist. In addition to the lattice, an external harmonic confinement will be present due to the Gaussian profile of the laser beams [6].

1.1.3 Band Structure

Consider a periodic potential as described by eq. (1.8). *Bloch's Theorem* states that energy eigenstates of a periodic potential with lattice vector \mathbf{R} and quasi-momentum \mathbf{q} can be written as Bloch waves, which take the form

$$\phi_{\mathbf{q}}^{(n)}(\mathbf{r}) = e^{i\mathbf{qr}} u^{(n)}(\mathbf{r}), \quad (1.10)$$



FIGURE 1.2: (a) Two dimensional optical lattice formed by two mutually orthogonal laser beams. These tubes have a characteristic cigar shape, due to the Gaussian profile of the lasers. (b) Upon using three orthogonal laser beams, the result is a three dimensional lattice reminiscent of a cubic crystal. Figure is adopted from [78].

which is a plane wave modulated by a function with the same periodicity as the potential $u^{(n)}(\mathbf{r}) = u^{(n)}(\mathbf{r} + \mathbf{R})$. Furthermore, the Bloch waves are periodic in reciprocal space, such that $\phi_{\mathbf{q}}^{(n)}(\mathbf{r}) = \phi_{\mathbf{q} + \mathbf{G}}^{(n)}(\mathbf{r})$, where \mathbf{G} is a reciprocal lattice vector. [33]

This leads to an energy spectrum in the shape of bands with the periodicity of the first *Brillouin Zone*. Bands are denoted by the band index n , and their shape is determined by both the shape and the depth of the potential. The potential depth is often denoted in units of the recoil energy $E_{\text{rec}} = \frac{\hbar^2 k^2}{2m}$, where m is the mass of the atom, and k is the photon wave number of the light forming the optical lattice. For $V_0 = 0$, the particles are free, hence the bands will be parabolic. Meanwhile, for $V_0 \rightarrow \infty$, no interaction between different wells of the lattice can take place, as the wavefunctions of the trapped atoms will be confined to their respective well. Thus, the lattice is reduced to an array of independent harmonic oscillators, whereby the bands will appear flat with equal spacing [21].

1.1.4 Localized States

For lattice potential depths within $5E_{\text{rec}} \leq V_0 \leq 8E_{\text{rec}}$, the lattice is in the *tight binding limit*. Within this range the wavefunctions of the trapped atoms will only overlap with other wells in their closest proximity. Thus, interactions between wells are almost purely of nearest neighbour nature. Due to how well localized the wavefunctions are, a basis of Wannier functions is ideal for describing the system. Wannier functions are related to Bloch functions through the Fourier transform [34]

$$w^{(n)}(\mathbf{r}) = \frac{1}{\sqrt{N_L}} \sum_q e^{-i\mathbf{q}\mathbf{R}} \phi_{\mathbf{q}}^{(n)}(\mathbf{r}), \quad (1.11)$$

where N_L is the number of primitive cells of the lattice. The Wannier functions are well localized and centered around the lattice at site \mathbf{R} . In the case of a separable periodic potential, like that of eq. (1.9), the single-particle problem becomes one-dimensional [35]. Lastly, Wannier functions obey the orthonormality relation

$$\int d^3r \ w^{(n)*}(\mathbf{r} - \mathbf{R})w^{(n')}(\mathbf{r} - \mathbf{R}') = \delta_{n,n'}\delta_{\mathbf{R},\mathbf{R}'} , \quad (1.12)$$

thus forming a complete basis [6]. Figure 1.3.a shows Wannier functions plotted for lattice

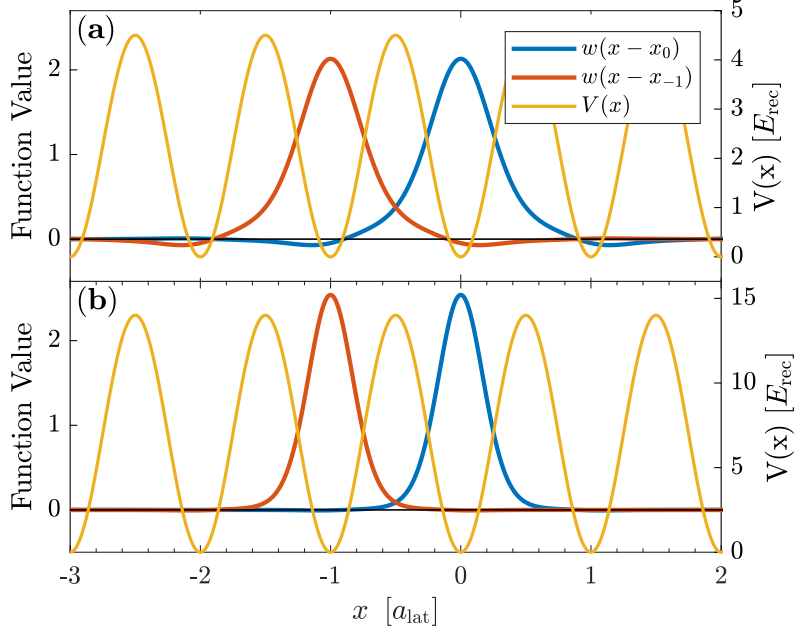


FIGURE 1.3: Two one-dimensional Wannier functions plotted for lattice depths of $V_0 = 4.5E_{\text{rec}}$ (a) and $V_0 = 14E_{\text{rec}}$ (b) respectively.

potential depths within the tight binding limit. As evident from the plot, the functions overlap with only their nearest neighbours. In the case of a more shallow lattice, the functions would extend to further wells, while they will tend towards a Gaussian shape as the lattice depth increases [21], which can be seen in figure 1.3.b.

1.2 Bose-Einstein Condensates

Bosons are particles of integer spin, whose statistics obey those of a Bose-Einstein distribution

$$n_i = \frac{g_i}{\exp((\varepsilon_i - \mu)/k_B T) - 1} , \quad (1.13)$$

where i denotes the state, n_i is the population of the state, g_i is its degeneracy, ε_i is its energy, μ is the chemical potential, k_B is the Boltzmann constant, and T is the temperature. One important feature of bosons is that, unlike fermions, multiple particles can occupy the same quantum state. At higher temperatures the energy spectrum is practically continuous, whereby this property has little effect, as two particles occupying the same single-particle state is highly unlikely. However, at low temperatures the energy spectrum systems become increasingly discrete, hence the statistics of the particles become very important. As evident

from eq. (1.13), the population of the ground state diverges as $T \rightarrow 0$. However, even below a finite temperature, T_c , one will observe a macroscopic population of the ground state. T_c is called the critical temperature, and marks the point where multiple particles will start forming a Bose-Einstein Condensate (BEC). [48]

1.2.1 Non-Interacting Particles

In the case of non-interacting particles and zero temperature, all particles of a Bose gas can be described by identical single-particles wavefunctions $\phi(\mathbf{r}_i)$. Hence, the many-body wavefunction is simply given by the product

$$\Psi(\mathbf{r}_1, \dots, \mathbf{r}_N) = \prod_i^N \phi(\mathbf{r}_i) . \quad (1.14)$$

Such a product state can be described by a single macroscopic wavefunction

$$\psi(\mathbf{r}) = \sqrt{N} \varphi(\mathbf{r}) , \quad (1.15)$$

where $\phi(\mathbf{r})$ is the wave function of the single-particle state, in which the bosons condensate into [47].

Second-Quantization

When describing Bose-Einstein condensates it is very convenient to work in second quantization, which describes the number of particle in each state rather than the state of each particle.

First, consider a basis of single particle states $\{|n\rangle\}$, namely a Fock basis. In this space particles are created or annihilated through their respective operators

$$\hat{a}_\mu^\dagger |0\rangle_\mu = |1\rangle_\mu . \quad (1.16)$$

For bosons the creation and annihilation operators fulfill the commutation relations

$$[\hat{a}_\nu, \hat{a}_\mu] = [\hat{a}_\nu^\dagger, \hat{a}_\mu^\dagger] = 0 \quad , \quad [\hat{a}_\nu, \hat{a}_\mu^\dagger] = \delta_{\nu,\mu} , \quad (1.17)$$

with the number operator given as

$$\hat{n}_\mu = \hat{a}_\mu^\dagger \hat{a}_\mu . \quad (1.18)$$

In second quantization many-body states are described by the occupation of the individual Fock states. Thus, a creation operator will raise the number of particles in its corresponding state by one, while the annihilation operator will lower it:

$$\hat{a}_\nu^\dagger |N_0, N_1, \dots, N_\nu, \dots\rangle = \sqrt{N_\nu + 1} |N_0, N_1, \dots, N_\nu + 1, \dots\rangle \quad (1.19)$$

$$\hat{a}_\nu |N_0, N_1, \dots, N_\nu, \dots\rangle = \sqrt{N_\nu} |N_0, N_1, \dots, N_\nu - 1, \dots\rangle . \quad (1.20)$$

Likewise, the number operator \hat{n}_μ will count the number of particles in its corresponding state. These operators can be combined with an orthonormal basis of spatial wavefunctions $\{\phi_k\}$ in order to create field operators

$$\hat{\psi}(\mathbf{r}) = \sum_k \phi_k(\mathbf{r}) \hat{a}_k \quad , \quad \hat{\psi}^\dagger(\mathbf{r}) = \sum_k \phi_k^*(\mathbf{r}) \hat{a}_k^\dagger , \quad (1.21)$$

where $\hat{\psi}^\dagger(\mathbf{r})$ will create a particle at location \mathbf{r} . For bosons the field operators fulfill the commutation relations [8]

$$[\hat{\psi}(\mathbf{r}), \hat{\psi}^\dagger(\mathbf{r}')] = \delta^3(\mathbf{r} - \mathbf{r}') , \quad [\hat{\psi}(\mathbf{r}), \hat{\psi}(\mathbf{r}')] = 0 . \quad (1.22)$$

Now, consider a gas of non-interacting bosons described by eq. (1.15), where ϵ_k is the energy of the k 'th single-particle state. Due to the completeness of the basis of single-particle wavefunctions, $\{\phi_k\}$, the creation operator can be expressed as

$$\hat{a}_k^\dagger = \int d^3r \phi_k^*(\mathbf{r}) \hat{\psi}^\dagger(\mathbf{r}) . \quad (1.23)$$

Thereby the non-interacting Hamiltonian can be written as

$$\begin{aligned} \hat{H}^{(0)} &= \sum_k \epsilon_k \hat{a}_k^\dagger \hat{a}_k \\ &= \sum_k \int d^3r_1 d^3r_2 \epsilon_k \phi_k(\mathbf{r}_2) \phi_k^*(\mathbf{r}_1) \hat{\psi}^\dagger(\mathbf{r}_1) \hat{\psi}(\mathbf{r}_2) \\ &= \int d^3r \hat{\psi}^\dagger(\mathbf{r}) \left(-\frac{\hbar^2}{2m} \nabla^2 + U(\mathbf{r}) \right) \hat{\psi}(\mathbf{r}) , \end{aligned} \quad (1.24)$$

where the orthonormality of the wavefunctions

$$\sum_k \phi_k(\mathbf{r}_2) \phi_k^*(\mathbf{r}_1) = \delta^3(\mathbf{r}_1 - \mathbf{r}_2) \quad (1.25)$$

has been utilized.

1.2.2 Weakly Interacting Particles

A characteristic of a BEC is its low temperature and density. Thus, is it a valid approximation to only consider two-particle interactions

$$\hat{H}^{(2)} = \frac{1}{2} \sum_{i \neq j} V(\mathbf{r}_i - \mathbf{r}_j) . \quad (1.26)$$

At low energies all interactions can be considered of s-wave nature, because waves of higher angular momentum are reflected by the centrifugal barrier. Furthermore, the thermal de Broglie wavelength for cold gases is much larger than the effective extension of the interaction potential. Therefore, the actual shape of the scattering potential is irrelevant, whereby one can replace it with a pseudo-potential

$$V(\mathbf{r} - \mathbf{r}') = g \delta^3(\mathbf{r} - \mathbf{r}') = \frac{4\pi\hbar^2 a}{m} \delta^3(\mathbf{r} - \mathbf{r}') , \quad (1.27)$$

which results in the same scattering phase as the real, more complicated scattering potential. Thus, the interaction of cold atoms is fully determined by the scattering length, a [21]. Introducing the density operator

$$\hat{\rho}(\mathbf{r}) = \hat{\psi}^\dagger(\mathbf{r}) \hat{\psi}(\mathbf{r}) , \quad (1.28)$$

allows writing $\hat{H}^{(2)}$ in second quantization

$$\begin{aligned}\hat{H}^{(2)} &= \frac{1}{2} \int d^3r_1 d^3r_2 V(\mathbf{r}_1 - \mathbf{r}_2) \hat{\psi}^\dagger(\mathbf{r}_1) \hat{\psi}(\mathbf{r}_1) (\hat{\psi}^\dagger(\mathbf{r}_2) \hat{\psi}(\mathbf{r}_2) - \delta(\mathbf{r}_1 - \mathbf{r}_2)) \\ &= \frac{1}{2} \int d^3r_1 d^3r_2 \hat{\psi}^\dagger(\mathbf{r}_1) \hat{\psi}^\dagger(\mathbf{r}_2) V(\mathbf{r}_1 - \mathbf{r}_2) \hat{\psi}(\mathbf{r}_1) \hat{\psi}(\mathbf{r}_2).\end{aligned}\quad (1.29)$$

Combining this with the basic Hamiltonian of equation (1.24), gives the full Hamiltonian in second quantization

$$\hat{H} = \hat{H}^{(0)} + \hat{H}^{(2)}\quad (1.30)$$

$$\begin{aligned}&= \int d^3r \hat{\psi}^\dagger(\mathbf{r}) \left(-\frac{\hbar^2}{2m} \nabla^2 + U(\mathbf{r}) \right) \hat{\psi}(\mathbf{r}) \\ &\quad + \frac{1}{2} \int d^3r_1 d^3r_2 \hat{\psi}^\dagger(\mathbf{r}_1) \hat{\psi}^\dagger(\mathbf{r}_2) V(\mathbf{r}_1 - \mathbf{r}_2) \hat{\psi}(\mathbf{r}_1) \hat{\psi}(\mathbf{r}_2)\end{aligned}\quad (1.31)$$

Solving the Heisenberg equations of motion using the field description of the Hamiltonian leads to

$$i\hbar \frac{\partial}{\partial t} \hat{\psi}(\mathbf{r}) = [\hat{\psi}(\mathbf{r}), \hat{H}] = \left(-\frac{\hbar^2}{2m} \nabla^2 + U(\mathbf{r}) + g \hat{\psi}^\dagger(\mathbf{r}) \hat{\psi}(\mathbf{r}) \right) \hat{\psi}(\mathbf{r}),\quad (1.32)$$

which is not analytically solvable. However, if the scattering length a is much less than the mean inter-particle distance, such that $na^3 \ll 1$, where n is the density of the gas, the mean-field approximation is viable

$$\hat{\psi}(\mathbf{r}) = \psi(\mathbf{r}) + \delta\hat{\psi}(\mathbf{r}),\quad (1.33)$$

where $\psi(\mathbf{r})$ is the mean-field given by eq. (1.15), and $\delta\hat{\psi}(\mathbf{r})$ is fluctuations from the mean. If $\langle \delta\hat{\psi}(\mathbf{r}) \rangle = 0$, the fluctuations can be neglected, leading to the Gross-Pitaevskii equation [23, 49]

$$i\hbar \frac{\partial}{\partial t} \hat{\psi}(\mathbf{r}) = \left(-\frac{\hbar^2}{2m} \nabla^2 + U(\mathbf{r}) + g|\psi(\mathbf{r})|^2 \right) \psi(\mathbf{r}).\quad (1.34)$$

The Gross-Pitaevskii equation is very similar to the Schrödinger equation with exception of the non-linear term $g|\psi(\mathbf{r})|^2$, which can make the equation hard to solve in regions of low density.

1.3 Bose-Hubbard Model of Interacting Bosons in a Lattice

The Bose-Hubbard model describes weakly interacting bosons in a periodic lattice within the tight binding limit. The model is perfectly capable of predicting results with good accuracy, however, two conditions must hold in order for it to be valid: (i) both the thermal energy and the mean interaction energy at a single site must be much smaller than the separation to first excited band, $\hbar\omega_0$, and (ii) the Wannier functions decay essentially within the length of the lattice constant [6]. Under these conditions one is assured that only the lowest band is taken into account, and that only nearest-neighbour interactions take place.

The Bose-Hubbard model is interesting, as it supports two distinct phases: the Superfluid phase and the Mott-Insulator phase. Furthermore, the model contains effects such as a quantum phase transition between the two phases mentioned above, which can be crossed without any change in external parameters.

1.3.1 The Bose-Hubbard Hamiltonian

Consider the Hamiltonian for bosonic particles in a trapping potential in one dimension as described by eq. (1.31). For a periodic lattice potential in the tight binding limit it is favourable to work in a basis of localized Wannier functions. Expanding the field operators of the Hamiltonian in eq. (1.31) in the Wannier basis yields [29]

$$\begin{aligned}\hat{H} &= \int dx \sum_{ij} w^*(x - x_i) \hat{a}_i^\dagger \left(-\frac{\hbar^2}{2m} \nabla^2 + V(x) \right) w(x - x_j) \hat{a}_j \\ &\quad + g \int dx \sum_{ijkl} w^*(x - x_i) w^*(x - x_j) w(x - x_k) w(x - x_l) \hat{a}_i^\dagger \hat{a}_j^\dagger \hat{a}_k \hat{a}_l\end{aligned}\quad (1.35)$$

$$= - \sum_{ij} J_{ij} \hat{a}_i^\dagger \hat{a}_j + \sum_{ijkl} U_{ijkl} \hat{a}_i^\dagger \hat{a}_j^\dagger \hat{a}_k \hat{a}_l , \quad (1.36)$$

where

$$J_{ij} = - \int dx w^*(x - x_i) \left(-\frac{\hbar^2}{2m} \nabla^2 + V(x) \right) w(x - x_j) \quad (1.37)$$

$$U_{ijkl} = g \int dx w^*(x - x_i) w^*(x - x_j) w(x - x_k) w(x - x_l) \quad (1.38)$$

Since the system is periodic, one can consider a single site, $i = 0$, as representative for the entire lattice. In this way, the different terms of the Hamiltonian can be interpreted as follows:

- J_{00} = constant energy offset
- J_{01} = "overlap matrix element" to neighbouring site
- $J_{02-0\infty}$ = "overlap matrix element" to further sites
- U_{0000} = on-site interaction for two particles
- U_{0ii0} = interaction off-site
- U_{0001} = interaction + tunnelling, off-site

Due to the rapid decay of the Wannier functions, the overlap of wavefunctions is limited to their nearest neighbour. Dropping all exponentially suppressed terms and constant offsets yields the Bose-Hubbard Hamiltonian

$$\hat{H} = -J \sum_{\langle i,j \rangle} \hat{a}_i^\dagger \hat{a}_j + \frac{U}{2} \sum_i \hat{n}_i (\hat{n}_i - 1) + \sum_i \varepsilon_i \hat{n}_i , \quad (1.39)$$

where $J = J_{01}$, the bracket $\langle i, j \rangle$ denotes only counting neighbouring pairs, and

$$U = U_{0000} = g \int dx |w(x)|^4 . \quad (1.40)$$

The first term of the Bose-Hubbard Hamiltonian describes the kinematics within the model, which takes the form of tunneling between neighbouring sites. This is interpreted by annihilating a particle at site j while creating a particle at site i . The second term describes the interaction between particles within a single site, and the last term $\sum_i \varepsilon_i \hat{n}_i$ takes into account a possible potential offset at different sites. Figure 1.4 illustrates the parameters of the Bose-Hubbard model as function of the lattice depth. The tunneling matrix element



FIGURE 1.4: Tunneling matrix element, J , of eq. (1.37) and interaction strength, U , of eq. (1.40) as function of lattice depth. The parameters are calculated for Rubidium-87 atoms in an optical lattice with wavelength $\lambda = 1064\text{nm}$. The phase transition between the superfluid and Mott Insulator is marked with a dashed line.

falls off very quickly with increasing lattice depth, as the Wannier functions become localized to their respective wells, thus reducing their overlap. The localization of the Wannier functions also causes the on-site interaction strength to increase.

1.3.2 Phases of the Bose-Hubbard Model

The Bose-Hubbard model supports two quantum phases: The *superfluid* phase and the *Mott-Insulator* phase. These phases depend on the ratio J/U , and can be described separately by examining the ground state of the Bose-Hubbard Hamiltonian in the two extreme limits of the J/U ratio.

Superfluid Phase

For a system where the tunneling matrix element J is dominant, the lowest energy is obtained by delocalizing the atoms over the entire lattice. Thereby the wavefunction will be a product over single-particle states, and the system will be a superfluid [21].

Consider the case of negligible interactions and a lattice with wells of equal depth. In this scenario the Bose-Hubbard Hamiltonian reduces to

$$\hat{H} = \hat{H}_J = -J \sum_{\langle i,j \rangle} \hat{a}_i^\dagger \hat{a}_j , \quad (1.41)$$

which is completely periodic within the lattice due to the lack of site specific terms. This leads to solutions in the shape of Bloch waves. The Fourier transform of the annihilation and creation operators reads

$$\hat{a}_j = \frac{1}{L} \sum_q e^{iqx_j} \hat{a}_q \quad , \quad \hat{a}_j^\dagger = \frac{1}{L} \sum_q e^{-iqx_j} \hat{a}_q^\dagger , \quad (1.42)$$

where L is the number of sites in the lattice. Through the Fourier transform the Hamiltonian (1.41) can be expressed in momentum space

$$\hat{H}_J = -J \sum_{q=-\infty}^{\infty} \left(e^{-iqd} + e^{iqd} \right) \hat{n}_q , \quad (1.43)$$

where d is the lattice distance. In momentum space the Hamiltonian is diagonal and has a continuous energy spectrum

$$E_q = -2J \cos(qd) . \quad (1.44)$$

Thus, the excitation spectrum of the superfluid is said to be gapless. The lowest energy is of the system is obtained for $q = 0$, whereby the ground state is

$$|\Psi_{SF}\rangle = \frac{1}{\sqrt{N_p!}} \left(\hat{a}_{q=0}^\dagger \right)^{N_p} |0\rangle = \frac{1}{\sqrt{N_p!}} \left(\frac{1}{L} \sum_{j=1}^L \hat{a}_j^\dagger \right)^{N_p} |0\rangle , \quad (1.45)$$

where N_p is the number of particles. This state supports a well defined macroscopic phase on each lattice site, since the many-body state is a product over identical single-particle states [21]. With all particle condensed into the $q = 0$ momentum space state, the particles are completely de-localized in real space, which can be seen by taking the Fourier transform. For large $N_p, L \rightarrow \infty$ at fixed density N_p/L the state becomes indistinguishable from having coherent states, $|\alpha\rangle$, on all lattice sites [6]. Since bosonic operators at different sites commute, the superfluid state can be factorized into a product of local coherent states

$$|\Psi_{SF}\rangle \approx \prod_j \left(e^{\sqrt{N_p/L} \hat{a}_j^\dagger} \right) |0\rangle = |\alpha_1\rangle \otimes |\alpha_2\rangle \otimes \dots \quad (1.46)$$

Coherent states are eigenstates of the annihilation operator $\hat{a} |\alpha\rangle = \alpha |\alpha\rangle$, where $|\alpha|^2$ can be

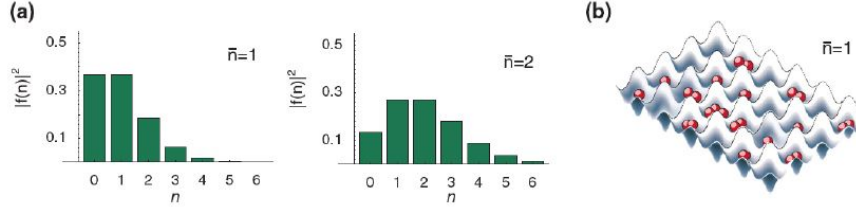


FIGURE 1.5: (a) The statistics for the number of particles per lattice site n for a filling fraction of $\bar{n} = 1$ and $\bar{n} = 2$ in the superfluid phase. (b) Illustration of the particles in the lattice. There will be large fluctuations of the number of particles found at each lattice site at a given time. Figure and caption adopted from [21].

considered the particle density of the system, and $\alpha = |\alpha|e^{i\phi}$, with ϕ being a global phase. Utilizing the coherent state form of the wavefunction (1.46) the average filling fraction \bar{n} can be calculated

$$\bar{n} = \langle \hat{n}_i \rangle = \langle \Psi_{SF} | \hat{a}_j^\dagger \hat{a}_j | \Psi_{SF} \rangle = \frac{N_p}{L} , \quad (1.47)$$

as well as the fluctuations of particle number per site

$$\frac{\sqrt{\Delta \bar{n}^2}}{\bar{n}} \sim \frac{1}{\sqrt{\bar{n}}} . \quad (1.48)$$

Therefore, the probability distribution for the number of atoms at a given site is Poissonian, which can be seen in figure 1.5. Due to the relatively large fluctuation of particle number per site, one would find a somewhat random number of atoms at a given site in a single measurement. However, averaging over many measurements well produce the filling fraction \bar{n} . In the presence of a finite interaction the resulting distribution would be sub Poissonian due to number squeezing [21].

Mott-Insulator Phase

In the case of negligible tunneling only the on-site interaction between the atoms has to be taken into account, and the Bose-Hubbard Hamiltonian reduces to

$$\hat{H} = \hat{H}_U = \frac{U}{2} \sum_i \hat{n}_i (\hat{n}_i - 1) , \quad (1.49)$$

which is quadratic in \hat{n}_i . This heavily penalizes having multiple particles at the same site. Thus, the ground state of the system will be an equal distribution of all the particles throughout the lattice. Any fluctuations from this average will increase the energy, whereby the phase is said to be incompressible [20]. This incompressibility can be formulated as $\partial n / \partial \mu = 0$, where μ is the chemical potential, and is the defining property of the Mott-Insulator [6].

Consider the case of average filling of one particle per site, $\bar{n} = 1$. The many-body state

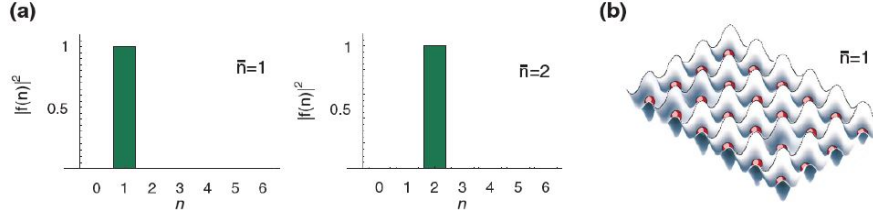


FIGURE 1.6: (a) The statistics for the number of particles per lattice site n in the Mott-insulator phase, for a filling fraction of $\bar{n} = 1$ and $\bar{n} = 2$. (b) Illustration of the particles in the lattice. The particles does not hop around in the lattice and are equally distributed. Caption and figure are adapted from [21].

can be described by a product of single particles located on each site [6]

$$|\Psi_{Mott}\rangle = \prod_j \hat{a}_j^\dagger |0\rangle . \quad (1.50)$$

Eq. 1.50 is a simple product of local Fock states with precisely one atom per site, which is illustrated in figure 1.6. This configuration of atoms minimizes the energy with regards to the Hamiltonian of eq. (1.49). Any fluctuation from unit occupancy will increase the energy, as merely a single double occupancy will increase the energy by U . Thereby, unlike the energy spectrum of the Superfluid, the Mott-Insulator spectrum is gapped. As long as the gain in kinetic energy due to hopping, J , is smaller than the on-site interaction, U , the atoms remain localized. However, for $J > 0$ the ground state is no longer the product state described in eq. (1.50) [6]. As J increases, the gap in the excitation spectrum will gradually decrease until the transition to the superfluid is reached and the spectrum becomes gapless. While the Mott-Insulator phase has complete localization, the phases on the individual sites have obtained maximum uncertainty. Therefore, no phase coherence between different sites is present [21].

1.3.3 Quantum Phase Transition

Consider once again the full Bose-Hubbard Hamiltonian (1.39). The superfluid and the Mott-Insulator account for the two limits of the ratio J/U . However, in order to understand the full phase diagram of the Bose-Hubbard model, one has to derive the critical fraction $(J/U)_{crit}$ for which the phase transition occurs. There are several ways of doing this - one of them is looking at a mean-field solution of the Bose-Hubbard model. For simplicity the zero temperature case is treated here. Even without a change of temperature the phase transition still happens, hence it is referred to as a *quantum phase transition*, since the phase transition can happen without change of external parameters [55].

Applying the mean field approximation to the annihilation operator yields

$$\hat{a}_j = \psi + \delta\hat{a}_j , \quad (1.51)$$

where ψ is the locally constant mean field, and $\delta\hat{a}_j$ is the fluctuation term. Inserting this into the Hamiltonian yields

$$\hat{H}_{MF} = -J \sum_{\langle i,j \rangle} \left(\psi^* + \delta\hat{a}_i^\dagger \right) (\psi + \delta\hat{a}_j) + \text{int.} \quad (1.52)$$

Instead of considering the Hamiltonian as a whole, it can be considered as a sum of local on-site Hamiltonians

$$\hat{H}_{MF} = \sum_i \hat{h}_i . \quad (1.53)$$

For a homogeneous system one can express the kinetic part of the Hamiltonian locally if only small fluctuations from the mean field are assumed

$$\begin{aligned} \hat{a}_i^\dagger \hat{a}_j &= \left(\psi^* + \delta\hat{a}_i^\dagger \right) (\psi + \delta\hat{a}_j) \\ &= \psi^* \psi + \psi^* \delta\hat{a}_j + \psi \delta\hat{a}_i^\dagger + \delta\hat{a}_i^\dagger \delta\hat{a}_j \\ &\approx \psi^* \psi + \psi^* (\hat{a}_j - \psi) + \psi (\hat{a}_i^\dagger - \psi^*) \\ &= \psi^* \hat{a}_j + \psi \hat{a}_i^\dagger - \psi^* \psi . \end{aligned} \quad (1.54)$$

Since every term only contains a single index, one can let $j \rightarrow i$ leaving a local description

$$\hat{h}_i = Jz\psi^*\psi - Jz \left(\psi^* \hat{a}_i + \psi \hat{a}_i^\dagger \right) + \frac{U}{2} \hat{n}_i (\hat{n}_i - 1) + \mu_i \hat{n}_i , \quad (1.55)$$

where z is the number of neighbours of site i [44]. The last term added is a chemical potential, which is needed due to the lack of a fixed local particle number prompting the use of a Grand Canonical Ensemble description.

Landau theory is a general theory regarding phase transitions, which states that in the vicinity of a critical point, one may expand the free energy in a power series of some order parameter. Thus, in order to find $(J/U)_{crit}$, eq. (1.55) must be minimized. here, the order parameter is the mean field, hence

$$E_{MF} = \text{const.} + a|\psi|^2 + b|\psi|^4 + \dots \quad (1.56)$$

Eq. (1.56) constitutes an effective potential, which dictates certain properties of the system. The potential is symmetric in the complex plane allowing the system to have any phase. Furthermore, at some critical value of a , (here $a = 0$), the potential will shift from having a single central minimum to having minima at some finite $|\psi|$. This is a U(1) spontaneous

symmetry breaking, which in Landau theory is associated with a phase transition [50]. Thus, one need to compute the parameter a of equation (1.56).

One method is using second order perturbation theory, where the $\hat{\psi} = 0$ case is solved exactly, followed by adding a small $\hat{\psi}$ as a perturbation. The zeroth order of the local mean-field Hamiltonian reads

$$\hat{h}_i^{(0)} = Jz(\psi^*\psi) + \frac{U}{2}\hat{n}_i(\hat{n}_i - 1) - \mu\hat{n}_i. \quad (1.57)$$

Since the zero-order solution only contains number operators, the ground state of the solution can be expressed in the Fock basis:

$$\begin{aligned} |0\rangle &\text{ for } \mu < 0 \\ |1\rangle &\text{ for } 0 \leq \mu < U \\ |2\rangle &\text{ for } U \leq \mu < 2U \\ &\vdots \end{aligned}$$

The first order perturbation to the energy vanishes, as

$$E_i^{(1)} = \langle n | \delta\hat{h}_i | n \rangle = 0, \quad (1.58)$$

Thus, the use of a second order perturbation is required

$$E_i^{(2)} = \sum_{n \neq m} \frac{|\langle n | \delta\hat{h}_i | m \rangle|^2}{E_m^{(0)} - E_n^{(0)}}. \quad (1.59)$$

Here the perturbation Hamiltonian

$$\hat{h}_i = -zJ(\hat{a}_i\psi^* + \psi\hat{a}_i^\dagger) \quad (1.60)$$

contains only single creation/annihilation operators, whereby

$$\langle n | \delta\hat{h}_i | m \rangle = 0 \quad \text{for } |n - m| \neq 1. \quad (1.61)$$

Hence, only off-diagonal matrix elements contribute to the perturbation

$$\begin{aligned} \langle n | \hat{a}_i^\dagger | n - 1 \rangle &= \sqrt{n} \langle n | n \rangle \\ \langle n + 1 | \hat{a}_i^\dagger | n \rangle &= \sqrt{n + 1} \langle n | n \rangle \\ &\vdots \end{aligned}$$

Thereby, the second order perturbation energy reduces to

$$\begin{aligned} E_i^{(2)} &= (Jz)^2 |\psi|^2 \left(\frac{n}{E_g^{(0)} - E_{n-1}^{(0)}} + \frac{n+1}{E_n^{(0)} - E_{n+1}^{(0)}} \right) \\ &= (Jz)^2 |\psi|^2 \left(\frac{n}{U(n-1) - \mu} + \frac{n+1}{\mu - Un} \right). \end{aligned} \quad (1.62)$$

From eq. (1.56) a is the pre-factor of all terms proportional $|\psi|^2$. Collecting those across from all the perturbations yields the approximation

$$a = Jz + (Jz)^2 |\psi|^2 \left(\frac{n}{U(n-1) - \mu} + \frac{n+1}{\mu - Un} \right). \quad (1.63)$$

As stated earlier $(J/U)_{crit}$ can be found at the point where $a = 0$, hence

$$0 \stackrel{!}{=} 1 + \frac{n}{\bar{U}(n-1) - \bar{\mu}} + \frac{n+1}{\bar{\mu} - \bar{U}n}, \quad (1.64)$$

with $\bar{\mu} = \frac{\mu}{Jz}$ and $\bar{U} = \frac{U}{Jz}$. Finally, the solution for the chemical potential is [44]

$$\bar{\mu}_{\pm} = \frac{1}{2} \left(\bar{U}(2n-1) \pm \frac{1}{2} \sqrt{\bar{U}^2 - 2\bar{U}(2n+1)} \right). \quad (1.65)$$

A better understanding of the results can be obtained by examining figure ??, which displays a phase diagram of the Bose-Hubbard model. The μ_{\pm} curves encloses the region where the

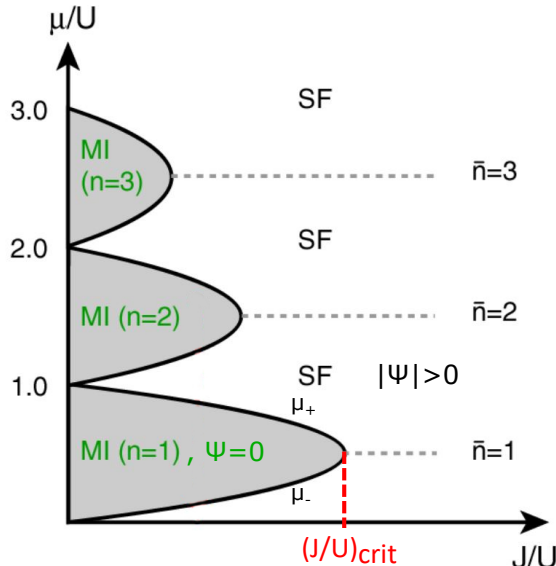


FIGURE 1.7: Phase diagram of Bose-Hubbard model for $T = 0$. Grey areas mark the Mott-Insulator phase for different number of particles per site, while white regions mark the superfluid phase. [21]

system is in the Mott-Insulating phase. $(1/\bar{U})_{crit} = (J/U)_{crit}$ can be read off the graph from the point where the two curves μ_{\pm} meet. No fluctuations take place in the Mott Insulator, whereby the particle number per site is well defined. As the chemical potential increases each site can accommodate more particles as long as the increase in chemical potential compensates the increased energy due to interactions between the particles.

The mean-field solution of the Bose-Hubbard model is only an approximation, which proves quite inaccurate for one dimension. This is obvious when comparing the critical ratio for the mean-field approach, $(U/J)_{crit}^{MF,1D} = 11.66$, with numerical results computed using the DMRG method, $(U/J)_{crit}^{DMRG,1D} = 3.37$, [36]. Nevertheless, the mean-field gives a good intuitive feeling of the physics taking place and how one can describe them without resorting to diagonalizing the Hamiltonian.

Chapter 2

Quantum Optimal Control Theory

The fundamental problem of Quantum Optimal Control Theory is to steer the dynamics of a quantum system in a desired way through external fields [53, 60]. Often, the goal is the transfer from an initial state, $|\psi_0\rangle$, to a desired target-state, $|\psi_{\text{target}}\rangle$. The fields responsible for controlling the dynamics of the system are parametrized by a set of control parameters or functions. Optimal control theory determines the parameters, which lead to the desired dynamics of the system [74].

In control problems, the Hamiltonian of the system is given as

$$\hat{H} = \hat{H}_0 + \sum_{n=1}^m \hat{H}_n(u_n(t)) , \quad (2.1)$$

where \hat{H}_0 is an uncontrollable drift, \hat{H}_n are the controllable fields, and $u_n(t)$ are the control functions. A quantum system is completely controllable if every unitary operator, \hat{U} , is accessible from the identity operator, \hat{I} , via a path $\gamma(t) = \hat{U}(t, t_0)$ satisfying [57]

$$i\partial_t \hat{U}(t, t_0) = \hat{H}\hat{U}(t, t_0) . \quad (2.2)$$

For an N -dimensional Hilbert space, a sufficient condition for complete controllability of a quantum system is that the Lie algebra generated by the Hamiltonians in eq. (2.1),

$$L_0 = \text{Lie} \left(i\hat{H}_0, i\hat{H}_1, \dots, i\hat{H}_m \right) , \quad (2.3)$$

is of dimension N^2 [52].

Extending these conditions to infinite-dimensional Hilbert spaces and constrained controls is non-trivial [26].

2.1 The Gradient-Ascent Pulse Engineering Method - GRAPE

The control problem presented in this thesis is steering the system from an initial state in the superfluid phase to a target-state in the Mott-Insulator phase. This is achieved by varying the lattice depth, which therefore can be considered the control parameter.

The optimal control problem can be stated as follows: Suppose the system is initially described by the state $|\psi_0\rangle = |\psi(0)\rangle$, and the potential is varied in the time interval $[0, T]$. The goal is finding the set of control parameters, $\mathbf{u}(t)$, which brings the initial state as close as possible to the target-state, $|\psi_{\text{target}}\rangle$. This is expressed in terms of a cost function

$$J_T = \frac{1}{2} \left(1 - | \langle \psi_{\text{target}} | \psi(T) \rangle |^2 \right) , \quad (2.4)$$

which is given as half the infidelity between the target and the state at $t = T$. The cost function becomes zero, when the terminal state matches the target state up to an arbitrary

phase. Hence, the optimal control problem can be formulated as a minimization problem of eq. (2.4) [27].

Large variations in the control parameter is often hard to achieve experimentally. Therefore, an extra term is added to the cost function, which penalizes strong variations in the control. The new cost function reads

$$J = J_T + J_R = J_T + \frac{\gamma}{2} \sum_{n=1}^m \int_0^T \left(\frac{\partial u_n}{\partial t} \right)^2 dt , \quad (2.5)$$

where γ weighs the relative importance between matching states and smoothness of the control [27]. As the state transfer is considered the highest priority, $\gamma \ll 1$ such that J_T dominates the cost function of eq. (2.5).

A powerful way of performing optimal control is the Gradient-Ascent Pulse Engineering (GRAPE) method. Through GRAPE, the gradient of the cost function (2.5) can be evaluated and used to update the existing set of controls [32]. Thereby, one achieves an optimization of the cost function.

The gradient of the cost function can be derived in multiple ways. A common method is introducing a Lagrange multiplier [25, 71, 7], which forces the dynamics to obey the Schrödinger equations. This method considers the states and the control as continuous functions, which must be discretized after the derivation of the gradient for numerical purposes. However, postponing the discretization until the very last step causes a loss of accuracy, as a series of higher order corrections due to the discretization are lost. Here, an alternative derivation following [32, 14] is presented in which the discretization is introduced immediately.

Assume the transfer time, T , is discretized in steps of $\Delta t = T/N$. Subjecting the control to a similar discretized yields

$$u_n = (u_n(t_1), \dots, u_n(t_N)) . \quad (2.6)$$

The time-evolution of the system during the time step j is given by the propagator

$$\hat{U}_j \equiv \hat{U}(u(t_j)) = \exp \left\{ -i \left(\sum_{n=1}^m \hat{H}_n(u_n(t_j)) \right) \Delta t \right\} . \quad (2.7)$$

Thereby, the cost function (2.5) becomes

$$J = \frac{1}{2} \left(1 - | \langle \psi_{\text{target}} | \prod_{j=1}^N \hat{U}_j | \psi(0) \rangle |^2 \right) + \frac{\gamma}{2} \sum_{n=1}^m \sum_{j=1}^{N-1} \left(\frac{\Delta u_n(t_j)}{\Delta t} \right)^2 \Delta t , \quad (2.8)$$

where $\Delta u_n(t_j) = u_n(t_{j+1}) - u_n(t_j)$. The full gradient of the cost, $\nabla J(\mathbf{u})$, is a vector of partial derivatives $\frac{\partial J(\mathbf{u})}{\partial u_n(t_j)}$, which can be derived analytically.

First, consider the derivative of the regularization

$$\begin{aligned} \frac{\partial J_R}{\partial u_n(t_j)} &= \frac{\gamma}{2} \left(2 \frac{u_n(t_j) - u_n(t_{j-1})}{\Delta t^2} - 2 \frac{u_n(t_{j+1}) - u_n(t_j)}{\Delta t^2} \right) \Delta t \\ &= \frac{\gamma}{\Delta t} (2u_n(t_j) - u_n(t_{j+1}) - u_n(t_{j-1})) . \end{aligned} \quad (2.9)$$

The part of the gradient related to the regularization depends only on the control, whereby it can be calculated without considering the state of the system.

Next, consider the derivative of J_T . Defining the transfer probability amplitude $\tau \equiv \langle \psi_{\text{target}} | \psi(T) \rangle$, the derivative of the final infidelity with respect to the control can be written

as

$$\frac{\partial J_T}{\partial u_n(t_j)} = -\frac{1}{2} \frac{\partial}{\partial u_n(t_j)} \tau^* \tau = -\text{Re} \left(\tau^* \frac{\partial \tau}{\partial u_n(t_j)} \right). \quad (2.10)$$

From eq. (2.10) it is evident that the derivative of the infidelity depends only on the derivative of the transfer probability amplitude, $\frac{\partial \tau}{\partial u_n(t_j)}$. This derivative can be rewritten as

$$\begin{aligned} \frac{\partial \tau}{\partial u_n(t_j)} &= \frac{\partial}{\partial u_n(t_j)} \left\langle \psi_{\text{target}} \left| \prod_{j=1}^N \hat{\mathcal{U}}_j \right| \psi(0) \right\rangle \\ &= \left\langle \psi_{\text{target}} \left| \hat{\mathcal{U}}_N \dots \hat{\mathcal{U}}_{j+1} \frac{\partial \hat{\mathcal{U}}_j}{\partial u_n(t_j)} \hat{\mathcal{U}}_{j-1} \dots \hat{\mathcal{U}}_1 \right| \psi(0) \right\rangle \end{aligned} \quad (2.11)$$

Multiplying eq. (2.11) with τ^* to recreate the result of eq. (2.10) yields

$$\tau^* \frac{\partial \tau}{\partial u_n(t_j)} = \langle \psi(T) | \psi_{\text{target}} \rangle \left\langle \psi_{\text{target}} \left| \prod_{j'=j+1}^N \hat{\mathcal{U}}_{j'} \frac{\partial \hat{\mathcal{U}}_j}{\partial u_n(t_j)} \prod_{j'=1}^{j-1} \hat{\mathcal{U}}_{j'} \right| \psi(0) \right\rangle \quad (2.12)$$

$$= i \left\langle \chi(T) \left| \prod_{j'=j+1}^M \hat{\mathcal{U}}_{j'} \frac{\partial \hat{\mathcal{U}}_j}{\partial u_n(t_j)} \prod_{j'=1}^{j-1} \hat{\mathcal{U}}_{j'} \right| \psi(0) \right\rangle \quad (2.13)$$

$$= i \left\langle \chi(t_j) \left| \frac{\partial \hat{\mathcal{U}}_j}{\partial u_n(t_j)} \right| \psi(t_{j-1}) \right\rangle, \quad (2.14)$$

where $|\chi(T)\rangle \equiv i |\psi_{\text{target}}\rangle \langle \psi_{\text{target}}| \psi(T)\rangle$ is the projection of the final state onto the target state. Notice how in eq. (2.14) the state $|\chi(T)\rangle$ has been propagated backwards in time. The derivative of the propagator, $\hat{\mathcal{U}}_j$, is non-trivial, due to possible non-commutativity between the Hamiltonian and its derivative. This results in a series of higher order corrections to the derivative of propagator. Expanding the propagator as a Taylor series before taking the derivative gives

$$\begin{aligned} \frac{\partial \hat{\mathcal{U}}_j}{\partial u_n(t_j)} &= \frac{\partial}{\partial u_n(t_j)} \exp(-i \hat{H} \Delta t) \\ &= \sum_{p=0}^{\infty} \frac{(-i \Delta t)^p}{p!} \frac{\partial \hat{H}^p}{\partial u_n(t_j)}. \end{aligned} \quad (2.15)$$

As mentioned before the Hamiltonian may not commute with its derivative. Therefore, one must be careful when taking the derivative of \hat{H}^p . Retaining the ordering of the operators while taking the derivative yields

$$\begin{aligned} \frac{\partial \hat{\mathcal{U}}_j}{\partial u_n(t_j)} &= \sum_{p=1}^{\infty} \frac{(-i \Delta t)^p}{p!} \sum_{q=0}^{p-1} \hat{H}^q \frac{\partial \hat{H}}{\partial u_n(t_j)} \hat{H}^{p-q-1} \\ &= \sum_{p=0}^{\infty} \sum_{q=0}^{\infty} \frac{A^p B A^q}{(p+q+1)!}, \end{aligned} \quad (2.16)$$

where $A \equiv -i \hat{H} \Delta t$ and $B \equiv -i \partial \hat{H} / \partial u_n(t_j) \Delta t$ have been defined for notational convenience. Through the standard relations of the gamma function, $\Gamma(z)$, one can derive the identity

$$\frac{1}{(p+q+1)!} = \frac{1}{p! q!} \int_0^1 (1-\alpha)^p \alpha^q d\alpha. \quad (2.17)$$

Thereby eq. (2.16) can be expressed as

$$\begin{aligned} \frac{\partial \hat{\mathcal{U}}_j}{\partial u_n(t_j)} &= \sum_{p=0}^{\infty} \sum_{q=0}^{\infty} \frac{A^p B A^q}{p! q!} \int_0^1 (1-\alpha)^p \alpha^q d\alpha \\ &= \int_0^1 \sum_{p=0}^{\infty} \sum_{q=0}^{\infty} \frac{(A(1-\alpha))^p}{p!} B \frac{(A\alpha)^q}{q!} d\alpha \\ &= \int_0^1 e^{(1-\alpha)A} B e^{\alpha A} d\alpha \\ &= e^A \int_0^1 e^{-\alpha A} B e^{\alpha A} d\alpha , \end{aligned} \quad (2.18)$$

where the expansion of the exponential function has been used to eliminate the sums. Although eq. (2.18) looks rather simple, evaluating the integral in its current form is a fairly hard task. Instead, the integral can be explicitly solved by applying the Baker–Campbell–Hausdorff expansion

$$e^X Y e^{-X} = \sum_{k=0}^{\infty} \frac{[X, Y]_k}{k!} = Y + [X, Y] + \frac{1}{2!}[X, [X, Y]] + \frac{1}{3!}[X, [X, [X, Y]]] + \dots \quad (2.19)$$

where $[X, Y]_k = [X, [X, Y]]_{k-1}$ and $[X, Y]_0 = Y$ is the definition of the recursive commutator [79]. Thus, eq. (2.18) reads

$$\begin{aligned} \frac{\partial \hat{\mathcal{U}}_j}{\partial u_n(t_j)} &= e^A \int_0^1 \sum_{k=0}^{\infty} \alpha^k \frac{(-1)^k}{k!} [A, B]_k d\alpha \\ &= e^A \sum_{k=0}^{\infty} \frac{(-1)^k}{(k+1)!} [A, B]_k . \end{aligned} \quad (2.20)$$

Inserting this final expression for the derivative of the propagator into eq. (2.10), one finds the exact derivative of the infidelity

$$\begin{aligned} \frac{\partial J_T}{\partial u_n(t_j)} &= -\text{Re} \left\langle \chi(t_j) \left| i e^{-i \hat{H} \Delta t} \sum_{k=0}^{\infty} \frac{(-1)^k}{(k+1)!} \left[-i \hat{H} \Delta t, -i \frac{\partial \hat{H}}{\partial u_n(t_j)} \Delta t \right]_k \right| \psi(t_{j-1}) \right\rangle \\ &= -\text{Re} \left\langle \chi(t_{j-1}) \left| \sum_{k=0}^{\infty} \frac{i^k \Delta t^{k+1}}{(k+1)!} \left[\hat{H}, \frac{\partial \hat{H}}{\partial u_n(t_j)} \right]_k \right| \psi(t_{j-1}) \right\rangle . \end{aligned} \quad (2.21)$$

For small time-steps the higher order corrections can be neglected, however, choosing a larger time-step reduces the run-time of the time-evolution, which is critical when describing many-body systems. Therefore, when using large time-steps, higher-order correlations should be included to preserve accuracy. Computing the higher order corrections can be done efficiently by analytically deriving the commutators beforehand. In section 4.2.2 an alternative propagator is constructed using the Suzuki-Trotter expansion, which causes the gradient to be exact to zeroth order.

Finally, combining the derivatives of eq. (2.9) and (2.21) produces the entries of the gradient

vector for the cost function

$$\begin{aligned} \frac{\partial J(\mathbf{u})}{\partial u_n(t_j)} = & -\text{Re} \left\langle \chi(t_{j-1}) \left| \left(i \frac{\partial \hat{H}}{\partial u_n(t_j)} \Delta t + \text{h.o.} \right) \right| \psi(t_{j-1}) \right\rangle \\ & + \frac{\gamma}{\Delta t} (2u_n(t_j) - u_n(t_{j+1}) - u_n(t_{j-1})) . \end{aligned} \quad (2.22)$$

Here h.o. denotes all higher order terms ($k > 0$).

Through the analytically derived gradient, the cost can be iteratively updated using gradient-based optimization methods until a desired threshold is reached. This forms the framework of the Gradient-Ascent Pulse Engineering (GRAPE) algorithm [32], which is summarised below:

Algorithm 1 GRAPE Algorithm

```

Choose initial control  $\mathbf{u}^{(1)}$ .
while  $J > J_{\text{threshold}}$  do
    Calculate  $|\psi(t_k)\rangle = \prod_{j=1}^k \hat{\mathcal{U}}_j |\psi(0)\rangle$  for  $k = 1 \dots N$ .
    Calculate  $|\chi(t_k)\rangle = \prod_{j=N}^k \hat{\mathcal{U}}_j^\dagger |\chi(T)\rangle$  for  $k = N \dots 1$ .
    Evaluate  $\frac{\partial J}{\partial u_n(t_k)}$  for  $k = 1 \dots N$  and  $n = 1 \dots m$  according to eq. (2.22).
    Update controls using gradient such that  $J^{(i+1)} < J^{(i)}$ .
end while

```

The computations are performed under the boundary conditions

$$\mathbf{u}(0) = \text{fixed value} \quad (2.23)$$

$$\mathbf{u}(T) = \text{fixed value} \quad (2.24)$$

$$|\psi(0)\rangle = |\psi_0\rangle \quad (2.25)$$

$$|\chi(T)\rangle = i |\psi_{\text{target}}\rangle \langle \psi_{\text{target}} | \psi(T) \rangle . \quad (2.26)$$

Figure 2.1 illustrates an update step of the controls such that the cost function is reduced. Although the starting guess of the control, $\mathbf{u}^{(1)}$, can be completely random, both faster

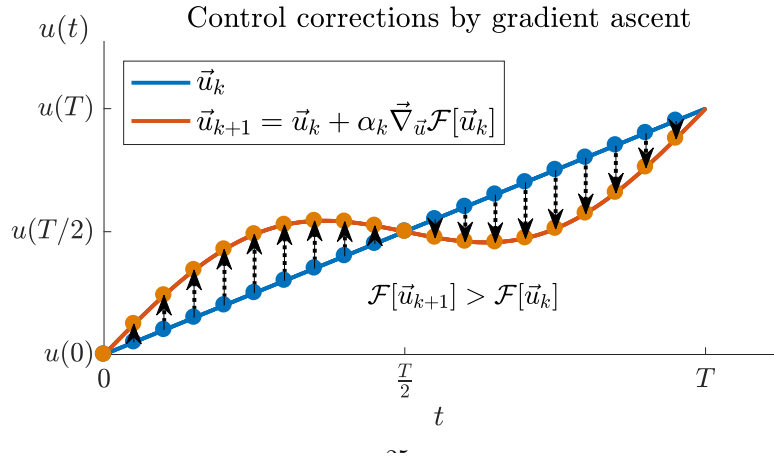


FIGURE 2.1: Visualisation of update step $i \rightarrow i + 1$ of the control $\mathbf{u}^{(i)}$ resulting in a decreased cost function.

convergence and lower convergence value is achieved by choosing a good starting seed. Clearly, there is no guarantee that the algorithm will converge to the global optimum, as it is based on a gradient ascent procedure [32]. Nevertheless, the algorithm can be made

to search a large portion of the parameter space by executing it multiple time for various seeds.

2.2 Gradient-Optimization Using Parametrization - GROUP

The convergence rate of optimal control sequences has been shown to be greatly improved by employing gradient-based methods, such as GRAPE, for updating the control [27]. One of the disadvantages of GRAPE is the dimension for the optimization. As the duration of the control pulse is discretized into N time-steps, the control at each of these steps must be optimized. For long durations or small time-steps the resulting dimension of the optimization (N) will be very large. One may consider this type of control parametrization having too many degrees of freedom for the optimization. However, employing a proper parametrization of the control can drastically reduce the optimization dimension [71].

A common choice is employing a chopped basis, which parametrizes the control as

$$u(t) = u_0(t) + S(t) \sum_{n=1}^M c_n f_n(t), \quad (2.27)$$

where f_n are the basis functions, and c_n are the optimization coefficients. In addition, $u_0(t)$ is the initial control function, and $S(t)$ is a shape function enforcing the boundary conditions of the control, whereby $S(0) = S(T) = 0$ CITE JJ ARTIKEL. The shape function used throughout this thesis consists of two steep sigmoids oriented such that S is unit for most time steps. The basis functions, f_n , must be chosen based on physical insight of the system. For the control problem discussed in this thesis, employing a basis of sine functions has proven itself useful, as the sine functions are excellent at describing the smoothly varying control pulses desired CITE JJ. Thus, the basis functions read $f_n = \sin\left(\frac{\omega_n t}{T}\right)$, where $\omega_n = n\pi$. An extension of this type of chopped basis was done in [15, 10], introducing random shifts to the frequencies resulting in the Chopped RAndom Basis or CRAB. In recent years the CRAB parametrization has been used together with the Nelder-Mead hill climbing algorithm to solve various control problems [15, 11, 67, 40].

The great advantage of employing a reduced basis representation is the drastic reduction in the optimization space. However, artificial minima can be introduced, if the chosen basis is incapable of spanning the part of the optimization space containing the optimal solutions [51]. Hence, the chopped basis dimension, M , must be chosen with consideration.

The Gradient-Optimization Using Parametrization or GROUP algorithm introduced in JJ CITE combines the chopped basis representation with the GRAPE algorithm. Parameterizing the control alters the gradient of the cost functional described in eq. (2.22). The new gradient can be derived using the chain rule

$$\begin{aligned} \frac{\partial J}{\partial c_n} &= \sum_{j=1}^N \frac{\partial J}{\partial u(t_j)} \frac{\partial u(t_j)}{\partial c_n} \\ &= \sum_{j=1}^N \frac{\partial J}{\partial u(t_j)} S(t_j) f_n(t_j), \end{aligned} \quad (2.28)$$

where only a single control has been chosen for cleaner notation. The gradient in GROUP is more complicated than in GRAPE. However, the cost of computing the gradient is still dominated by the evaluation of the derivative $\frac{\partial J}{\partial u(t_j)}$, as this requires two time-evolutions for

the full duration, T . Therefore, the increased computational cost of evaluating the gradient is negligible compared to the reduced dimensionality through the parameterization. In JJREF a comparison between different optimization algorithms for optimal control demonstrated that GROUP outperformed both GRAPE and Nelder-Mead with CRAB in term of fidelity reached and number of function evaluations required for convergence.

2.2.1 Alteration of constraints through GROUP

Consider the non-parametrized optimization problem discretized in time which is subjected to the boundaries of eq. (2.23)-(2.26). Optimal control problems are often subjected to constraints to avoid the control containing infeasible values

$$u_{min} \leq u(t_j) \leq u_{max} . \quad (2.29)$$

In the case of the Bose-Hubbard model, a lower bound of the control is needed, as the model is not well defined for lattice depths well below the tight-binding limit.

In order to enforce the constraints during a gradient-based optimization, the derivative of the constraints are needed as well. As the problem may be subjected to multiple sets of constraints, a Jacobian matrix of the constraint derivatives must be calculated

$$\mathbf{J}_{ij} = \frac{\partial g_i}{\partial x_j} , \quad (2.30)$$

where g_i are the constraint functions, and x_j are the optimization parameters.

Employing the GROUP algorithm causes a parametrization of the control, eq. (2.27), which in turn alters the constraints. Thus, one must also consider the alteration of the Jacobian. In the Bose-Hubbard control problem the constraint function is simply the control itself, whereby the transformed Jacobian reads

$$\mathbf{J}_{ij} = \frac{\partial u(t_i)}{\partial c_j} = S(t_i) f_j(t_i) . \quad (2.31)$$

Thus, the Jacobian of the constraints has $N \times M$ entries, where N is the number of time steps, and M is the dimension of the chopped basis. The matrix elements Jacobian 2.31 are easy to evaluate during the optimization, as they remain constant for the entire duration.

2.3 Interior Point Method

Through the gradient of the cost functional, the control functions can be iteratively updated yielding an improved cost. The update of the control functions can be done using various hill-climbing methods. Interior point methods are modified versions of Newtons method for bound, constrained problems. The methods approach the solution from within the feasible region and provides efficient performance while having better theoretical properties than the standard simplex method [43].

For simplicity a linear version of the method will be derived, however, the formalism can easily be extended to non-linear problems [43].

2.3.1 Karush–Kuhn–Tucker conditions

Consider the general minimization problem

$$\begin{aligned} \min_{x \in \mathbb{R}^n} \quad & c^T x \\ \text{subject to} \quad & Ax = b \\ & x \geq 0, \end{aligned} \tag{2.32}$$

can be derived from any linear problem through slack variables, which transform inequality constraints into equality constraints at the cost of introducing extra variables [72]. The Karush–Kuhn–Tucker (KKT) conditions are first-order conditions for a solution of a non-linear problem to be an optimum. Unlike Lagrange multipliers, the KKT conditions accommodates inequality constraints.

Theorem 1 Suppose that x^* is a local solution of the objective function $f : \mathbb{R}^n \rightarrow \mathbb{R}$ with respect to a collection of constraints $\{c_i(x)\}_{i=1}^m$, where $c_i : \mathbb{R}^n \rightarrow \mathbb{R}$. Let \mathcal{L} be the Lagrangian of the problem. If the subset of the equality constraints $\{c_i(x) \in \mathcal{E}\}$ has the property that $\{\nabla c_i(x^*)\}$ is linear independent, then a vector of Lagrange multipliers, λ^* , exists for which the following holds:

$$\nabla_x \mathcal{L}(x^*, \lambda^*) = 0, \tag{2.33a}$$

$$c_i(x^*) = 0, \quad \forall i \tag{2.33b}$$

$$\lambda_i^* \geq 0, \quad \forall i \in \mathcal{I} \tag{2.33c}$$

$$\lambda_i^* c_i(x^*) = 0, \quad \forall i \in \mathcal{E} \cup \mathcal{I} \tag{2.33d}$$

where \mathcal{E} and \mathcal{I} denote the equality and inequality subspaces respectively [43].

If x^* satisfies the conditions, its objective value must be at an optimum point.

2.3.2 Barrier Problems

In interior point methods the boundaries of the variables are enforced through a barrier function, which keeps the objective function continuously differentiable. A general, linear optimization problem can be associated with a barrier function

$$B(x, \mu) = c^T x - \mu \sum_{i=1}^n \ln x_i, \tag{2.34}$$

where $\mu > 0$ is the barrier parameter. For $\mu \rightarrow 0$ one recovers the original problem (2.32). The optimization Lagrangian of the barrier problem is

$$\mathcal{L}(x, \lambda, s) = c^T x - \mu \sum_{i=1}^n \ln x_i - \lambda^T (Ax - b), \tag{2.35}$$

where $\lambda \in \mathbb{R}^m$ is the Lagrange multiplier for the $Ax = b$ constraint. Now, let $X = \text{Diag}(x_1, \dots, x_n)$, $e = (1, 1, \dots, 1)^T$, $s = \mu X^{-1} e$, and $S = \text{Diag}(s_1, \dots, s_n)$. Thereby the KKT conditions of the barrier problem can be stated as

$$A^T \lambda + s = c \tag{2.36a}$$

$$Ax = b \tag{2.36b}$$

$$XSe = \mu e. \tag{2.36c}$$

By adding the barrier term the KKT conditions has been "relaxed", as they are no longer zero [54]. Again, for $\mu \rightarrow 0$ the original conditions are recovered.

2.3.3 Primal-Dual Interior Point Method

Primal-dual methods optimize an additional, *dual*, problem while optimizing the main, *primal*, problem. Consider the initial linear problem (2.32), whose dual is given by

$$\begin{aligned} & \max_{\lambda \in \mathbb{R}^n} b^T \lambda \\ & \text{subject to } A^T \lambda + s = c \\ & \quad s \geq 0 . \end{aligned}$$

The two problems are closely related. If either the primal or the dual problem has a solution, then so does the other, and the objective values are equal. If either problem is unbounded, then the other problem is infeasible. If a solution exists, then the optimal solution to the dual problem are the Lagrange multipliers to the primal problem and vice versa [43]. Hence, for primal-dual algorithms triplet of variables, (x, λ, s) , is considered when computing the optimum of a function. Note, the dual of the dual problem is the original problem.

The primal-dual interior point method optimizes a subproblem for a given μ by taking constrained Newton steps towards the optimum [43]. The optimal solution of the main problem is found by solving these subproblems iteratively for ever decreasing μ using the previous solution as starting point [72].

The solutions for the primal-dual subproblems are characterized by the KKT conditions, which can be written into a single mapping

$$F(x, \lambda, s) = \begin{pmatrix} A^T \lambda + s - c \\ Ax - b \\ XSe \end{pmatrix} = 0 \quad (2.37)$$

with the Jacobian

$$J(x, \lambda, s) = \begin{pmatrix} 0 & A^T & I \\ A & 0 & 0 \\ S & 0 & X \end{pmatrix} \quad (2.38)$$

The Newton direction, (x_B, λ_B, s_B) , can be written as the solution to the system of equations

$$J \begin{pmatrix} x_B \\ \lambda_B \\ s_B \end{pmatrix} = -F \quad (2.39)$$

The step direction equation (2.39) does not take the barrier term into account. However, the constraints can easily be added to the problem, as the barrier term merely alters the KKT conditions, F . Thereby, the constrained Newton step for the primal-dual problem reads

$$\begin{pmatrix} 0 & A^T & I \\ A & 0 & 0 \\ S & 0 & X \end{pmatrix} \begin{pmatrix} x_B \\ \lambda_B \\ s_B \end{pmatrix} = - \begin{pmatrix} A^T \lambda + s - c \\ Ax - b \\ XSe - \mu e \end{pmatrix} . \quad (2.40)$$

The functions are optimized by taking a step of length α in the direction specified by eq. (2.40), such that the updated function values read

$$(x_{k+1}, \lambda_{k+1}, s_{k+1}) = (x_k, \lambda_k, s_k) + \alpha(x_B, \lambda_B, s_B) , \quad (2.41)$$

where α can be found using a line-search or other more sophisticated methods. The procedure above can be summarized in the following algorithm [54]:

Algorithm 2 Primal-Dual Interior Point Method

```

Choose  $\sigma \in (0, 1)$  and  $\mu_0 > 0$ .
Choose initial point  $(x_0, \lambda_0, s_0)$  within feasible region.
for  $k = 1, \dots$  do
     $\mu_k \leftarrow \sigma \mu_{k-1}$ 
    Calculate the Newton direction using eq. (2.40).
    Compute step-size  $\alpha$ .
    Update parameters according to eq. (2.41)
end for

```

The implementation of the interior point algorithm used in this thesis is from the IPOPT library [73], which also approximates the Hessian of the optimization Lagrangian through previous derivatives using the L-BFGS algorithm [39]. By including information about the second derivative, the algorithm is able to converge in much fewer iterations.

2.4 Quantum Speed Limit

A subtlety in the formulation of optimal control problems is that one is only searching for the control, $\mathbf{u}(t)$, which steers the initial state into the target-state at exactly the duration $t = T$. However, it is often desirable to obtain the desired state in the shortest timespan possible. If a solution exists at $t = T_1$, it might not exist at $t = T_2 < T_1$. The shortest duration for which a solution can be found is called the *quantum speed limit* (QSL). The speed at which the system can evolve is determined by the relevant energy scales. If the system only has access to finite energies, a lower bound for how fast the system can evolve exists, which in turn leads to the QSL [9].

The quantum speed limit can also be interpreted geometrically by examining how the state of the system moves through the Hilbert space. Considering the transfer $|\psi\rangle \rightarrow |\chi\rangle$, the fidelity $F = |\langle\psi|\chi\rangle|$ is a measure of the overlap of the states. The fidelity is zero if the two states are orthogonal, while its maximum value of one is obtained if the states are identical up to a global phase. The distance between the two states in the Hilbert space can be interpreted as an angle [80]

$$\theta = \arccos(\sqrt{F}) , \quad (2.42)$$

where an angle of $\theta = \pi/2$ corresponds to orthogonal states, while states of unit fidelity are equivalent to $\theta = 0$. The velocity of the state evolution can be defined as the rate of change of the angle, which is given by [2]

$$\frac{d\theta}{dt} = \Delta E , \quad (2.43)$$

where ΔE is the energy spread given by the variance of the Hamiltonian

$$\Delta E = \sqrt{\langle\psi|\hat{H}^2|\psi\rangle - \langle\psi|\hat{H}|\psi\rangle^2} . \quad (2.44)$$

The energy spread must obey the Heisenberg time-energy uncertainty principle providing a fundamental limit to the velocity in the Hilbert space. The quantum speed limit for the transfer between two arbitrary states $|\psi\rangle$ and $|\chi\rangle$ separated by the angle θ was derived in [41] as

$$T_{\text{QSL}} = \frac{\theta}{\Delta E}. \quad (2.45)$$

However, the derivation of (2.45) assumes a time-independent Hamiltonian, which is very rarely the case in optimal control problems. The quantum speed limit for a time-dependent energy spread can be derived using arguments from differential geometry [2, 19]

$$\int_0^T \Delta E(t) dt \geq \theta. \quad (2.46)$$

Eq. (2.46) states that the path length transversed in the Hilbert space is bounded by the initial angle θ . The quantum speed limit is reached when the time-dependent Hamiltonian realizes the most direct path in the Hilbert space between the states $|\psi\rangle$ and $|\chi\rangle$. Note that eq. (2.46) does not directly provide the quantum speed limit, as the control functions corresponding to the shortest path are not known in general. Hence, determining the quantum speed limit from eq. (2.46) is an optimization problem in itself.

To determine the quantum speed limit, one can examine the relative motion of $|\psi(t)\rangle$ in the Hilbert space. Assuming the state is evolved according the optimal Hamiltonian realizing the equality of eq. (2.46). Thus, the direct velocity in the Hilbert space is given by $Q_{\text{opt}}(t) = \Delta E_{\text{opt}}(t)$, and the obtained fidelity can be expressed as a function of duration [19]

$$F(T) = \sin^2 \left(\int_0^T Q_{\text{opt}}(t) dt \right), \quad (2.47)$$

if the states $|\psi\rangle$ and $|\chi\rangle$ are orthogonal. Interpreting the state as moving along a geodesic in the Hilbert space between the two orthogonal states, the direct velocity is given by $Q_{\text{opt}}(t) = -\frac{d\theta(t)}{dt}$, whereby

$$F(T) = \sin^2 \left(\int_0^T -\frac{d\theta(t)}{dt} dt \right) = \sin^2 \left(-\theta(t) \Big|_0^T \right) = \sin^2 \left(\frac{\pi}{2} \frac{T}{T_{\text{QSL}}} \right). \quad (2.48)$$

The relation $\theta(T) = \frac{\pi}{2} \left(1 - \frac{T}{T_{\text{QSL}}} \right)$ is only valid if the state is moving on a geodesic, whereas eq. (2.47) is more general. A similar behavior to eq. (2.48) was reported in [11], where a number of systems were shown to behave according to the relation.

For an example of optimal control see Appendix A, which illustrates some of the consequences of the quantum speed limit.

Chapter 3

Matrix Product States

Numerical analysis of quantum many-body systems using exact diagonalisation is highly limited by system size. Due to the large number of possible configurations in a many-body system and entanglement coupling various degrees of freedom, the Hilbert space grows too large for exact methods to search. Consider the Bose-Hubbard model described in eq. (1.39). The dimension of the corresponding Hilbert space is

$$D_{\mathcal{H}} = \frac{(L + N_p - 1)!}{N_p!(L - 1)!} , \quad (3.1)$$

where L is the number of sites, and N_p is the number of particles. For unit occupancy, $N_p/L = 1$, the Hilbert space grows exponentially with the system size [83]. Therefore, descriptions using exact diagonalisation are only possible for small systems. Matrix product states parameterize the quantum states through a product of tensors, which can be depicted as a network. Decomposing the state as an explicitly contracted network of tensors enables efficient application of operators. Furthermore, the scaling of entanglement within a matrix product state is very different to the original state, as MPS follow an area law, whereby only a tiny corner of the Hilbert space has to be considered when searching for ground states [17].

This chapter will cover the basics of matrix product states including their construction and freedom of gauges called canonical forms [58]. Furthermore, the generalization of MPS to operators called matrix product operators are introduced along with their applications. Algorithms involving matrix products states such as the DMRG method [76, 75] are introduced in the following chapter.

3.1 Entanglement in Quantum Systems and Area Laws

Entanglement is a fundamental property of quantum mechanics responsible for correlating different degrees of freedom within a quantum system. Thus, the individual parts of a quantum system can not be described alone, as entanglement with the remainder of the system has to be taken into consideration. This drastically complicates any description of the system, which is why exact descriptions of many-body systems are almost impossible. The measure of entanglement within a quantum many-body system is the entanglement entropy, although it is often more instructive to look at the bipartite entanglement entropy, which measures the entanglement between two partitions of the system. Consider a bipartition of the Hilbert space $\mathcal{H} = \mathcal{H}_A \otimes \mathcal{H}_B$. A state $|\psi\rangle \in \mathcal{H}$ can be decomposed using the *Schmidt decomposition* as

$$|\psi\rangle = \sum_{\alpha} \Lambda_{\alpha} |\alpha\rangle_A \otimes |\alpha\rangle_B , \quad (3.2)$$

where the states $\{|\alpha\rangle_{A(B)}\}$ form an orthonormal basis of $\mathcal{H}_{A(B)}$, and $\Lambda_\alpha \geq 0$ are the Schmidt coefficients fulfilling $\sum_\alpha \Lambda_\alpha^2 = 1$ [46]. If only one term contributes to the Schmidt decomposition, the state is a product state i.e. the two parts of the Hilbert space are not mutually entangled. More terms implies that the state is entangled. From the Schmidt decomposition one can determine the reduced density matrix

$$\rho_A = \text{Tr}_B |\psi\rangle\langle\psi| = \sum_\alpha \Lambda_\alpha^2 |\alpha\rangle_A\langle\alpha|_A , \quad (3.3)$$

by tracing out the subsystem B . From the Schmidt decomposition one can determine the entanglement entropy of the bipartition, which is defined as the von-Neumann entropy, S , of the reduced density matrix given by [46]

$$S = - \sum_\alpha \Lambda_\alpha^2 \log \Lambda_\alpha^2 . \quad (3.4)$$

Quite often, one is not concerned with the actual entanglement entropy of the system, but rather how it scales when the region in question grows in size. It is natural to assume that the entanglement entropy scales with the *volume* of the system, since this is the case for thermal systems. However, ground states of quantum many-body systems often follow an *area law*, meaning that the scaling of the entropy is linear in the boundary area of the region. This is especially the case for systems with a gapped and local Hamiltonian [17]. In a one dimensional lattice the boundary of a bipartition is constant in size independently of where the cut is made. Hence, the entropy will be bounded by a constant independent of the size of both the system and the subsystem, if the system follows an area law. This can be understood intuitively, as only degrees of freedom within the correlation length, ξ , of the boundary will be entangled, no matter where in the system the boundary is present [24]. This observation is the key to the success of numerical computations for one-dimensional systems, as one has to consider only a small region of the Hilbert space when performing a variational search for the ground state. A highly efficient way of describing one dimensional systems is through Matrix Product States (MPS), which follow an area law by default, as they are constructed through a series of Schmidt decompositions.

3.2 Construction of an MPS

Matrix products states are parametrisations of one dimensional quantum states through a product of tensors. This parametrisation is especially intuitive for lattice systems, as each lattice site can be represented by a single tensor. These tensors have two different kinds of indices; *physical indices*, j , which corresponds to the local, physical states at a given site, and *bond indices*, α , which serves to connect neighbouring sites. Tensors can be merged by contracting the bond connecting them, which is done by summing over their common index. Equations involving matrix product states tend to grow quite long, whereby they often are described through diagrams. In the diagrammatic representation the physical indices are marked by vertical legs, while bond indices are marked by horizontal legs. When two tensors are connected by a leg, it means that the corresponding bond is contracted. Further details and examples regarding tensor diagrams can be found in Appendix B.

Consider a chain of L sites with each site having a d -dimensional local Hilbert space $\{|j_n\rangle\}$, where $n = 1, \dots, L$. An arbitrary quantum state of this system reads

$$|\psi\rangle = \sum_{j_1, \dots, j_L} c_{j_1 \dots j_L} |j_1, \dots, j_L\rangle . \quad (3.5)$$

This description of a general state can be parametrised to the MPS form by applying successive Schmidt decomposition. However, in practice this is done through Singular Value Decompositions (SVD), as these are faster to perform numerically. The two approaches are equivalent, as the singular value decomposition is essentially a restatement of the Schmidt decomposition CITE. Through an SVD, an arbitrary matrix, A , of dimensions $(M \times N)$ can be decomposed into three matrices

$$A = USV^\dagger . \quad (3.6)$$

These matrices have the following properties [58]:

- U is of dimension $(M \times \min(M, N))$ and has orthonormal columns, meaning $U^\dagger U = I$. If $M \leq N$, then it is also unitary $UU^\dagger = I$.
- S is a positive, diagonal $(\min(M, N) \times \min(M, N))$ matrix. The diagonal elements are singular values, and the number of non-zero entries is the Schmidt rank of A .
- V^\dagger is of dimension $(\min(M, N) \times N)$ and has orthonormal rows, meaning $V^\dagger V = I$. If $M \geq N$, then it is also unitary $VV^\dagger = I$.

From the general state of eq. (3.5) an MPS can be constructed through the following steps:

1. The d^L -dimensional vector $c_{j_1 \dots j_L}$ is reshaped into a $(d \times d^{L-1})$ matrix $\Psi_{j_1, (j_2 \dots j_L)}$. Performing an SVD on Ψ yields

$$c_{j_1 \dots j_L} = \Psi_{j_1, (j_2 \dots j_L)} = \sum_{\alpha_1}^d U_{j_1, \alpha_1} S_{\alpha_1, \alpha_1} (V^\dagger)_{\alpha_1, (j_2 \dots j_L)} = \sum_{\alpha_1}^d A_{\alpha_1}^{j_1} \Psi_{(\alpha_1 j_2), (j_3 \dots j_L)} , \quad (3.7)$$

where U has been reshaped into d row vectors A^{j_1} with entries $A_{\alpha_1}^{j_1} = U_{j_1, \alpha_1}$. In this notation $A_{\alpha_1}^{j_1}$ is a tensor with physical indices j_1 and bond indices α_1 . Furthermore, S and V^\dagger has been multiplied and reshaped into a $(d^2 \times d^{L-2})$ matrix, $\Psi_{(\alpha_1 j_2), (j_3 \dots j_L)}$.

2. The new matrix $\Psi_{(\alpha_1 j_2), (j_3 \dots j_L)}$ is subjected to an SVD decomposition

$$c_{j_1 \dots j_L} = \sum_{\alpha_1}^d \sum_{\alpha_2}^{d^2} A_{\alpha_1}^{j_1} U_{(\alpha_1 j_2), \alpha_2} S_{\alpha_2, \alpha_2} (V^\dagger)_{\alpha_2, (j_3 \dots j_L)} = \sum_{\alpha_1}^d \sum_{\alpha_2}^{d^2} A_{\alpha_1}^{j_1} A_{\alpha_1, \alpha_2}^{j_2} \Psi_{(\alpha_2 j_3), (j_4 \dots j_L)} , \quad (3.8)$$

where U has been decomposed into d matrices A^{j_2} with entries $A_{\alpha_1, \alpha_2}^{j_2} = U_{(\alpha_1 j_2), \alpha_2}$. The matrix $\Psi_{(\alpha_2 j_3), (j_4 \dots j_L)}$ has dimensions $(d^3 \times d^{L-3})$ and is yet again a product of the matrices S and V^\dagger from the SVD.

3. The procedure detailed in the two previous steps is continued throughout the chain leaving

$$c_{j_1 \dots j_L} = \sum_{\alpha_1, \dots, \alpha_{L-1}} A_{\alpha_1}^{j_1} A_{\alpha_1, \alpha_2}^{j_2} \dots A_{\alpha_{L-2}, \alpha_{L-1}}^{j_{L-1}} A_{\alpha_{L-1}, \alpha_L}^{j_L} \equiv A^{j_1} A^{j_2} \dots A^{j_{L-1}} A^{j_L} , \quad (3.9)$$

where the sum can be recognized as a matrix multiplication allowing a neater notation.

The construction of an MPS is illustrated in figure 3.1. Thereby, the original state (equation 3.5) can be written as a matrix product state in the form [58]

$$|\psi\rangle = \sum_{j_1, \dots, j_L} A^{j_1} A^{j_2} \dots A^{j_{L-1}} A^{j_L} |j_1, \dots, j_L\rangle . \quad (3.10)$$

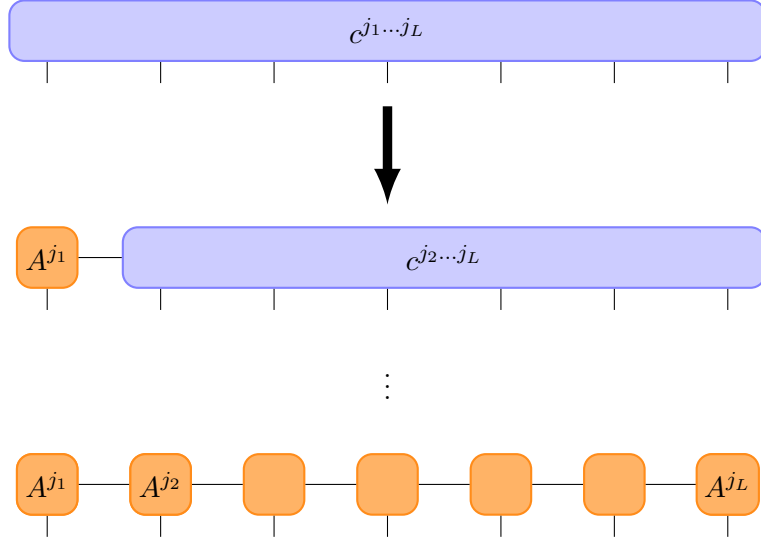


FIGURE 3.1: *Diagrammatic representation of the construction of a left-canonical MPS from an arbitrary quantum state through successive SVD's.*

Due to the dimensions of the components of an SVD, the dimensions of the matrices A^{j_n} follow a pyramid-like structure $(1 \times d), (d \times d^2), \dots, (d^{L/2-1} \times d^{L/2}), (d^{L/2} \times d^{L/2-1}), \dots, (d \times 1)$, where L is taken as even for simplicity. Hence, the matrix dimensions increase exponentially making exact computations practically impossible. However, certain simplifications can be made, which greatly reduces computational time without sacrificing much precision. First, one only needs to keep the non-zero, singular values of the matrices S , thus reducing the dimensional factor from d to r_n , where $r_n \leq d$ is the Schmidt rank of the n 'th decomposition. Secondly, as discussed earlier, only a few terms is needed to accurately describe entanglement across bonds. Therefore, the matrices S , U and V can be truncated keeping only the D largest singular values, as these contribute the most to the state. Thus, the dimension of the matrices will cap at D : $(1 \times d), (d \times d^2), \dots, (d^n \times D), (D \times D), \dots, (D \times d^n) \dots (d \times 1)$, avoiding the otherwise exponential dimensional growth [59]. The amount of singular values needed to be kept in order to produce an accurate approximation of the state is highly dependent of the system. Thus, one often need to perform the same calculation for various values of D , in order to gauge how much the matrices can be truncated.

3.3 Canonical Forms

The MPS described in equation 3.10 is not unique, as writing

$$\tilde{A}^{j_n} = X_{n-1} A^{j_n} X_n^{-1} \quad (3.11)$$

describes the same state using different matrices. This gauge freedom allows expressing the MPS in whichever way is most convenient, which can greatly reduce the effort of applying operators and calculating overlaps. By choosing a gauge, the MPS is brought into a *canonical form* [68].

3.3.1 Left-canonical matrix product state

The process of constructing an matrix product state detailed in Section 3.2 brings the MPS in a *left-canonical* form. This implies that all the matrices are left-normalized, such that

$$\sum_{j_n} A^{j_n \dagger} A^{j_n} = I . \quad (3.12)$$

The left-normalization is a consequence of the matrix U (from the SVD) fulfilling $U^\dagger U = I$. Since the matrices A^{j_n} are reshaped from U , these properties persists

$$\begin{aligned} \delta_{\alpha_n, \alpha'_n} &= \sum_{\alpha_{n-1} j_n} (U^\dagger)_{\alpha_n, (\alpha_{n-1} j_n)} U_{(\alpha_{n-1} j_n), \alpha'_n} \\ &= \sum_{\alpha_{n-1} j_n} (A^{j_n \dagger})_{\alpha_n, \alpha_{n-1}} A_{\alpha_{n-1}, \alpha'_n}^{j_n} \\ &= \sum_{j_n} \left(A^{j_n \dagger} A^{j_n} \right)_{\alpha_n, \alpha'_n} \end{aligned}$$

Figure 3.2 illustrates a contraction of the bonds connecting two left-normalised matrices. As

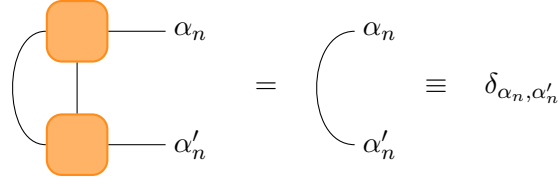


FIGURE 3.2: *Contraction over the left index (shown as the arc) and the physical index of two left-normalised matrices. The result is $\delta_{\alpha_n, \alpha'_n}$, adding the n 'th site to the contraction of all previous sites to the left.*

this contraction results in the identity per definition, one can contract left-normalised matrices without any explicit calculation. The explicit contraction is displayed diagrammatically through an arc, which is equivalent to an identity-tensor with two bond indices.

3.3.2 Right-canonical matrix product state

One could also have built a a right-canonical MPS from eq. (3.5), had one performed the SVDs from other side of the chain. Constructing the MPS from the right implies multiplying U and S into the new Ψ -matrix, and reshaping $(V^\dagger)_{(\alpha_{n-1} j_n), \alpha_n}$ into matrices $B_{\alpha_{n-1}, \alpha_n}^{j_n}$. Hence, the right-canonical form of the MPS of eq. (3.10) reads

$$|\psi\rangle = \sum_{j_1, \dots, j_L} B^{j_1} B^{j_2} \dots B^{j_{L-1}} B^{j_L} |j_1, \dots, j_L\rangle . \quad (3.13)$$

In this form all the matrices are right-normalized, whereby

$$\sum_{j_n} B^{j_n} B^{j_n \dagger} = I . \quad (3.14)$$

Note the reverse ordering of the matrix product compared to the left-normalized case. Figure 3.3 illustrates two right-normalised matrices contracted over their physical index.

$$\begin{array}{c} \text{Diagram showing two purple rectangular boxes representing matrices. The top box has an input } \alpha_n \text{ and an output } \alpha_n, \text{ with a curved arc connecting its right side to the left side of the bottom box. The bottom box has an input } \alpha'_n \text{ and an output } \alpha'_n, \text{ with a curved arc connecting its right side to the left side of the top box. An equals sign follows this. To the right is another diagram showing a single curved arc connecting } \alpha_n \text{ and } \alpha'_n. \text{ This is followed by an equivalence symbol } \equiv \text{ and the expression } \delta_{\alpha_n, \alpha'_n}. \end{array}$$

FIGURE 3.3: *Contraction over the right index (shown as the arc) and the physical index of two right-normalised matrices.*

3.3.3 Mixed-canonical matrix product state

In practice one rarely finds use for a purely left- or right-canonical MPS. However, combining the two canonical forms listed above yields the mixed-canonical form. The mixed-canonical results in a natural bi-partitioning of the system into a Schmidt decomposition, and it is especially useful for measuring local properties of the state [58].

Consider the procedure of building an MPS in the left-canonical form, where $c_{j_1 \dots j_L}$ has been decomposed from the left up until site n

$$c_{j_1 \dots j_L} = \sum_{\alpha_n} (A^{j_1} \dots A^{j_n})_{\alpha_n} S_{\alpha_n, \alpha_n} (V^\dagger)_{\alpha_n, (j_{n+1} \dots j_L)} . \quad (3.15)$$

By reshaping V^\dagger into the matrix $\Psi_{(\alpha_n j_{n+1} \dots j_{N-1}), j_N}$, one can initiate a successive decomposition from the right, resulting in a set of right-normalized matrices. The final result reads

$$c_{j_1 \dots j_N} = A^{j_1} \dots A^{j_n} S B^{j_{n+1}} \dots B^{j_L} , \quad (3.16)$$

which is illustrated in figure 3.4a. In the mixed-canonical form the Schmidt decomposition

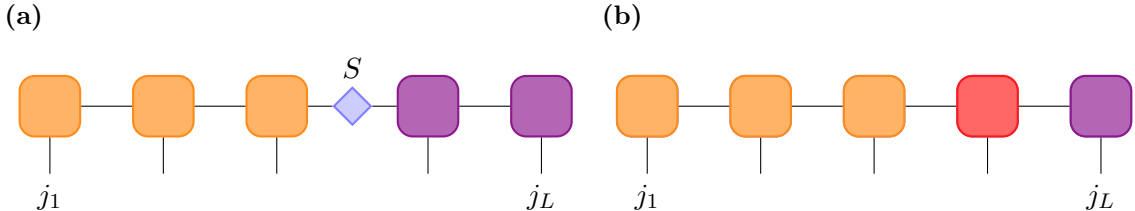


FIGURE 3.4: *Two variants of the mixed-canonical form of an MPS. The form (a) retains the matrix S originating from the SVD, whereby the MPS is directly brought into the form of a Schmidt decomposition. Multiplying S into either its left or right neighbour creates the form (b), which has a central site containing the normalization of the entire state. The form (b) is well suited for measuring local properties of the state.*

can be read directly from the form of the MPS by introducing the vectors

$$|\alpha_n\rangle_A = \sum_{j_1, \dots, j_n} (A^{j_1} \dots A^{j_n})_{1, \alpha_n} |j_1, \dots, j_n\rangle \quad (3.17)$$

$$|\alpha_n\rangle_B = \sum_{j_{n+1}, \dots, j_L} (B^{j_{n+1}} \dots B^{j_L})_{\alpha_n, 1} |j_{n+1}, \dots, j_L\rangle , \quad (3.18)$$

whereby the state can be written in the form

$$|\psi\rangle = \sum_{\alpha_n} S_{\alpha_n, \alpha_n} |\alpha_n\rangle_A |\alpha_n\rangle_B . \quad (3.19)$$

In order for eq. (3.19) to be considered a Schmidt decomposition, the matrix S must fulfill $\sum_{\alpha_n} (S_{\alpha_n, \alpha_n})^2 = 1$, which is fulfilled by default by the SVD. Furthermore, the states $|\alpha_n\rangle_A$ and $|\alpha_n\rangle_B$ have to be orthonormal respectively, which they are by construction.

Another useful version of the mixed-canonical form is depicted in figure 3.4b, where the matrix S of eq. (3.16) has been multiplied unto the matrix to either the left or right of it. The result is a central cite, which is neither left- nor right-normalized, but instead contains the normalization of the entire state. Overlaps can expectation values can be computed very efficiently using the mixed-canonical form, as most of the tensor network can be explicitly contracted due to the normalization.

3.3.4 Bringing a matrix product state into canonical form

The previous examples of canonical forms were realised during the construction of the matrix product states. However, any arbitrary MPS can be brought into a canonical form through a series of SVD's, again exploiting the left-/right-normalization of the resulting matrices.

Consider a general MPS

$$|\psi\rangle = \sum_{j_1, \dots, j_L} \sum_{\alpha_1, \dots} M_{1, \alpha_1}^{j_1} M_{\alpha_1, \alpha_2}^{j_2} M_{\alpha_2, \alpha_3}^{j_3} \dots |j_1, \dots, j_L\rangle , \quad (3.20)$$

which has to be brought into a left-canonical form. By grouping the physical and left (row) index of $M_{1, \alpha_1}^{j_1}$, one can reshape the tensor into a single matrix, $M_{(j_1, 1), \alpha_1}$. Applying an SVD yields $M = ASV^\dagger$, where $A^\dagger A = I$, such that A is left-normalized as desired. Thus, the left-normalisation of the first tensor of the MPS reads

$$\begin{aligned} |\psi\rangle &= \sum_{j_1, \dots, j_L} \sum_{\alpha_1, \dots} M_{(j_1, 1), \alpha_1} M_{\alpha_1, \alpha_2}^{j_2} M_{\alpha_2, \alpha_3}^{j_3} \dots |j_1, \dots, j_L\rangle \\ &= \sum_{j_1, \dots, j_L} \sum_{\alpha_1, \dots} \sum_{s_1} A_{(j_1, 1), s_1} S_{s_1, s_1} V_{s_1, \alpha_1}^\dagger M_{\alpha_1, \alpha_2}^{j_2} M_{\alpha_2, \alpha_3}^{j_3} \dots |j_1, \dots, j_L\rangle \\ &= \sum_{j_1, \dots, j_L} \sum_{\alpha_1, \dots} \sum_{s_1} A_{1, s_1}^{j_1} \left(S_{s_1, s_1} V_{s_1, \alpha_1}^\dagger M_{\alpha_1, \alpha_2}^{j_2} \right) M_{\alpha_2, \alpha_3}^{j_3} \dots |j_1, \dots, j_L\rangle \\ &= \sum_{j_1, \dots, j_L} \sum_{\alpha_2, \dots} \sum_{s_1} A_{1, s_1}^{j_1} \tilde{M}_{s_1, \alpha_2}^{j_2} M_{\alpha_2, \alpha_3}^{j_3} \dots |j_1, \dots, j_L\rangle , \end{aligned} \quad (3.21)$$

where $\tilde{M}_{s_1, \alpha_2}^{j_2} = \sum_{\alpha_1} S_{s_1, s_1} V_{s_1, \alpha_1}^\dagger M_{\alpha_1, \alpha_2}^{j_2}$. This procedure can be iterated through the entire chain, leaving the MPS in the left-canonical form [58].

Likewise, an MPS can be brought into a right-canonical form by grouping the physical index with the right (column) index of M yielding the SVD $M = USB$, where $BB^\dagger = I$. Thus, iterating through the chain from the right will produce a right-canonical MPS.

3.4 Overlaps and Efficient Contractions

Similarly to matrix multiplication, the number of computations need for contracting a string of tensors can be greatly reduced when performing the contractions in the right order. Consider the general case of two general states $|\psi\rangle$ and $|\phi\rangle$ described by the matrices M and \tilde{M} . The overlap between these states reads

$$\langle \phi | \psi \rangle = \sum_{j_1, \dots, j_L} \tilde{M}^{j_L \dagger} \dots \tilde{M}^{j_1 \dagger} M^{j_1} \dots M^{j_L} , \quad (3.22)$$

which is represented diagrammatically in figure 3.5. The evaluation of the overlap can be

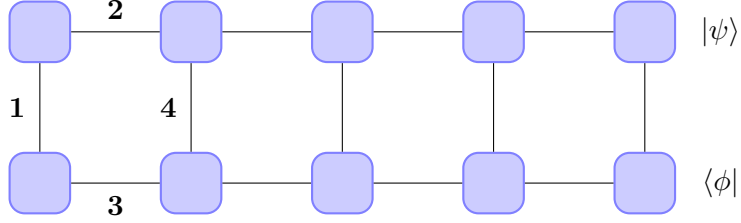


FIGURE 3.5: Efficient contraction of the overlap between two general states $|\psi\rangle$ and $\langle\phi|$. By contracting the bonds in the specified order the number of multiplications is greatly reduced.

drastically sped up by considering the optimal order of contractions, which corresponds to an optimal bracketing of eq. (3.22):

$$\langle\phi|\psi\rangle = \sum_{j_L} \tilde{M}^{j_L\dagger} \left(\dots \left(\sum_{j_2} \tilde{M}^{j_2\dagger} \left(\sum_{j_1} \tilde{M}^{j_1\dagger} M^{j_1} \right) M^{j_2} \right) \dots \right) M^{j_L}. \quad (3.23)$$

Within the innermost bracket a matrix is formed by multiplying a column and a row vector followed by the summation over the first physical index, j_1 . In the remaining set of brackets three matrices are multiplied and the corresponding physical index is summed over. However, after the first contraction the complexity of the operation does not increase. Consider the worst case scenario of all the matrices being of dimension $(D \times D)$ with a local Hilbert space of dimension d . The total operational cost of the optimal contraction is $O(LD^3d)$ compared to otherwise exponential complexity of a random order of contractions [58]. The order of contractions described in eq. (3.23) is illustrated in figure 3.5.

When calculating a norm, $\langle\psi|\psi\rangle$, the canonical form of the MPS greatly reduces to computational time, as having an either left- or right-canonical MPS implies a norm of 1 without any contractions needed.

3.5 Matrix Product Operators

A Matrix Product Operator (MPO) is an operator expressed in the formalism of an MPS. Thereby, operators can be incorporated as part of the tensor networks, where they are evaluated by the contraction of bonds.

Consider a single coefficient of an MPS of the state general $|\psi\rangle$

$$\langle j_1, \dots, j_L | \psi \rangle = \langle \mathbf{j} | \psi \rangle = M^{j_1} M^{j_2} \dots M^{j_L}. \quad (3.24)$$

Expressing an operator \hat{O} in the basis of the local states, one can write it in a similar manner

$$\hat{O} = \sum_{\mathbf{j}, \mathbf{j}'} |\mathbf{j}\rangle \langle \mathbf{j}| \hat{O} |\mathbf{j}'\rangle \langle \mathbf{j}'| = \sum_{\mathbf{j}, \mathbf{j}'} W^{j_1, j'_1} W^{j_2, j'_2} \dots W^{j_L, j'_L} |\mathbf{j}\rangle \langle \mathbf{j}'|, \quad (3.25)$$

where the coefficients are $\langle \mathbf{j} | \hat{O} | \mathbf{j}' \rangle = W^{j_1, j'_1} W^{j_2, j'_2} \dots W^{j_L, j'_L}$. The operator matrices, W^{j_n, j'_n} , differ from the state matrices, M , as the representation of the operators needs both an ingoing and an outgoing physical index. The ingoing physical index is depicted graphically as an extra vertical leg. A pictorial representation of the operator \hat{O} can be seen in figure 3.6.

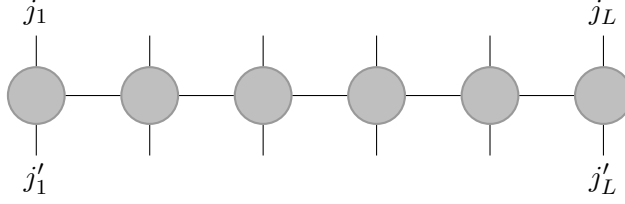


FIGURE 3.6: An operator \hat{O} expressed in the MPS form (MPO). The resulting matrix product operator has two physical indices marked by vertical lines, which corresponds to an ingoing and outgoing physical state.

3.5.1 Applying an MPO to an MPS

Applying a matrix product operator to a matrix product state is simply a matrix multiplication, where the matching physical indices are summed over:

$$\begin{aligned}
 \hat{O} |\psi\rangle &= \sum_{\mathbf{j}, \mathbf{j}'} \sum_{\alpha, \beta} \left(M_{1,\alpha_1}^{j'_1} M_{\alpha_1, \alpha_2}^{j'_2} \dots \right) \left(W_{1,\beta_1}^{j'_1, j_1} W_{\beta_1, \beta_2}^{j'_2, j_2} \dots \right) |\mathbf{j}\rangle \\
 &= \sum_{\mathbf{j}, \mathbf{j}'} \sum_{\alpha, \beta} \left(M_{1,\alpha_1}^{j'_1} W_{1,\beta_1}^{j'_1, j_1} \right) \left(M_{\alpha_1, \alpha_2}^{j'_2} W_{\beta_1, \beta_2}^{j'_2, j_2} \right) \dots |\mathbf{j}\rangle \\
 &= \sum_{\mathbf{j}} \sum_{\alpha, \beta} N_{(1,1), (\alpha_1, \beta_1)}^{j_1} N_{(\alpha_1, \beta_1), (\alpha_2, \beta_2)}^{j_2} \dots |\mathbf{j}\rangle \\
 &\equiv \sum_{\mathbf{j}} N^{j_1} N^{j_2} \dots |\mathbf{j}\rangle = |\phi\rangle
 \end{aligned} \tag{3.26}$$

The result is a new MPS, $|\phi\rangle$, which is described by the matrices N^{j_n} and is illustrated in figure 3.7. These matrices have the dimensions of the product of the dimensions of the original MPS and MPO. Thus, applying an operator leaves the form of the MPS invariant but increases the matrix dimensions. If the dimension of the MPS is D , and the dimension

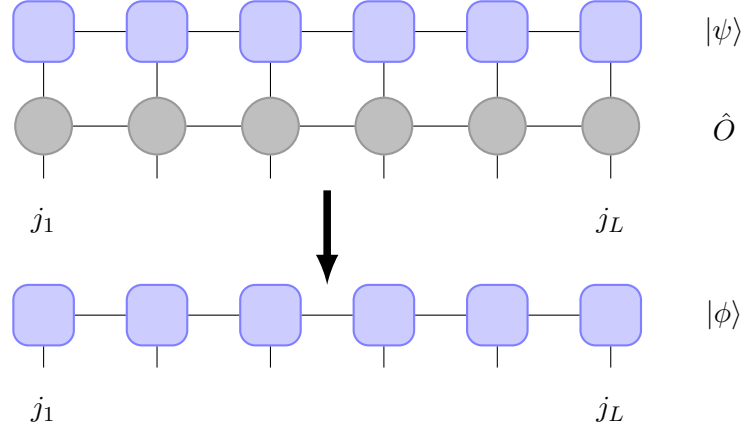


FIGURE 3.7: Application of an MPO, \hat{O} , to an MPS, $|\psi\rangle$. Matching physical indices are contracted resulting in a new MPS, $|\phi\rangle$, with increased matrix dimensions.

of the MPO is D_W , the total computational cost of the operation is $O(Ld^2 D_W^2 D^2)$.[58, 42]

3.6 Correlation Functions and Measurement of Local Properties

Measuring local properties of a state is achieved by calculating the expectation value of local operators. Consider the local operator $\hat{O}^{[n]}$, where the square brackets denote the site, on which \hat{O} operates. As $\hat{O}^{[n]}$ acts only on site n , it can be expressed in the local basis of said site

$$\hat{O}^{[n]} = \sum_{j_n, j'_n} O^{j_n, j'_n} |j_n\rangle \langle j'_n| . \quad (3.27)$$

Applying a local operator to a state implies applying the identity operator to all other sites. The full operator, $\hat{O} = \hat{I}^{[1]} \otimes \hat{I}^{[2]} \otimes \dots \otimes \hat{O}^{[n]} \otimes \dots \otimes \hat{I}^{[L]}$, can be expressed as an MPO and readily be applied to a matrix product state. However, the calculation is greatly simplified when considering an MPS in a mixed-canonical form, where the central tensor is located on site n . Thereby the entire tensor network on either side of site n can be contracted without any calculation. The remaining network needed to be contracted is shown in figure 3.8a, which is simply the sum

$$\langle \psi | \hat{O}^{[n]} | \psi \rangle = \sum_{j_n, j'_n} O^{j_n, j'_n} \text{Tr} \left(M^{j_n \dagger} M^{j'_n} \right) \quad (3.28)$$

with the computational cost $O(D^2 d^2)$ [58]. Very similar is the case of multiple-site local

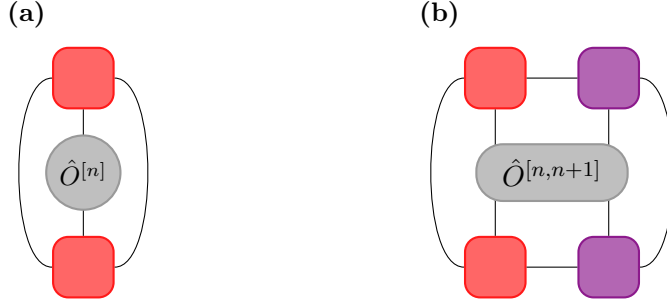


FIGURE 3.8: *Measurement of local properties of a matrix product state in the mixed-canonical form.*

operator. However, sites on which the operator act can not be contracted explicitly. Thus, the resulting tensor network will look like the example shown in figure 3.8b, where a two-site operator is measured.

Correlation functions can also be calculated efficiently using matrix product states in the mixed-canonical form. Consider the correlation $\langle \psi | \hat{O}^{[n]} \hat{Q}^{[n+k]} | \psi \rangle$, whose corresponding tensor network is shown in figure 3.9. Bringing the MPS into a mixed-canonical form with the central tensor at site m results in the outer parts of the network being explicitly contracted as identities. However, the otherwise right-normalized tensors between the two operators can not be contracted as identities, as the right-most operator breaks the canonical form. Thus, one has to contract a network of length $k+1$, which is done most efficiently following the optimal bracketing described in eq. (3.26). The complexity of the entire contraction is of order $O(kD^3d)$.

3.6.1 Correlation length

Although the MPS formalism excels at describing one dimensional systems, it struggles with describing long ranged correlations, due to how it is constructed. Consider a general MPS

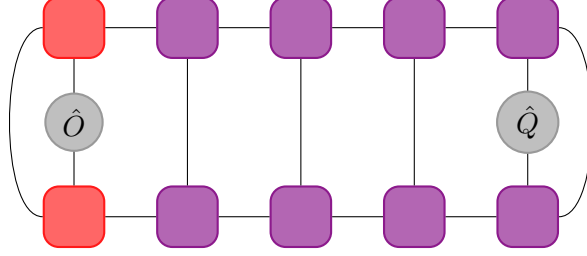


FIGURE 3.9: Tensor network for the correlation function $\langle \psi | \hat{O}^{[n]} \hat{Q}^{[n+4]} | \psi \rangle$. The outer parts of the network are implicitly contracted to identities following the mixed-canonical form of the MPS.

in no particular canonical form, as described in eq. (3.20). The *transfer operator* is defined as

$$\hat{E}^{[n]} = \sum_{\alpha_{n-1}, \alpha'_{n-1}} \sum_{\alpha_n, \alpha'_n} E_{(\alpha_{n-1} \alpha'_{n-1}), (\alpha_n \alpha'_n)}^{[n]} (|\alpha_{n-1}\rangle \langle \alpha'_{n-1}|) (|\alpha_n\rangle \langle \alpha'_n|) , \quad (3.29)$$

where $E^{[n]}$ are the matrix elements of the transfer operator

$$E^{[n]} = \sum_{j_n} M^{[n]j_n*} \otimes M^{[n]j_n} . \quad (3.30)$$

The transfer operator is essentially a complete, positive map from operators defined on a block of the lattice of length $n - 1$ to a block of length n , such that

$$\{|\alpha_{n-1}\rangle \langle \alpha'_{n-1}|\} \rightarrow \{|\alpha_n\rangle \langle \alpha'_n|\} . \quad (3.31)$$

The most important property of the transfer matrix is that all its eigenvalues $|\lambda_k| \leq 1$ if the corresponding state is either left- or right-normalized [58].

Generalizing the transfer operator matrix elements (3.30) to contraction with an operator \hat{O} at site n yields

$$E_O^{[n]} = \sum_{j_n, j'_n} O^{j_n, j'_n} M^{[n]j_n*} \otimes M^{[n]j'_n} . \quad (3.32)$$

Thereby, correlation functions can be expressed using only the transfer matrices of eq. (3.30) and (3.32). Assuming a translational invariant transfer matrices for a left-normalized state, whereby the correlation can be expressed as

$$\begin{aligned} \langle \psi | \hat{O}^{[i]} \hat{O}^{[j]} | \psi \rangle &= \text{Tr } E^{[1]} \dots E^{[i-1]} E_O^{[i]} E^{[i+1]} \dots E^{[j-1]} E_O^{[j]} E^{[j+1]} \dots E^{[L]} \\ &= \text{Tr } E_O^{[i]} E^{j-i-1} E_O^{[j]} E^{L-j+i-1} \\ &= \sum_{l,k} \langle l | E_O^{[i]} | k \rangle \lambda_k^{j-i-1} \langle k | E_O^{[j]} | l \rangle \lambda_l^{L-j+i-1} \\ &= \sum_k \langle 1 | E_O^{[i]} | k \rangle \lambda_k^{j-i-1} \langle k | E_O^{[j]} | 1 \rangle \quad (\text{for } L \rightarrow \infty) \end{aligned} \quad (3.33)$$

where $|k\rangle$ and $|l\rangle$ are eigenstates of the transfer operator with eigenvalues λ . Since $|\lambda_k| \leq 1$, only the leading eigenvalue $\lambda_1 = 1$ remains as $L \rightarrow \infty$. Defining the distance between two sites as $r = |j - i - 1|$ and the correlation length as $\xi_k = -1/\ln \lambda_k$, the correlation function can be written as

$$\frac{\langle \psi | \hat{O}^{[i]} \hat{O}^{[j]} | \psi \rangle}{\langle \psi | \psi \rangle} = c_1 + \sum_{k=2} c_k e^{-r/\xi_k} , \quad (3.34)$$

where $c_k = \langle 1 | E_O^{[i]} | k \rangle \langle k | E_O^{[j]} | 1 \rangle$. [58]

According to eq. (3.34), correlation functions are given by a linear combination of exponential functions in the MPS description. Therefore, matrix product states struggle describing long range correlations, such as the superfluid single-particle correlations. While single-particle correlations decay exponentially for the Mott-Insulator, it decays following a power-law for superfluids

$$\langle \hat{a}_i^\dagger \hat{a}_j \rangle \sim |i - j|^{-K_b/2}, \quad (3.35)$$

where K_b is the Tomonaga-Luttinger parameter [18]. For short distances eq. (3.34) is able to accurately approximate a power-law, however, only the slowest exponential decay will survive as distances grow larger. Hence, the correlation turns into a pure exponential decay with $\xi = -1/\ln \lambda$, where λ is the largest eigenvalue of \hat{E} contributing to the correlation. To demonstrate the correlation properties of matrix product states, consider figure 3.10. The figure depict the density matrix with entries $\rho_{i,j} = \langle \psi | \hat{a}_i^\dagger \hat{a}_j | \psi \rangle$ for the ground state of

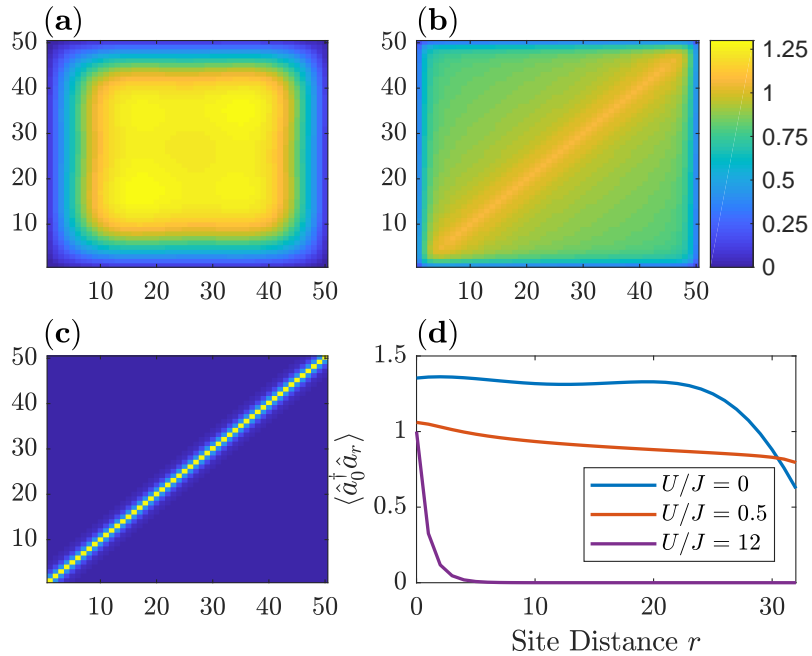


FIGURE 3.10: (a-c) Density matrices of a 50 site system for $U/J = 0, 0.5, 12$. d entries of the 15th row of the density matrices plotted as a function of distance from the diagonal, r .

a Bose-Hubbard system with $L = 50$ sites and unit occupancy. The ground state was found at various fractions of U/J using the DMRG algorithm detailed in Section 4.1.2. Figures 3.10.a and 3.10.c show the density matrix plotted for the superfluid and the Mott-Insulator limit respectively. In the superfluid limit, long-range correlations are present, which is seen by large off-diagonal elements. However, since all correlations decay exponentially in the MPS description, the algorithm has difficulty approximating the very long range correlations of the system. This is visualized in figure 3.10.d, where the correlation function is plotted against distance from the diagonal. The superfluid graph has a hump on it, which is an artifact of the MPS description and DMRG algorithm. Due to the very long correlation length, the graph should be almost flat except for the rapid drop in the end, which is due to the closed boundary conditions.

In the Mott-Insulator limit no interaction takes place between sites, and the correlation length is zero. Hence, the correlation matrix contains only diagonal elements of equal magnitude. Figure 3.10.c shows some off-diagonal elements of non-zero magnitude, since the

system is not a pure Mott-Insulator at $U/J = 12$. Nevertheless, the correlations are well described by only a single exponential function, as seen by the figure.

Finally, figure 3.10.ii illustrates the density matrix for a system with $U/J = 0.5$, which is primarily a superfluid. The particles are not completely de-localized, which is noticeable from the well defined diagonal. Plotting the correlation function reveals the best approximation being a power-law, confirming the system is indeed a superfluid.

Chapter 4

Tensor Network Algorithms

Although matrix product states enables analytical treatment of certain classes of quantum states [4, 1], their real power becomes evident when performing numerical computations. These computations require algorithms capable of exploiting the properties of the matrix product states. The Density-Matrix Renormalization Group (DMRG) was developed as the most powerful numerical method to study one-dimensional quantum lattice systems [76, 75]. Years later the connection between the DMRG method and matrix product states was made, as these two approaches share many features [45, 16]. Formulating the DMRG method in the MPS language made several extensions to the algorithm possible, which would otherwise have been very difficult to express within the DMRG framework [58]. Among these extensions one finds the tDMRG algorithm, which borrows elements from DMRG in order to perform time-evolution of a matrix product state.

This chapter covers variational ground state search through the DMRG method and time-evolution of matrix product states through the tDMRG algorithm.

4.1 Variational Ground State Search

For large systems exact diagonalization of the Hamiltonian is impossible, whereby one must resort to variational methods in order to find ground states. A variational search involves finding the state, $|\psi\rangle$, which minimizes

$$E = \frac{\langle\psi|\hat{H}|\psi\rangle}{\langle\psi|\psi\rangle}. \quad (4.1)$$

The Hamiltonian must be expressed as a matrix product operator to be applied to the state. An example is given in Appendix C, where the Bose-Hubbard Hamiltonian is formulated through tensors. Furthermore, in a variational search the state is repeatedly modified until the expectation value of the Hamiltonian is minimized. Therefore, the tensor network corresponding to eq. 4.1 must be contracted efficiently in order for the search to be viable.

4.1.1 Efficient Application of a Hamiltonian to an MPS

Section 3.5 detailed the most effective way of applying a matrix product operator to a state, however, even further reductions to the computational cost are needed, as the overlap with the Hamiltonian is evaluated many times during the ground state search. The DMRG variational search algorithm updates only a single tensor of the state at a time, whereby most of the tensor network describing the operator overlap remains constant. Hence, most of the network can be stored and used for multiple calculations, which is one of the key properties of the DMRG algorithm.

Consider a matrix product state in a mixed-canonical form

$$\begin{aligned} |\psi\rangle &= \sum_{\mathbf{j}} A^{j_1} \dots A^{j_{n-1}} \Psi^{j_n} B^{j_{n+1}} \dots B^{j_L} |\mathbf{j}\rangle \\ &= \sum_{\alpha_{n-1}, \alpha_n} |\alpha_{n-1}\rangle_A \Psi_{\alpha_{n-1}, \alpha_n}^{j_n} |\alpha_n\rangle_L , \end{aligned} \quad (4.2)$$

where Ψ^{j_n} is the central site, and $|\alpha_{n-1}\rangle_A$ and $|\alpha_n\rangle_B$ are block states introduced in eq. (3.17) and (3.18) respectively. In the basis $\{|\alpha_{n-1}\rangle, |j_n\rangle, |\alpha_n\rangle\}$ the individual matrix elements of the Hamiltonian can be expressed as

$$\langle \alpha_{n-1} j_n \alpha_n | \hat{H} | \alpha'_{n-1} j'_n \alpha'_n \rangle = \sum_{\mathbf{j}, \mathbf{j}'} W^{j_1, j'_1} \dots W^{j_L, j'_L} \langle \alpha_{n-1} j_n \alpha_n | \mathbf{j} \rangle \langle \mathbf{j}' | \alpha'_{n-1} j'_n \alpha'_n \rangle .$$

Since the basis of local states $\{|\mathbf{j}\rangle\}$ shares a state with the basis $\{|\alpha_{n-1}\rangle, |j_n\rangle, |\alpha_n\rangle\}$, the above expression can be re-written using $\sum_{\mathbf{j}} \langle j_n | \mathbf{j} \rangle = \sum_{\mathbf{j}^*} |\mathbf{j}^*\rangle$, where "*" means "excluding j_n ". Thus,

$$\begin{aligned} &\langle \alpha_{n-1} j_n \alpha_n | \hat{H} | \alpha'_{n-1} j'_n \alpha'_n \rangle = \\ &= \sum_{\mathbf{j}^*, \mathbf{j}'^*} W^{j_1, j'_1} \dots W^{j_n, j'_n} \dots W^{j_L, j'_L} \\ &\quad \times \langle \alpha_{n-1} | j_1 \dots j_{n-1} \rangle \langle \alpha_n | j_{n+1} \dots j_L \rangle \langle j'_1 \dots j'_{n-1} | \alpha'_{n-1} \rangle \langle j'_{n+1} \dots j'_L | \alpha'_n \rangle \\ &= \sum_{\mathbf{j}^*, \mathbf{j}'^*} W^{j_1, j'_1} \dots W^{j_n, j'_n} \dots W^{j_L, j'_L} \\ &\quad \times (A^{j_1} \dots A^{j_{n-1}})^*_{1, \alpha_{n-1}} (B^{j_{n+1}} \dots B^{j_L})^*_{\alpha_n, 1} \left(A^{j'_1} \dots A^{j'_{n-1}} \right)_{1, \alpha'_{n-1}} \left(B^{j'_{n+1}} \dots B^{j'_L} \right)_{\alpha'_n, 1} \\ &= \sum_{\alpha_n, \beta_n, \alpha'_n} \left(\sum_{j_1, j'_1} A_{1, \alpha_1}^{j_1*} W_{1, \beta_1}^{j_1, j'_1} A_{1, \alpha'_1}^{j'_1} \right) \left(\sum_{j_2, j'_2} A_{\alpha_1, \alpha_2}^{j_2*} W_{\beta_1, \beta_2}^{j_2, j'_2} A_{\alpha'_1, \alpha'_2}^{j'_2} \right) \dots W_{\beta_{n-1}, \beta_n}^{j_n, j'_n} \\ &\quad \times \left(\sum_{j_{n+1}, j'_{n+1}} B_{\alpha_n, \alpha_{n+1}}^{j_{n+1}*} W_{\beta_n, \beta_{n+1}}^{j_{n+1}, j'_{n+1}} B_{\alpha'_n, \alpha'_{n+1}}^{j'_{n+1}} \right) \left(\sum_{j_L, j'_L} B_{\alpha_{L-1}, 1}^{j_L*} W_{\beta_{L-1}, 1}^{j_L, j'_L} B_{\alpha'_{L-1}, 1}^{j'_L} \right) . \quad (4.3) \end{aligned}$$

While this expression may seem terrible complicated due to all the indices, it is actually rather easy to understand. First, the matrix element is written excluding the local basis state $|j_n\rangle$. Next, the Hamilton MPO is projected into the block states of A, $|\alpha_{n-1}\rangle_A$, and B, $|\alpha_n\rangle_B$. Finally, the matrices are grouped according to their expansion in the local basis. Working with the above expression appears cumbersome, but it is merely a decoupling of the system into three distinct parts, which can be seen in figure 4.1. Since both the left and right side of the network is connected, one can contract these parts into two separate

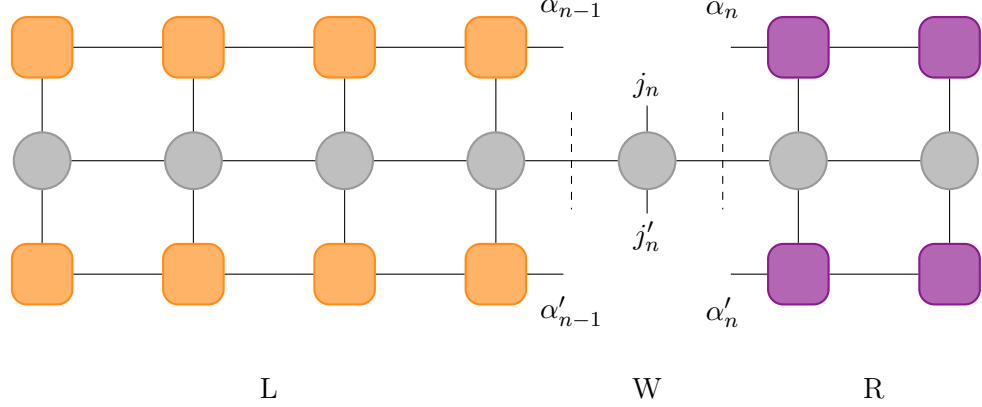


FIGURE 4.1: Representation of the matrix element $\langle \alpha_{n-1} j_n \alpha_n | \hat{H} | \alpha'_{n-1} j'_n \alpha'_n \rangle$ as a tensor network. The network can be factorize into three distinct parts: The left (L) and right (R) environments consisting of the contracted network to the left and right of the operator tensor, $W^{[n]}$, respectively.

tensors L and R called *environments*:

$$L_{\alpha_n, \beta_n, \alpha'_n} = \sum_{\{\alpha_i \beta_i \alpha'_i\}} \left(\sum_{j_1, j'_1} A_{1, \alpha_1}^{j_1*} W_{1, \beta_1}^{j_1, j'_1} A_{1, \alpha'_1}^{j'_1} \right) \dots \left(\sum_{j_n, j'_n} A_{\alpha_{n-1}, \alpha_n}^{j_n*} W_{\beta_{n-1}, \beta_n}^{j_n, j'_n} A_{\alpha'_{n-1}, \alpha'_n}^{j'_n} \right) \quad (4.4)$$

$$R_{\alpha_n, \beta_n, \alpha'_n} = \sum_{\{\alpha_i \beta_i \alpha'_i\}} \left(\sum_{j_{n+1}, j'_{n+1}} B_{\alpha_n, \alpha_{n+1}}^{j_{n+1}*} W_{\beta_n, \beta_{n+1}}^{j_{n+1}, j'_{n+1}} B_{\alpha'_n, \alpha'_{n+1}}^{j'_{n+1}} \right) \dots \times \left(\sum_{j_L, j'_L} B_{\alpha_{L-1}, 1}^{j_L*} W_{\beta_{L-1}, 1}^{j_L, j'_L} B_{\alpha'_{L-1}, 1}^{j'_L} \right) \quad (4.5)$$

From these contractions, the tripartite structure of the Hamiltonian matrix element, as seen in figure 4.1, can be written in a compact way

$$\langle \alpha_{n-1} j_n \alpha_n | \hat{H} | \alpha'_{n-1} j'_n \alpha'_n \rangle = \sum_{\beta_{n-1}, \beta_n} L_{\alpha_{n-1}, \beta_{n-1}, \alpha'_{n-1}} W_{\beta_{n-1}, \beta_n}^{j_n, j'_n} R_{\alpha_n, \beta_n, \alpha'_n} . \quad (4.6)$$

Finally, applying the Hamiltonian in the $\{|\alpha_{n-1}\rangle, |j_n\rangle, |\alpha_n\rangle\}$ basis to the MPS of eq. (4.2) yields [58]

$$\hat{H} |\psi\rangle = \sum_{\beta_{n-1}, \beta_n} \sum_{\alpha'_{n-1}, j'_n, \alpha'_n} L_{\alpha_{n-1}, \beta_{n-1}, \alpha'_{n-1}} W_{\beta_{n-1}, \beta_n}^{j_n, j'_n} R_{\alpha_n, \beta_n, \alpha'_n} \Psi_{\alpha'_{n-1}, \alpha'_n}^{j'_n} |\alpha_{n-1}\rangle_A |j_n\rangle | \alpha_n\rangle_B . \quad (4.7)$$

Expressing \hat{H} in the basis of the block states exposes the central site of the MPS such that it can be varied in a ground state search. Evaluating $\hat{H} |\psi\rangle$ must be done many times during a variational search of the ground state, hence this operation must be executed as fast as possible. Examining eq. (4.7) one will notice, that while the boundaries of L and R will change depending on which site is being optimized, the bulk of the two tensors remain constant through a lot of the calculations. Instead of calculating L and R from eq. (4.4) and (4.5) for every evaluation of eq. (4.7), one can iteratively build them, since they only change by one column of the network at a time. Thus, a large number of computations can be reused.

Consider the construction of the tensor $L^{[i]}$, which can be built iteratively from the left by contracting the previous left-tensor $L^{[i-1]}$ with the i 'th column of the network consisting of $A^{[i]}$, $W^{[i]}$ and $A^{[i]\dagger}$

$$L_{\alpha_i, \beta_i, \alpha'_i}^{[i]} = \sum_{\substack{j_i, j'_i \\ \alpha_{i-1}, \beta_{i-1}, \alpha'_{i-1}}} W_{\beta_{i-1}, \beta_i}^{[i]j_i, j'_i} \left(A^{[i]j_i\dagger} \right)_{\alpha_i, \alpha_{i-1}} L_{\alpha_{i-1}, \beta_{i-1}, \alpha'_{i-1}}^{[i-1]} A_{\alpha'_{i-1}, \alpha'_i}^{[i]j'_i}. \quad (4.8)$$

The iterative update of $L^{[i]}$ can be seen illustrated in figure 4.2. The square-bracket notation has been re-introduced to keep track of the tensors relation to the physical sites. In order to remain consistent with notation, the dummy scalars $L_{\alpha_0, \beta_0, \alpha'_0}^{[0]} = 1 = \alpha_0, \beta_0, \alpha'_0$ have been introduced.

It is important to store every iteration of $L^{[i]}$, since L will grow and shrink constantly

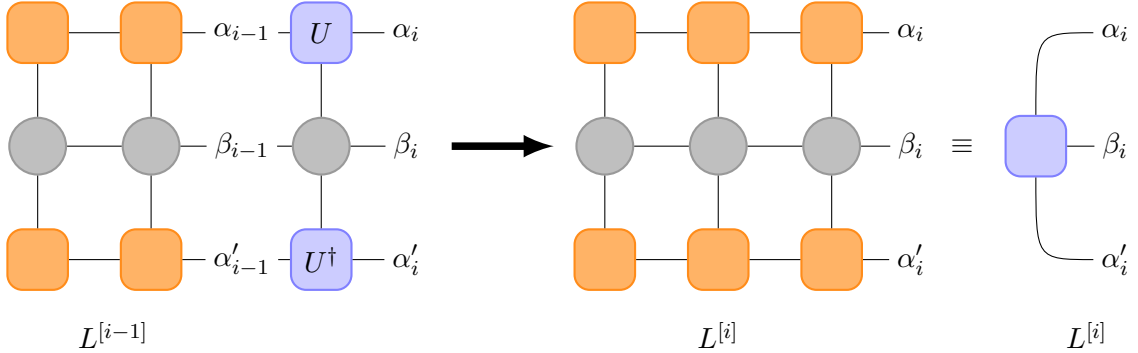


FIGURE 4.2: Iterative update from $L^{[i-1]}$ to $L^{[i]}$ through a contraction of $L^{[i-1]}$ with $A^{[i]}$, $W^{[i]}$ and $A^{[i]\dagger}$. The result is a tensor with three horizontal legs.

throughout the variational search of the ground state, whereby every iteration of $L^{[i]}$ will be used multiple times. The same applies when building the right environment, R . Here one starts from the right and moves left when iteratively contracting the tensor. By applying optimal bracketing, the computational cost of updating the environments scales as $O(dD^3D_W)$.

4.1.2 Iterative Ground State Search and the DMRG Algorithm

In order to find the ground state of the system one can introduce a Lagrangian multiplier, λ , and extremize

$$\langle \psi | \hat{H} | \psi \rangle - \lambda \langle \psi | \psi \rangle, \quad (4.9)$$

whereby the desired ground state, $|\psi\rangle$, and ground state energy, λ^0 , will be reached.

Trying to optimize an entire MPS at once is a highly non-linear problem involving an extremely large number of variables. However, the problem can be linearised by only considering the variables of a single tensor (site) at a time, while keeping the rest of the MPS constant. By varying just a single tensor at a time, one will continuously find states lower in energy, until convergence is reached. However, this procedure is very prone to getting stuck in a local extrema. To circumvent this, one can consider two sites at a time and optimize with regards to a two-site tensor, created by momentarily merging the two sites [75].

Consider the variation of the tensors $M^{[n]}$ and $M^{[n+1]}$. Expressing the minimization problem

of eq. (4.9) in terms of the left and right environments (as done in eq. (4.7)) yields

$$\begin{aligned} \langle \psi | \hat{H} | \psi \rangle = & \sum_{j_n, j'_n} \sum_{\alpha'_{n-1}, \alpha'_n, \alpha'_{n+1}} \sum_{\alpha_{n-1}, \alpha_n, \alpha_{n+1}} \sum_{\beta_{n-1}, \beta_n, \beta_{n+1}} L_{\alpha_{n-1}, \beta_{n-1}, \alpha'_{n-1}}^{[n-1]} W_{\beta_{n_1}, \beta_n}^{j_n, j'_n} W_{\beta_n, \beta_{n+1}}^{j_{n+1}, j'_{n+1}} \\ & \times R_{\alpha_{n+1}, \beta_{n+1}, \alpha'_{n+1}}^{[n+2]} M_{\alpha_{n-1}, \alpha_n}^{j_n} M_{\alpha'_{n-1}, \alpha'_n}^{j'_n *} M_{\alpha_n, \alpha_{n+1}}^{j_{n+1}} M_{\alpha'_n, \alpha'_{n+1}}^{j'_{n+1} *} \end{aligned} \quad (4.10)$$

with the overlap

$$\begin{aligned} \langle \psi | \psi \rangle = & \sum_{j_n, j_{n+1}} \sum_{\alpha'_{n-1}} \sum_{\alpha_{n-1}, \alpha_n, \alpha_{n+1}} \Psi_{\alpha_{n-1}, \alpha'_{n-1}}^A M_{\alpha_{n-1}, \alpha_n}^{j_n} M_{\alpha'_{n-1}, \alpha'_n}^{j'_n *} \\ & \times M_{\alpha_n, \alpha_{n+1}}^{j_{n+1}} M_{\alpha'_n, \alpha'_{n+1}}^{j'_{n+1} *} \Psi_{\alpha_{n+1}, \alpha'_{n+1}}^B, \end{aligned} \quad (4.11)$$

where the Hamiltonian from eq. (4.7) has been re-ordered to accommodate examining two sites, n and $n + 1$, at a time, and

$$\Psi_{\alpha_{n-1}, \alpha'_{n-1}}^A = \sum_{j_1, \dots, j_{n-1}} \left(M^{j_{n-1}\dagger} \dots M^{j_1\dagger} M^{j_1} \dots M^{j_{n-1}} \right)_{\alpha_{n-1}, \alpha'_{n-1}} \quad (4.12)$$

$$\Psi_{\alpha_{n+1}, \alpha'_{n+1}}^B = \sum_{j_{n+2}, \dots, j_L} \left(M^{j_{n+2}} \dots M^{j_L} M^{j_L\dagger} \dots M^{j_{n+2}\dagger} \right)_{\alpha'_{n+1}, \alpha_{n+1}}. \quad (4.13)$$

Further simplifications can be made for mixed-canonical forms, if sites 1 through $n - 1$ are left-normalized, and sites $n + 2$ through L are right-normalized, whereby

$$\Psi_{\alpha_{n-1}, \alpha'_{n-1}}^A = \delta_{\alpha_{n-1}, \alpha'_{n-1}}, \quad \Psi_{\alpha_{n+1}, \alpha'_{n+1}}^B = \delta_{\alpha_{n+1}, \alpha'_{n+1}}. \quad (4.14)$$

Finding the extremum of eq. (4.9) with respect to $M_{\alpha'_{n-1}, \alpha'_n}^{[n]j'_n *} M_{\alpha'_n, \alpha'_{n+1}}^{[n+1]j'_{n+1} *}$ is done through the following sequence:

Two-site update for iterative ground state search

1. **Merge:** Contract the two matrices $M^{[n]}$ and $M^{[n+1]}$ over the bond α_n creating a two-site tensor

$$\Theta_{\alpha_{n-1}, \alpha_{n+1}}^{j_n, j_{n+1}} = \sum_{\alpha_n} M_{\alpha_{n-1}, \alpha_n}^{[n]j_n} M_{\alpha_n, \alpha_{n+1}}^{[n+1]j_{n+1}} \quad (4.15)$$

2. **Solve eigenproblem:** This yields an eigenvalue problem, which can be seen by reshaping

$$\begin{aligned} H_{(\alpha_{n-1} j_n j_{n+1}, \alpha_{n+1}), (\alpha'_{n-1} j'_n j'_{n+1}, \alpha'_{n+1})} = & \\ = & \sum_{\beta_{n-1}, \beta_n} L_{\alpha_{n-1}, \beta_{n-1}, \alpha'_{n-1}}^{[n-1]} W_{\beta_{n_1}, \beta_n}^{[n]j_n, j'_n} W_{\beta_n, \beta_{n+1}}^{[n+1]j_{n+1}, j'_{n+1}} R_{\alpha_{n+1}, \beta_{n+1}, \alpha'_{n+1}}^{[n+2]} \end{aligned} \quad (4.16)$$

and

$$v_{\alpha_{n-1} j_n j_{n+1} \alpha_{n+1}} = \Theta_{\alpha_{n-1}, \alpha_{n+1}}^{j_n, j_{n+1}} \quad (4.17)$$

such that

$$Hv - \lambda v = 0. \quad (4.18)$$

Solving eq. (4.18) for the lowest eigenvalue λ_0 yields $v_{\alpha_{n-1}j_n j_{n+1} \alpha_{n+1}}^0$, which can be reshaped back to the now optimized two-site tensor, $\tilde{\Theta}_{\alpha_{n-1}, \alpha_{n+1}}^{j_n, j_{n+1}}$.

3. **Unmerge:** Reshape the updated $\tilde{\Theta}_{\alpha_{n-1}, \alpha_{n+1}}^{j_n, j_{n+1}}$ to a matrix and perform an SVD yielding

$$\tilde{\Theta}_{(j_n \alpha_{n-1}), (j_{n+1} \alpha_{n+1})} = \sum_{\alpha_n} U_{\alpha_{n-1}, \alpha_n}^{j_n} S_{\alpha_n, \alpha_n} (V^\dagger)_{\alpha_n, \alpha_{n+1}}^{j_{n+1}}. \quad (4.19)$$

This causes the bond dimension to increase $D \rightarrow dD$, which must be truncated by keeping only the D largest singular values of S .

4. **Update environments:** The last step depends on which direction, one is iterating through the chain. Here, the left- and right-normalization of U and V^\dagger is used to update the environments.

Going right: Update the left environment

$$\tilde{L}_{\alpha_n, \beta_n, \alpha'_n}^{[n]} = \sum_{\substack{j_n, j'_n \\ \alpha_{n-1}, \beta_{n-1}, \alpha'_{n-1}}} L_{\alpha_{n-1}, \beta_{n-1}, \alpha'_{n-1}}^{[n-1]} U_{\alpha_{n-1}, \alpha_n}^{j_n} W_{\beta_{n-1}, \beta_n}^{[n]j_n, j'_n} U_{\alpha'_{n-1}, \alpha'_n}^{j'_n*}, \quad (4.20)$$

and build the matrix of the right site

$$\tilde{M}_{\alpha_n, \alpha_{n+1}}^{[n+1]j_{n+1}} = \sum_{\alpha_n} S_{\alpha_n, \alpha_n} (V^\dagger)_{\alpha_n, \alpha_{n+1}}^{j_{n+1}}. \quad (4.21)$$

Going left: Update the right environment

$$\tilde{R}_{\alpha_n, \beta_n, \alpha'_n}^{[n+1]} = \sum_{\substack{j_{n+1}, j'_{n+1} \\ \alpha_{n+1}, \beta_{n+1}, \alpha'_{n+1}}} R_{\alpha_{n+1}, \beta_{n+1}, \alpha'_{n+1}}^{[n+2]} \left(V^\dagger\right)_{\alpha_n, \alpha_{n+1}}^{j_{n+1}} W_{\beta_n, \beta_{n+1}}^{[n+1]j_{n+1}, j'_{n+1}} \left(V^\dagger\right)_{\alpha_n, \alpha_{n+1}}^{j_{n+1}*}, \quad (4.22)$$

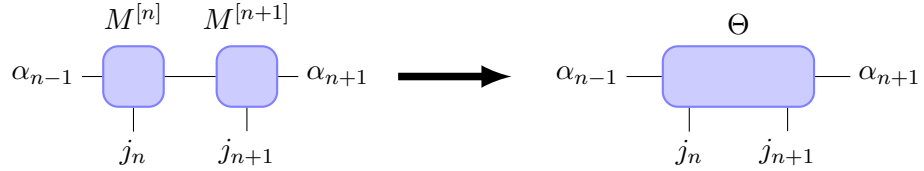
and build the matrix of the left site

$$\tilde{M}_{\alpha_{n-1}, \alpha_n}^{[n]j_n} = \sum_{\alpha_n} U_{\alpha_{n-1}, \alpha_n}^{j_n} S_{\alpha_n, \alpha_n}. \quad (4.23)$$

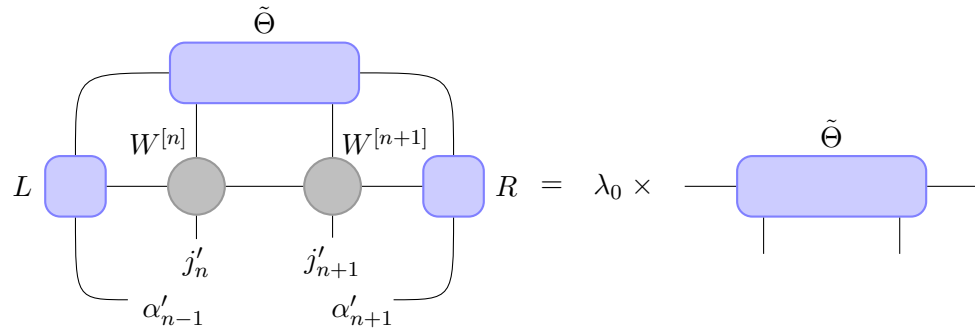
This concludes the two-site update sequence, which is illustrated in figure 4.3. After performing the sequence, one can move *one site* to either left or right, depending on which direction one is iterating.

Some comments regarding the sequence are in order: The matrices of the eigenvalue problem have dimensions $(d^2 D^2 \times d^2 D^2)$, which is generally too much for exact diagonalization, however, since only the lowest eigenvalue is of interest, one can use an iterative eigensolver [37]. Furthermore, if the MPS is not in the proper mixed-canonical form, the eigenvalue problem turns into a generalized eigenvalue problem, which can be numerically quite demanding. Thus, updating the left and right environments in step (4) is necessary, since it leads to great simplifications in step (2). Lastly, one could also consider just a single site when updating, however, this method is very prone to getting stuck [77]. By updating two sites at once, one actually optimizes the bond between them. Hence, after updating the two sites, one must only iterate a single site. Optimization is done with regards to the current configuration, whereby it depends on previous updates. To compensate for this, one must sweep through the entire system multiple times, which leads to the following algorithm for iterative ground state search, which follows the structure of the DMRG algorithm:

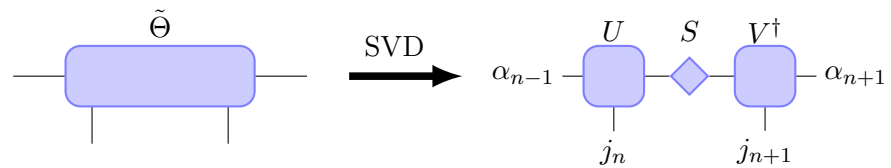
(1) Merge:



(2) Solve eigenproblem:



(3) Unmerge:



(4) Update environments:

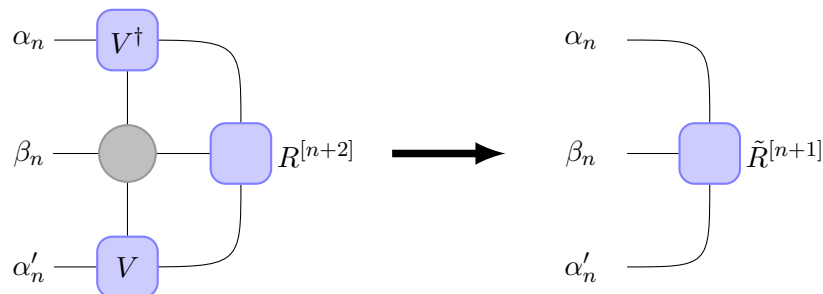
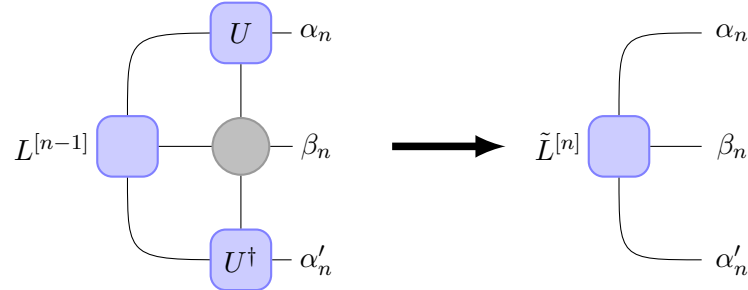


FIGURE 4.3: Diagrammatic representation of the two-site update sequence for iterative ground state search. Step (2) optimizes with regard to two sites, but only a single site is updated to avoid getting stuck. In step (4), when iterating left-to-right in the lattice, the left environment, $L^{[n]}$, is updated. The right environment, $R^{[n]}$, is updated when moving right-to-left.

Algorithm 3 Iterative ground state search (DMRG)

```

Choose  $|\psi\rangle$  right-normalized.
Calculate tensor  $R^{[i]}$  iteratively for  $i = L \dots 1$ .
while Stopping criteria not met do
    for  $n = 1 \dots L - 1$  do                                 $\triangleright$  Left sweep
        Perform two-site update on  $M^{[n]}$  and  $M^{[n+1]}$ .
        Update  $L^{[n]}$  according to eq. (4.20)
    end for
    for  $n = L - 1 \dots 1$  do                             $\triangleright$  Right sweep
        Perform two-site update on  $M^{[n]}$  and  $M^{[n+1]}$ .
        Update  $R^{[n]}$  according to eq. (4.22)
    end for
end while

```

Examples of the DMRG algorithm can be found in section 3.6.1, where the ground state of the Bose-Hubbard model is calculated for a lattice with 50 sites. The ground state is used to compute correlation functions of the system, and the example illustrates how matrix product states and the DMRG algorithm struggle when the correlation lengths grow very large. Another example can be found in appendix D, where the condensate fraction for various system sizes is computed in an attempt to determine the point of the superfluid to Mott-Insulator phase transition. Furthermore, the results obtained through the DMRG are compared with those of exact diagonalization.

4.2 Time Evolution of Matrix Product States

A central component of optimal control is time evolution. In order to compute any optimal control sequence, it is crucial to have a fast and accurate time evolution algorithm. However, also the construction of the time evolution operator must be taken into account, as exponentiating operators with terms acting on multiple sites, such as the Bose-Hubbard Hamiltonian, is a costly operation. Thus, both an efficient time evolution algorithm and an efficient operator exponentiation is needed when performing optimal control.

Several algorithms for time evolving matrix product states exist, however, they all origin from the same ideas proposed in [69, 70]. The most widely used of these algorithms is the tDMRG algorithm, which gets its name from its similarity with the ground state search algorithm described in section 4.1.2. The tDMRG algorithm has been utilized in several instances to simulate the dynamics of one-dimensional systems CITE, and it has even been previously used in conjunction with the CRAB algorithm to perform optimal control of the superfluid to Mott-Insulator phase transition [67, 15].

Although the standard algorithms for time evolution are quite efficient, further improvements can be made to the algorithms by tailoring them to the problem at hand. Therefore, a modified version of the tDMRG algorithm is proposed in Section 4.2.2, which directly utilizes the properties of the Bose-Hubbard Hamiltonian.

4.2.1 The tDMRG Algorithm

Consider the time evolution of a quantum state

$$|\psi(t)\rangle = \hat{\mathcal{U}}(t) |\psi(0)\rangle , \quad (4.24)$$

where $\hat{\mathcal{U}}(t) = e^{-i\hat{H}t}$ is the time evolution operator. Time evolution of a matrix product states is done in a manner similar to that of ground state search, as the bonds between the tensors are evolved rather than the tensors themselves. Thus, the time evolution operator must be decomposed into two-site tensors. The simplest realization of this is achieved by considering a Hamiltonian containing only nearest-neighbour interactions. Assume the Hamiltonian is a sum of two-site operators of the form $\hat{H} = \sum_n \hat{h}^{[n,n+1]}$. One can decompose this into a sum over even and odd bonds

$$\hat{H} = \hat{H}_{\text{odd}} + \hat{H}_{\text{even}} = \sum_{n \text{ odd}} \hat{h}^{[n,n+1]} + \sum_{n \text{ even}} \hat{h}^{[n,n+1]}. \quad (4.25)$$

Exponentiating the Hamiltonian is non-trivial due to the non-commutativity of the operators

$$[\hat{h}_{\text{odd}}^{[n,n+1]}, \hat{h}_{\text{even}}^{[n,n+1]}] \neq 0. \quad (4.26)$$

Considering a small time slice, Δt , the exponentiation can be achieved through the Trotter-Suzuki expansion [65]. To first order this reads

$$e^{-i\hat{H}\Delta t} = e^{-i\hat{H}_{\text{odd}}\Delta t} e^{-i\hat{H}_{\text{even}}\Delta t} + O(\Delta t^2), \quad (4.27)$$

where the error is due to the non-commutativity of the bond Hamiltonians. Thus, the time evolution operator can be expressed as the product

$$\hat{\mathcal{U}}(\Delta t) \approx \left(\prod_{n \text{ odd}} \hat{\mathcal{U}}^{[n,n+1]}(\Delta t) \right) \left(\prod_{n \text{ even}} \hat{\mathcal{U}}^{[n,n+1]}(\Delta t) \right), \quad (4.28)$$

where

$$\hat{\mathcal{U}}^{[n,n+1]}(\Delta t) = e^{-i\hat{h}^{[n,n+1]}\Delta t}. \quad (4.29)$$

The result is an MPO performing an infinitesimal time step on the odd bonds, and another MPO evolving the even bonds. An illustration of eq. (4.28) is shown in Figure 4.4. The

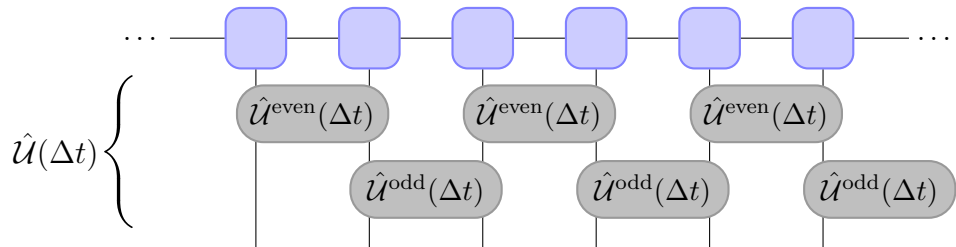


FIGURE 4.4: Approximation of each time step δt using a Trotter-Suzuki decomposition, such that the time evolution operator is expressed as a product of unitary two-site operators.

tDMRG algorithm describes the most efficient and accurate way of contracting the tensor network detailed in figure 4.4. The algorithm gets its name from its similarity with the DMRG algorithm detailed in section 4.1.2. In fact, the merge and unmerge procedure of the two algorithms is completely identical, whereby they only differ in the steps of applying the operator and proceeding to the next site. The following procedure details a time evolution step of the n 'th bond [58].

Infinitesimal time-step update for tDMRG

1. **Merge:** Contract tensors $M^{[n]}$ and $M^{[n+1]}$ over the bond α_n creating a two-site tensor $\Theta^{j_n, j_{n+1}}$.

2. **Apply unitary:** The two-site time evolution operator, $\hat{\mathcal{U}}^{[n,n+1]}$, is applied to $\Theta^{j_n,j_{n+1}}$

$$\tilde{\Theta}_{\alpha_{n-1},\alpha_{n+1}}^{j_n,j_{n+1}} = \sum_{j'_n,j'_{n+1}} \mathcal{U}^{j_n j_{n+1}, j'_n j'_{n+1}} \Phi_{\alpha_{n-1},\alpha_{n+1}}^{j'_n,j'_{n+1}}. \quad (4.30)$$

3. **Unmerge:** Reshape $\tilde{\Phi}_{\alpha_{n-1},\alpha_{n+1}}^{j'_n,j'_{n+1}}$ to a matrix and decompose it through an SVD. Applying $\hat{\mathcal{U}}^{[n,n+1]}$ causes an increase in bond dimension, $D \rightarrow d^2 D$, which must be truncated by keeping only the D largest singular values from the SVD.

4. **Progress:** Next, the center cite of the MPS must be shifted by two, in order to update the next even (odd) bond. This is achieved by merging tensors $M^{[n+1]}$ and $M^{[n+2]}$ and performing a second SVD, while reshaping the resulting U -matrices to left-normalised tensors to retain the canonical form. The product of the second SVD must be truncated as well, however, no loss of information will occur, as the Schmidt rank of the matrix S will be at most D following the first SVD.

Following the procedure above will leave the MPS in position for application of the unitary $\hat{\mathcal{U}}^{[n+2,n+3]}$. The efficiency of the tDMRG algorithm depends on the sequence in which bonds are evolved. A simple, yet effective way is iterating from left to right when evolving even bonds, while iterating right to left when evolving odd bonds. Thereby, the centered cite of the mixed-canonical form is moved continuously through the MPS, rather than having to be reset when reaching the end of the system.

Although the tDMRG algorithm is a very powerful algorithm, an even higher efficiency can be achieved when tailoring the algorithm to the system, which in this case is the Bose-Hubbard model. Thus, the Hamiltonian contains both nearest-neighbour and on-site terms. Furthermore, the Hamiltonian is time dependent, since the lattice depth is varied. The following algorithm is a modification of the tDMRG algorithm, which is tailored for conducting optimal control using the Bose-Hubbard Hamiltonian.

4.2.2 Modified Time Evolution Algorithm for Optimal Control

The optimization of the control causes the Hamiltonian to be altered multiple times. Hence, the propagator for the time-evolution must be re-calculate often, which can have a large numerical cost depending on the form of the Hamiltonian. A general operator \hat{W} can be exponentiated through the series expansion

$$\exp(\hat{W}) = \sum_{k=0}^{\infty} \frac{\hat{W}^k}{k!} = \hat{1} + \hat{W} \left(\hat{1} + \frac{\hat{W}}{2} \left(\hat{1} + \frac{\hat{W}}{3} \left(\dots \right) \right) \right) \quad (4.31)$$

The number of terms needed in the expansion to accurately describe the exponentiation depends on the operator. Performing the exponentiation through a series expansion is a relatively expensive operator. Therefore, it is crucial to find an easier way of constructing the time evolution operator. One method is by considering the form of the Bose-Hubbard Hamiltonian. The most natural choice of control parameter is the lattice depth, V_0 , as is the experimentally controllable parameter. The lattice depth determines both the tunneling matrix element, J (eq. (1.37)), and the interaction matrix element, U (eq. (1.40)), and has served as control parameter in other studies [67, 15]. Unfortunately, exponentiating the hopping terms of the Bose-Hubbard Hamiltonian is a relatively costly computation. Therefore, it was concluded that keeping J fixed and using U as the control parameter was the better option. Due to the diagonal form of the number operator, \hat{n}_i , the exponentiation of the interaction term can be built directly without the need for the series expansion

of eq. (4.31). However, simply exponentiating the different terms of the Bose-Hubbard Hamiltonian separately is not possible, as the operators do not commute. Therefore, one must expand the time evolution operator into its components through the Suzuki-Trotter expansion. To second order the Suzuki-Trotter expansion reads

$$\exp\left((\hat{V} + \hat{W})\delta\right) = \exp\left(\hat{V}\delta/2\right)\exp\left(\hat{W}\delta\right)\exp\left(\hat{V}\delta/2\right) + O(\delta^3). \quad (4.32)$$

Once again, the error is due to the non-commutativity of operators. Thus, the time evolution operator can be divided into a sequence of tensors, where

$$\hat{U}_J^{[i,i+1]} = \exp\left(-iJ(\hat{a}_i^\dagger \hat{a}_{i+1} + \hat{a}_{i+1}^\dagger \hat{a}_i)\Delta t\right) \quad (4.33)$$

$$\hat{U}_U^{[i]} = \exp\left(-i\frac{U}{2}\hat{n}_i(\hat{n}_i - 1)\Delta t/2\right). \quad (4.34)$$

A single time step, Δt , using the expanded operator is represented diagrammatically in

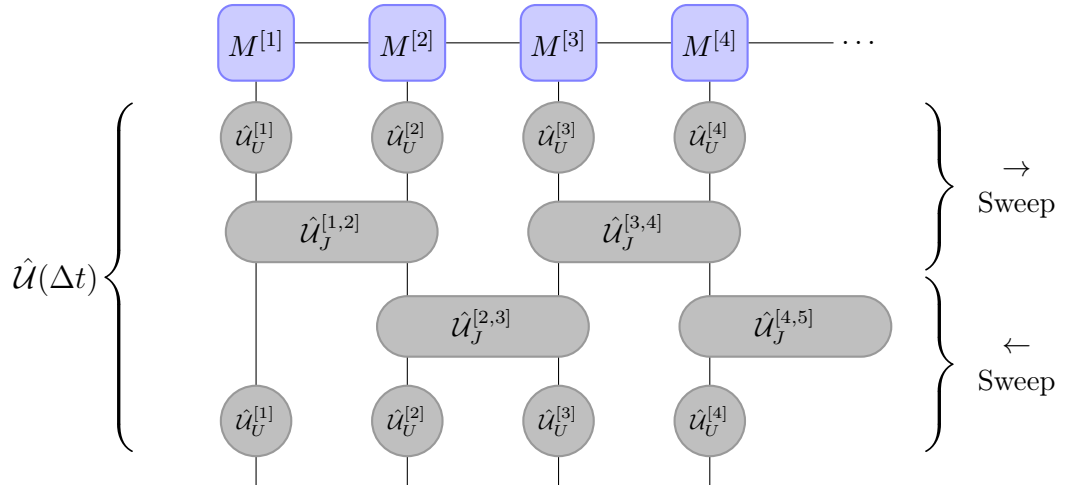


FIGURE 4.5: Tensor diagram depicting a single time step of the modified rDMRG algorithm. The time evolution operator has been subjected to a Suzuki-Trotter expansion as detailed in eq. (4.32). The tensors of the upper part of the network are contracted with the MPS while sweeping from left to right, whereas the lower part is applied with a right-to-left sweep.

figure 4.5. At first glance, the tensor network resulting from the Suzuki-Trotter expansion may seem rather extensive, however, it can be contracted in a very efficient manner. The upper part of the network is contracted in a left-to-right sweeping manner, where the position of the center cite, and thereby the normalisation of the MPS, is pushed to the right following each step. Likewise, the lower part of the network is contracted though a right-to-left sweep such that the MPS returns to its original form centered on the first site after applying the final operator. Thereby, the MPS is immediately ready for the subsequent time-propagation.

The sequence of contractions of the left-to-right sweep is shown in figure 4.6. The MPS is initially centered on the first tensor, while its remaining tensors are right-normalised. By contracting the bonds marked with a bold line shown in step 1 and 2, the operators are efficiently applied to the MPS. In the third step, the two-site tensor, Θ , is split using an SVD, where the bond dimension of the tensors is truncated. This is crucial in order to maintain a reduced dimensionality, which would otherwise result in a significant increase in contraction time. In the final and fourth step, the central cite of the MPS is moved to the start of the next two-site operator through another site merge and subsequent SVD. This step is exactly as in the original tDMRG algorithm. Thereby the normalization of the MPS

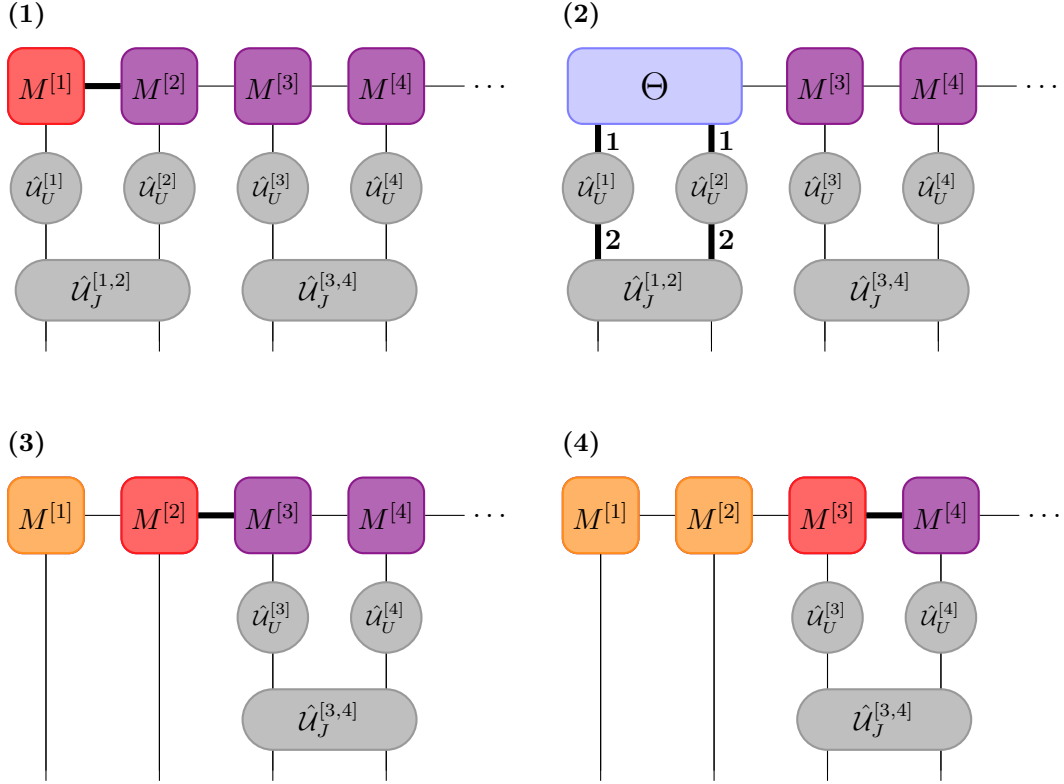


FIGURE 4.6: *Sequence of contractions for modified tDMRG algorithm during left to right sweep. Step (1): MPS is centered on site 1. Tensors $M^{[1]}$ and $M^{[2]}$ are contracted. Step (2): Two-site tensor, Θ , is contracted with operators in numbered sequence. The propagated two-site tensor is split using an SVD in step (3), followed by a contraction to the right. Lastly, in step (4), the two-site tensor of $M^{[2]}$ and $M^{[3]}$ is split using another SVD, whereby the center (and thereby the normalisation) is pushed to site 3.*

is "pushed" to the right and contained in a single site, which makes it easy to deal with in the end of the time evolution step.

As the center reaches the end of the MPS, the direction of the sweep is reversed. The right-to-left sweep is very similar to the sequence described above. The main difference is in the order of contractions, as the $\hat{U}_J^{[i,i+1]}$ -propagator is applied before $\hat{U}_U^{[i]}$. As the sweep, and thereby the central site, reaches the first site of the MPS, the central site is divided by its norm. Thereby the MPS is normalized and in the same configuration as before the time step. Thus, further propagations can be performed readily.

Additional precision is achieved when evaluating the control at the beginning and end points of the time interval [Steck2007]. Thus, the left-to-right sweep applies the operator $\hat{U}_{U(t)}^{[i]}$, while the right-to-left sweep applies $\hat{U}_{U(t+\Delta t)}^{[i]}$.

Gradient of Suzuki-Trotter propagator

In section 2.1 the derivative of the cost function with regards to the control was derived for a general propagator. However, expanding the propagator using the Suzuki-Trotter expansion while having a diagonal control Hamiltonian causes all higher order contributions to the gradient to drop out. Instead, the precision of the gradient is solely determined by the order of the expansion.

Consider the gradient entries for the cost function derived in section 2.1

$$\frac{\partial J}{\partial u_n(t_j)} = -\text{Re} \left\langle \chi(t_j) \left| i \frac{\partial \hat{\mathcal{U}}_j}{\partial u_n(t_j)} \right| \psi(t_{j-1}) \right\rangle, \quad (4.35)$$

where the derivative of a general propagator with respect to the control is given by

$$\frac{\partial \hat{\mathcal{U}}_j}{\partial u_n(t_j)} = e^{-i\hat{H}(u_n(t_j))\Delta t} \sum_{k=0}^{\infty} \frac{i^{k-1} \Delta t^{k+1}}{(k+1)!} \left[\hat{H}(u_n(t_j)), \frac{\partial \hat{H}(u_n(t_j))}{\partial u_n(t_j)} \right]_k. \quad (4.36)$$

The algorithm in this instance employs a Suzuki-Trotter expansion of the propagator while considering the control at both start and end of the step. For cleaner notation the Hamiltonian, which in this case is the Bose-Hubbard Hamiltonian of eq. (1.39), will be parametrized as $\hat{H}(U(t_j)) \equiv \hat{H}_J + U(t_j)\hat{H}_U$. Note, that the control in this instance is the interaction strength, $u_n(t_j) \equiv U(t_j)$. Thus, the full propagator reads

$$\hat{\mathcal{U}}_j^{\text{ST}} = \exp(-iU(t_j)\hat{H}_U\Delta t/2) \exp(-i\hat{H}_J\Delta t) \exp(-iU(t_{j-1})\hat{H}_U\Delta t/2) \equiv \hat{\mathcal{U}}_j^U \hat{\mathcal{U}}_j^J \hat{\mathcal{U}}_{j-1}^U. \quad (4.37)$$

Since the control at times t_j and t_{j-1} contribute to $\hat{\mathcal{U}}_j^{\text{ST}}$, the elements of the cost gradient are

$$\frac{\partial J}{\partial U(t_j)} = -\text{Re} \left\langle \chi(t_j) \left| i \frac{\partial \hat{\mathcal{U}}_j^{\text{ST}}}{\partial U(t_j)} \right| \psi(t_{j-1}) \right\rangle - \text{Re} \left\langle \chi(t_{j+1}) \left| i \frac{\partial \hat{\mathcal{U}}_{j+1}^{\text{ST}}}{\partial U(t_j)} \right| \psi(t_j) \right\rangle. \quad (4.38)$$

Further examining the derivative of the first propagator reveals

$$\begin{aligned} \frac{\partial \hat{\mathcal{U}}_j^{\text{ST}}}{\partial U(t_j)} &= \frac{\partial \hat{\mathcal{U}}_j^U}{\partial U(t_j)} \hat{\mathcal{U}}_j^J \hat{\mathcal{U}}_{j-1}^U \\ &= \exp(-iU(t_j)\hat{H}_U\Delta t/2) \sum_{k=0}^{\infty} \frac{i^{k-1} \Delta t^{k+1}}{(k+1)!} \left[U(t_j)\hat{H}_U, \hat{H}_U \right]_k \hat{\mathcal{U}}_j^J \hat{\mathcal{U}}_{j-1}^U \\ &= (-i\hat{H}_U\Delta t/2) \exp(-iU(t_j)\hat{H}_U\Delta t/2) \hat{\mathcal{U}}_j^J \hat{\mathcal{U}}_{j-1}^U \\ &= (-i\hat{H}_U\Delta t/2) \hat{\mathcal{U}}_j^{\text{ST}}. \end{aligned} \quad (4.39)$$

Since \hat{H}_U is diagonal, the following relation apply for the recursive commutator

$$\left[U(t_j)\hat{H}_U, \hat{H}_U \right]_k = \begin{cases} \hat{H}_U, & \text{if } k = 0. \\ 0, & \text{otherwise.} \end{cases}, \quad (4.40)$$

which causes all higher-order contributions to the derivative of the propagator to drop out. Likewise, the derivative of the second propagator is

$$\frac{\partial \hat{\mathcal{U}}_{j+1}^{\text{ST}}}{\partial u_n(j)} = \hat{\mathcal{U}}_{j+1}^{\text{ST}} \left(-i\hat{H}_U\Delta t/2 \right). \quad (4.41)$$

Inserting the derivatives of eq. (4.39) and (4.41) into the derivative of the cost (eq. (4.38)) yields

$$\begin{aligned} \frac{\partial J}{\partial U(t_j)} &= -\operatorname{Re} \left\langle \chi(t_j) \left| \left(\hat{H}_U \Delta t / 2 \right) \hat{U}_j^{\text{ST}} \right| \psi(t_{j-1}) \right\rangle - \operatorname{Re} \left\langle \chi(t_{j+1}) \left| \hat{U}_{j+1}^{\text{ST}} \left(\hat{H}_U \Delta t / 2 \right) \right| \psi(t_j) \right\rangle \\ &= -\operatorname{Re} \left\langle \chi(t_j) \left| \hat{H}_U \Delta t / 2 \right| \psi(t_j) \right\rangle - \operatorname{Re} \left\langle \chi(t_j) \left| \hat{H}_U \Delta t / 2 \right| \psi(t_j) \right\rangle \\ &= -\operatorname{Re} \left\langle \chi(t_j) \left| \hat{H}_U \Delta t \right| \psi(t_j) \right\rangle. \end{aligned} \quad (4.42)$$

Thus, the combination of the Suzuki-Trotter expansion and a diagonal control Hamiltonian eliminates all higher order contributions to the gradient. Thereby, the gradient of the cost is exact up to the order of the expansion. A comparison between a numerically calculated

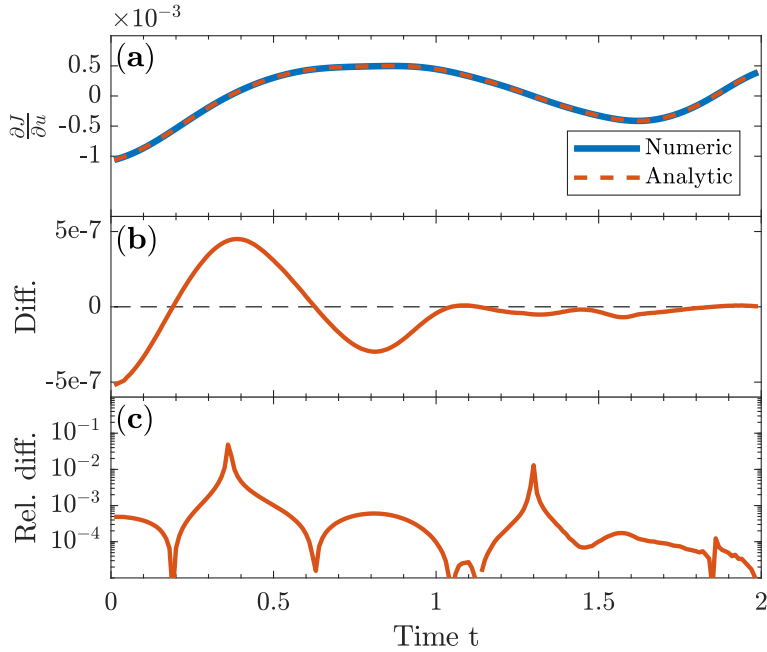


FIGURE 4.7: (a): Numerical gradient along with gradient calculated via eq. (4.42). (b): Difference between the two gradients. (c): Absolute relative difference between the two gradients.

gradient and the analytically derived gradient of eq. (4.42) can be seen in figure 4.7. The difference between the two gradients is largest at the beginning of the sequence, due to the accumulated error from the time evolution of $|\chi(0)\rangle$, which is derived from two time evolutions over the entire duration.

Time complexity of time-evolution algorithms

The Suzuki-Trotter expansion (4.32) does not determine the ordering of the operators. Thus, an alternative algorithm can be derived, where the half-step is taken using the $\hat{U}_J^{[i,i+1]}$ operator. However, applying the two-site operators is in general more time consuming than applying two single-site operator. A comparison between the run-times of various time-evolution algorithms in shown in Figure 4.8. The two tDMRG algorithms are the one described above using a half-step of \hat{U}_J and \hat{U}_U respectively. The MPO-based algorithm builds the propagator using ITensor library methods following [82], and the resulting MPO is applied to the MPS according to eq. (3.26). This method has an error of order $O(\Delta t^2)$, which is less accurate than the second-order Trotter expansion. In Section 3.5 the cost

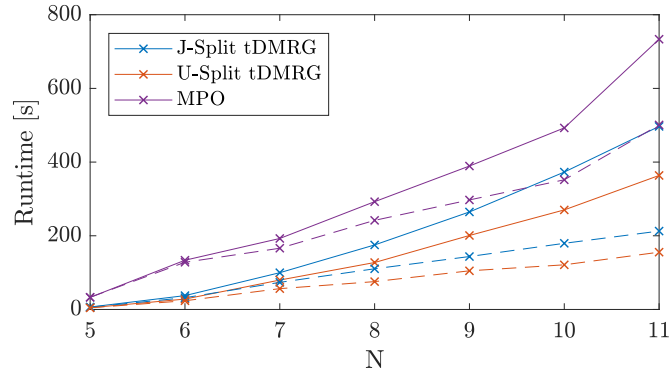


FIGURE 4.8: *Runtime of performing 100 time steps with various algorithms in Bose Hubbard system with unit occupancy. Solid lines are systems with a local Fock space of dimension N , while dashed lines are systems with a constant Fock space dimension of 5.*

of applying an MPO to an MPS was given by $O(Ld^2D_W^2D^2)$. Considering the single-site tensors of the tDMRG algorithms, D_W is zero. Since $d = L$ for the solid lines in Figure 4.8, the runtime of the algorithm will have a cubic scaling with the system size. However, a much better scaling can be achieved by truncating the local Hilbert space, such that d is kept constant resulting in a runtime scaling linearly with the system size. In the case of the Bose Hubbard model, eq. (1.39), the interaction term scales quadratically with the number of particles at a given site, which causes a huge energy penalty. Thus, for large systems with unit occupation, neglecting contributions from states with a majority of the particles at a single site is a reasonable approximation. Therefore, the modified tDMRG algorithm can be applied efficiently to very large systems, if the dimension of the physical index of the MPS is restricted to a reasonable fraction of the number of particles.

Chapter 5

Results

In this chapter the main results of the numerical investigation of the Bose-Hubbard superfluid to Mott-Insulator phase transition are presented. The framework set up for performing optimal control of lattice systems consist of multiple components working together:

The quantum state of the system is parametrized as a matrix product state (see Chapter 3), whereby the exponential scaling of the Hilbert space with system size can be avoided. Most of the tensor operations used are implemented in the ITensor library [64]. For time evolving the state a modified version of the tDMRG algorithm is employed (see Section 4.2.2), which is tailored specifically to the control problem. Quantum optimal control determines the best way to manipulate a set of external parameters in order to facilitate a state transfer $|\psi_0\rangle \rightarrow |\psi_{\text{target}}\rangle$. The boundary states are calculated initially using the DMRG algorithm (see Section 4.1.2) at the fixed control points $\mathbf{u}(0)$ and $\mathbf{u}(T)$, such that these states are guaranteed to be the ground state. The optimal set of control parameters needed for completing the state transfer with the highest possible fidelity is calculated using the GROUP algorithm described in Section 2.2. In each iteration of GROUP, the gradient of the cost functional is calculated using eq. (2.28), which utilizes the derivative of the Suzuki-Trotter expanded propagator given in eq. (4.42). The gradient is used to update the control through the Interior Point method (see Section 2.3). The version of the Interior Point method used here is implemented in IPOPT library [73].

In section 5.1 the optimal control framework is tested on a small lattice of 5 sites in order to gauge the dynamics of the system and determine suitable values of various parameters. The results from conducting optimal control of 20-site lattice with unit occupancy can be found in section 5.2.

5.1 Characterization of Methods on a Small System

To determine the optimal parameters and settings for the optimization, an initial analysis of a small system consisting of 5 sites with unit occupancy was made. Systems of different sizes are expected to evolve differently, especially due to the closed boundary conditions of the lattice, which have a greater impact for smaller systems. Although the dynamics are expected to vary with the lattice length, certain parameters such as the regularization factor, γ , and the dimension of the chopped basis, M , can be optimized using a smaller system. These parameters only affect the shape of the control pulse, which is subjected to constraints independent of the system size. Nevertheless, the optimal value of these parameters may change slightly with system size, since the shape of the optimal control pulse varies with both system size and optimization method used, as shown in [31].

5.1.1 Boundary Conditions

Section 1.3 describes how the Bose-Hubbard model is only well defined within the tight-binding limit. This is especially an issue for lattice depths below the limit, as the Wannier functions may start overlapping with the next-nearest neighbouring sites, thus facilitating two-site hopping, which is not accounted for in the model. Thus, the starting value of the control must be chosen with care. In [67, 15] initial lattice depths at $V_0(0) = 3E_{\text{rec}}$ and lower were chosen, where it was argued that the model is still a decent approximation at this depth. Hence, an initial control of $U/J(0) = 2$ was chosen for this analysis, which corresponds to a lattice depth around three recoil energies. In order to ensure the validity of the model, the minimum value of the control, which is enforced at all times during the pulse sequence, was set to the same value as the initial control. The final control was set to $(U/J)(T) = 50$ roughly corresponding to the final lattice depth of $V_0(T) = 14E_{\text{rec}}$ used in [67].

The initial and target state were calculated from the control parameter at the start and end of the duration respectively using the DMRG algorithm. Thus, the states are insured to be the ground state at each end of the duration, whereby the optimized state transfer will bring be between two ground states.

5.1.2 Seed Selection

The success of an optimization process is often dependent on the quality of the initial starting point or seed. Poor seeding strategies can lead to failure in finding optimal solutions when conducting local searches in complex optimization landscapes [62]. This has been demonstrated to occur in constrained quantum control problems [84], which is exactly the type of problem examined in this thesis. Hence, the type of seed used for the optimization must be chosen carefully.

Different adiabatic lattice ramps from the superfluid to Mott-Insulator phase were examined in [81]. The study concluded that ramping the lattice slowly around the point of the phase transition results in an improved final fidelity. A similar phenomenon can be found when considering an avoided crossing in a two-level system, $\{|1\rangle, |2\rangle\}$ due to an external perturbation. Here, $|1\rangle$ is the ground state in one asymptotic limit of the external parameter, while $|2\rangle$ is the ground state in the other limit. A transfer $|1\rangle \rightarrow |2\rangle$ can be achieved while remaining in the ground state by adiabatically sweeping over the external parameter, whereas a rapid change in the external parameter will result in the excited state being populated. Therefore, a ramp sequence was proposed in [81], which has an initial sigmoid shape followed by a slow increase in the lattice depth around the phase transition point. Following this, the lattice follows an exponential ramp to its final depth. Examining other attempts of optimizing the ramp sequence of the Bose-Hubbard model [15, 67] shows similar traits in their results. Therefore, choosing seeds with a slow ramp across the point of the phase transition followed by a rapid increase in lattice depth should yield good optimization results. Figure 5.1 shows the distribution of seeds used for the optimizations. Due to control parameter being the interaction strength of the Bose-Hubbard model, the phase transition occurs at quite a low control value. Hence, the initial part of the seed is a slowly increasing linear ramp, which crosses the point of the phase transition with a small slope. A shape function has been multiplied to the seeds enforcing a horizontal slope at the start and end of the duration, which helps avoiding any kinks in the control curve.

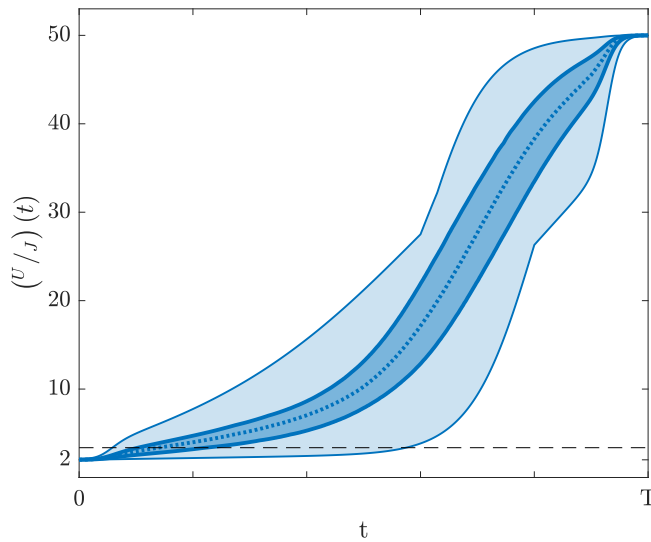


FIGURE 5.1: *Distribution of seeds used for optimization. All seeds lie within the lightly shaded region, while the darker region contains the 25-75 percentile of seeds. Lastly, the dotted line is the median value of the seed. The dashed line signifies the point of the Bose-Hubbard phase transition.*

5.1.3 Determining the Quantum Speed Limit

To illustrate the achieved fidelity's dependence on duration of the control sequence, a series of optimizations were made while scanning over the duration T . For this a regularization factor of $\gamma = 10^{-6}$ and an optimization space dimension of $M = 20$ were used. Since the control is parametrized using a linear combination of smooth functions, the effect of the regularization term is limited, however, it does help the optimization algorithm avoid greatly varying controls during its initial iterations. Lastly, a time-step of $\Delta t = 10^{-2}$ was chosen as a compromise between accuracy and runtime.

Figure 5.2 shows the final fidelities obtained for various durations from 100 different initial controls. In part 5.2.a the 25%- and 75%-quartiles along with the median of the solutions are displayed. At short durations the system can not evolve fast enough from the initial state to reach the target state, hence only low fidelities are obtained. However, as more and more time becomes available, fidelities very close to unit can be reached. Although the final fidelity does not appear to improve beyond $T = 3$, figure 5.2.b reveals the best solutions still improving at longer durations albeit at a reduced rate.

Compared to other figures of merit, the fidelity is a very strong measure, as it only considers the overlap with the target state. Due to the large number of quantum states in lattice systems, achieving unit fidelity is practically impossible, and even reaching high fidelities become increasingly difficult with system size. An alternative figure of merit was used for the optimal control of a Bose-Hubbard system presented in [67]. Instead of determining the convergence through the infidelity, a rescaled variance of the particle numbers in each of the central sites was used. This figure of merit is much less sensitive to the system size, however, it does have some less favorable properties: First, multiple particle configurations different from unit occupancy of each site can achieve a vanishing particle number variance. Furthermore, the pure state of a single particle on each lattice site only becomes the ground state as the lattice depth tends towards infinity. Therefore, the figure of merit used in [67] does not steer the state towards the ground state at the final control value, which could result in residual oscillations of the system after the control sequence. It should be noted

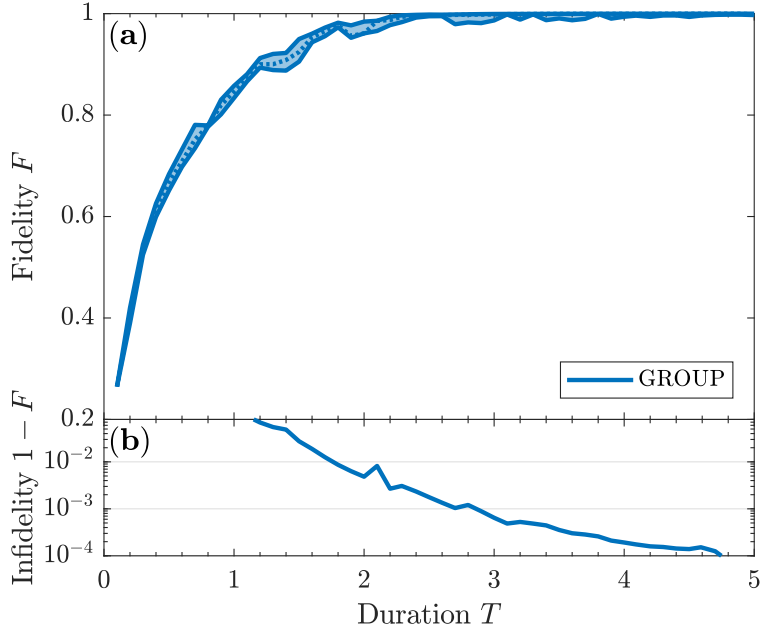


FIGURE 5.2: *Final fidelity obtained for optimal control at various durations. (a)* the dotted line marks the median fidelity achieved, while the shaded area displays the 25%- and 75%-quartiles of the solutions. *(b)* the lowest infidelity achieved for each duration.

that at the final control value used here, the state with a single particle at each site is a very good approximation of the ground state. Nevertheless, the fidelity is a more direct figure of merit, as it steers the system towards a single, well defined state.

Obtaining unit fidelity in a complex quantum system is very difficult, whereby a threshold for accepted final fidelity must be agreed on in order to determine the quantum speed limit. The threshold must be variable with the systems size, due to the sensitivity of the fidelity. In [31] a similar optimization was made, and an infidelity threshold of $I_{\text{QSL}} = 10^{-3}$ was set for a 3-site lattice. Adopting the same threshold for the results shown in figure 5.2 yields a quantum speed limit of $T_{\text{QSL}}^{(5)} = 2.7$ for the 5-site lattice.

Further information regarding the control landscape and the consistency of the algorithm can be inferred from the spread in fidelities shown in figure 5.2.a. A large variety of final fidelities may be due to a control landscape with many local minima. On the other hand, the same phenomenon could be caused by the inability of an algorithm to accurately converge to the minimum. The interior point method is a very robust algorithm capable of handling non-linear constraints, whereby it is reasonable to assume the variations in solutions being caused by the underlying control landscape. Considering the fairly large variation in seeds shown in figure 5.1, the control landscape of the 5-site problem must be relatively simple, as the variation in obtained fidelity is rather small.

5.1.4 Optimized Ramp Sequences

A central question is how the optimized ramp sequence differs from its initial seed in both shape and fidelity reached. From figure 5.2 one observes that durations around $T = 2.5$ consistently produce solutions with very high fidelity. The lowest infidelities reached at this duration are around $I \approx 10^{-3}$. Figure 5.3 displays an optimized ramp sequence at duration $T = 2.5$ along with an illustration of the evolution of the system. First, consider

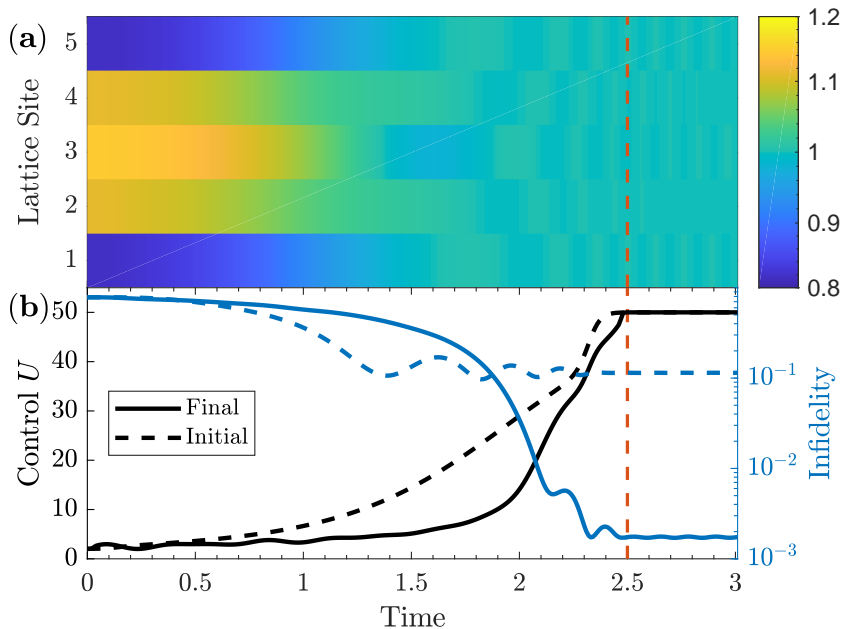


FIGURE 5.3: *Solution with highest fidelity achieved for duration $T = 2.5$. The dashed, red line marks the end of the duration, from which the system is further evolved using the final control value. (a) logarithmically scaled expectation value of the number operator, $\langle \hat{n}_i \rangle$, for each site as the system is evolved according to the optimized ramp. (b) the initial and optimized ramp sequences along with the corresponding evolution of fidelities.*

part 5.3.b in which the initial and optimized control is plotted together with the resulting infidelity. Optimizing the initial seed utilizing the GROUP algorithm has resulted in an increase of two magnitudes in the final fidelity achieved. While the initial ramp is fairly smooth, the optimized ramp wiggles a bit during the first half of the duration followed by a sharp upswing towards the final control value. The steep increase in the control towards the end is very similar to the adiabatic ramp sequence proposed in [81], however, the initial oscillating behavior is non-adiabatic. In fact, examining the optimized ramp sequences for durations shorter than $T = 2.5$ shows an increase in the amplitude of the ramp oscillations, as solutions are required to be increasingly non-adiabatic in order to reach a good fidelity within the given duration. Meanwhile, solutions for durations longer than $T = 2.5$ become increasingly adiabatic. Examples of solutions at various durations can be found in Appendix ???.

After the given optimization duration, T , the final control value is kept constant for an additional time span, where the system is further evolved. Any residual evolution of the system at this point is due to the system not being an eigenstate of the Hamiltonian corresponding to final control value. When examining the initial and final ramp sequence after the optimization duration, the initial control appears to reach a more stable state. However, this is an illusion caused by the logarithmic axis, as the optimized ramp produces a state much closer to the target state, which is set as the ground state of $\hat{H}(U(T))$ through the DMRG algorithm.

Figure 5.3.a illustrates the expectation value of the number operator, $\langle \hat{n}_i \rangle$, for each site during the ramp. Initially the system is in the superfluid state causing a low energetic cost for having multiple particles on each site. Thus, one observes a reduced number of particles at the outer sites of the lattice due to the closed boundary conditions. As the system is

evolved towards the Mott-Insulating state, having multiple particles at the same sites becomes very energetically unfavorable. Hence, the target state has a single particle at each site, as it is deep in the Mott regime. The optimized ramp brings the system very close to this configuration of particles, which can be observed near the dashed red line marking the end of the duration, T . Some imperfections are present, although their magnitude is exaggerated by the logarithmic color axis. The residual oscillations of the infidelity after the optimization durations can be seen in figure 5.3.a as fluctuations of the particle number.

5.1.5 Control Basis Size

Unlike GRAPE, which takes the full optimization space into account, parametrizations like GROUP utilize a chopped basis resulting in a much smaller dimension of the optimization space. When reducing the dimension of the optimization space through a parametrization as described in eq. (2.27), the new control basis must be able to span the solution space. Otherwise artificial minima can be introduced to the control landscape due to the incompleteness of the basis [51]. In the implementation of GROUP used for these calculations, the basis functions of the chopped basis are of the form $f_n = \sin(\omega_n t/T)$, where $\omega_n = n\pi$. These functions constitute the complete set eigenfunctions for the quantum mechanical problem of a particle trapped in a one-dimensional, infinitely deep well. Similarly, the control value is bounded by a constant upper and lower limit, whereby the full sine-basis is capable of describing all solutions. However, in the chopped basis only the M lowest frequencies are used for the parametrization. To investigate the basis size required to describe the optimal solutions, a series of optimizations were made for various basis sizes at the duration $T = 2.5$. The results of the scan over the basis size can be seen in figure 5.4. From figure 5.4.a it

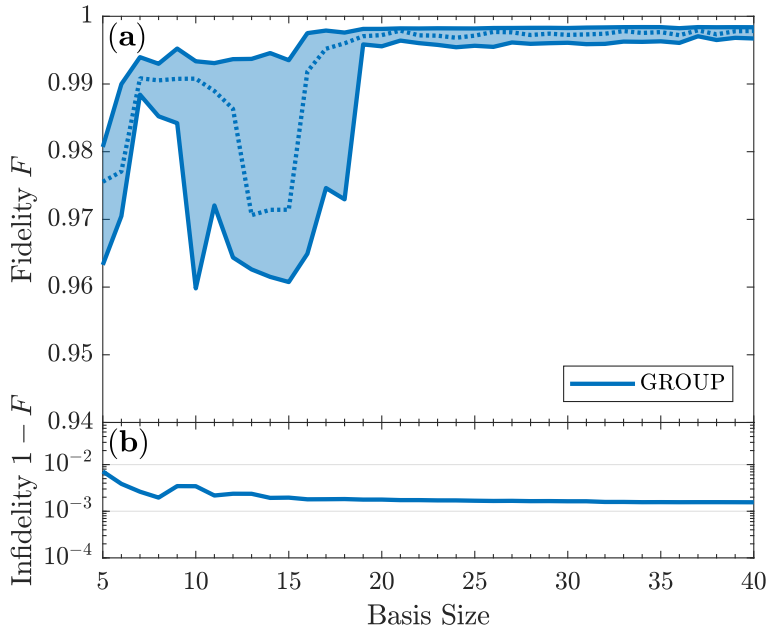


FIGURE 5.4: *Final fidelity obtained for optimal control at various optimization space dimensions for duration $T = 2.5$. (a) the dotted line marks the median fidelity achieved, while the shaded area displays the 25%- and 75%-quartiles of the solutions. (b) the lowest infidelities achieved for each basis size.*

is evident that a basis size of around 20 and above consistently produces high-fidelity solutions, while the quality of solutions using a smaller basis size fluctuated greatly. Thus, high-fidelity ramps for $T = 2.5$ have at least 20 frequency components. Although results obtained with a smaller basis are generally worse, high fidelity solutions are still possible to achieve, as the optimal solution may still be realizable using only few frequencies. This can be observed in figure 5.4.b, where the infidelity of the best solution remains constant, while the median fidelity of the solutions decreases. The large spread in final fidelity is a consequence of a more complicated optimization landscape with artificial minima, which causes the interior point method to converge to non-optimal points.

5.2 Optimal Control of Large Lattice Systems

Bibliography

- [1] Ian Affleck et al. “Rigorous results on valence-bond ground states in antiferromagnets”. In: *Physical review letters* 59.7 (1987), p. 799.
- [2] J. Anandan and Y. Aharonov. “Geometry of quantum evolution”. In: *Phys. Rev. Lett.* 65 (14 1990), pp. 1697–1700. DOI: 10.1103/PhysRevLett.65.1697. URL: <https://link.aps.org/doi/10.1103/PhysRevLett.65.1697>.
- [3] Mike H Anderson et al. “Observation of Bose-Einstein condensation in a dilute atomic vapor”. In: *science* 269.5221 (1995), pp. 198–201.
- [4] RJ Baxter. “Dimers on a rectangular lattice”. In: *Journal of Mathematical Physics* 9.4 (1968), pp. 650–654.
- [5] Immanuel Bloch, Jean Dalibard, and Sylvain Nascimbene. “Quantum simulations with ultracold quantum gases”. In: *Nature Physics* 8.4 (2012), pp. 267–276.
- [6] Immanuel Bloch, Jean Dalibard, and Wilhelm Zwerger. “Many-body physics with ultracold gases”. In: *Rev. Mod. Phys.* 80 (3 2008), pp. 885–964. DOI: 10.1103/RevModPhys.80.885. URL: <https://link.aps.org/doi/10.1103/RevModPhys.80.885>.
- [7] A. Borzì and U. Hohenester. “Multigrid Optimization Schemes for Solving Bose-Einstein Condensate Control Problems”. In: *SIAM Journal on Scientific Computing* 30.1 (2008), pp. 441–462. DOI: 10.1137/070686135. eprint: <https://doi.org/10.1137/070686135>. URL: <https://doi.org/10.1137/070686135>.
- [8] H. Bruus and K. Flensberg. *Many-Body Quantum Theory in Condensed Matter Physics: An Introduction*. Oxford Graduate Texts. OUP Oxford, 2004. ISBN: 9780198566335. URL: <https://books.google.dk/books?id=v5vhg1tYLC8C>.
- [9] T. Caneva et al. “Optimal Control at the Quantum Speed Limit”. In: *Phys. Rev. Lett.* 103 (24 2009), p. 240501. DOI: 10.1103/PhysRevLett.103.240501. URL: <https://link.aps.org/doi/10.1103/PhysRevLett.103.240501>.
- [10] Tommaso Caneva, Tommaso Calarco, and Simone Montangero. “Chopped random-basis quantum optimization”. In: *Physical Review A* 84.2 (2011), p. 022326.
- [11] Tommaso Caneva et al. “Speeding up critical system dynamics through optimized evolution”. In: *Phys. Rev. A* 84 (1 2011), p. 012312. DOI: 10.1103/PhysRevA.84.012312. URL: <https://link.aps.org/doi/10.1103/PhysRevA.84.012312>.
- [12] Claude Cohen-Tannoudji et al. *Atom-photon interactions: basic processes and applications*. Wiley Online Library, 1992.
- [13] Jean Dalibard et al. “Colloquium: Artificial gauge potentials for neutral atoms”. In: *Reviews of Modern Physics* 83.4 (2011), p. 1523.
- [14] P De Fouquieres et al. “Second order gradient ascent pulse engineering”. In: *Journal of Magnetic Resonance* 212.2 (2011), pp. 412–417.

- [15] Patrick Doria, Tommaso Calarco, and Simone Montangero. “Optimal Control Technique for Many-Body Quantum Dynamics”. In: *Phys. Rev. Lett.* 106 (19 2011), p. 190501. DOI: 10.1103/PhysRevLett.106.190501. URL: <https://link.aps.org/doi/10.1103/PhysRevLett.106.190501>.
- [16] J Dukelsky. “J. Dukelsky, MA Martín-Delgado, T. Nishino, and G. Sierra, Europhys. Lett. 43, 457 (1998).” In: *Europhys. Lett.* 43 (1998), p. 457.
- [17] J. Eisert, M. Cramer, and M. B. Plenio. “Colloquium: Area laws for the entanglement entropy”. In: *Rev. Mod. Phys.* 82 (1 2010), pp. 277–306. DOI: 10.1103/RevModPhys.82.277. URL: <https://link.aps.org/doi/10.1103/RevModPhys.82.277>.
- [18] Satoshi Ejima et al. “Characterization of Mott-insulating and superfluid phases in the one-dimensional Bose-Hubbard model”. In: *Phys. Rev. A* 85 (5 2012), p. 053644. DOI: 10.1103/PhysRevA.85.053644. URL: <https://link.aps.org/doi/10.1103/PhysRevA.85.053644>.
- [19] Miroslav Gajdacz et al. “Time-limited optimal dynamics beyond the quantum speed limit”. In: *Phys. Rev. A* 92 (6 2015), p. 062106. DOI: 10.1103/PhysRevA.92.062106. URL: <https://link.aps.org/doi/10.1103/PhysRevA.92.062106>.
- [20] Nathan Gemelke et al. “In situ observation of incompressible mott-insulating domains in ultracold atomic gases”. In: *Nature* 460.7258 (2009), p. 995.
- [21] Markus Greiner. “Ultracold quantum gases in three-dimensional optical lattice potentials”. PhD thesis. 2003. URL: <http://nbn-resolving.de/urn:nbn:de:bvb:19-9683>.
- [22] Rudolf Grimm, Matthias Weidmüller, and Yurii B. Ovchinnikov. “Optical Dipole Traps for Neutral Atoms”. In: ed. by Benjamin Bederson and Herbert Walther. Vol. 42. Advances In Atomic, Molecular, and Optical Physics Supplement C. Academic Press, 2000, pp. 95 –170. DOI: [https://doi.org/10.1016/S1049-250X\(08\)60186-X](https://doi.org/10.1016/S1049-250X(08)60186-X). URL: <http://www.sciencedirect.com/science/article/pii/S1049250X0860186X>.
- [23] E. P. Gross. “Structure of a quantized vortex in boson systems”. In: *Il Nuovo Cimento (1955-1965)* 20.3 (1961), pp. 454–477. ISSN: 1827-6121. DOI: 10.1007/BF02731494. URL: <https://doi.org/10.1007/BF02731494>.
- [24] M. B. Hastings. “An area law for one-dimensional quantum systems”. In: *Journal of Statistical Mechanics: Theory and Experiment* 2007.08 (2007), P08024.
- [25] Ulrich Hohenester et al. “Optimal quantum control of Bose-Einstein condensates in magnetic microtraps”. In: *Physical Review A* 75.2 (2007), p. 023602.
- [26] Garng M Huang, Tzyh J Tarn, and John W Clark. “On the controllability of quantum-mechanical systems”. In: *Journal of Mathematical Physics* 24.11 (1983), pp. 2608–2618.
- [27] Georg Jäger et al. “Optimal quantum control of Bose-Einstein condensates in magnetic microtraps: Comparison of gradient-ascent-pulse-engineering and Krotov optimization schemes”. In: *Physical Review A* 90.3 (2014), p. 033628.
- [28] D. Jaksch and P. Zoller. “The cold atom Hubbard toolbox”. In: *Annals of Physics* 315.1 (2005). Special Issue, pp. 52 –79. ISSN: 0003-4916. DOI: <https://doi.org/10.1016/j.aop.2004.09.010>. URL: <http://www.sciencedirect.com/science/article/pii/S0003491604001782>.
- [29] D. Jaksch et al. “Cold Bosonic Atoms in Optical Lattices”. In: *Phys. Rev. Lett.* 81 (15 1998), pp. 3108–3111. DOI: 10.1103/PhysRevLett.81.3108. URL: <https://link.aps.org/doi/10.1103/PhysRevLett.81.3108>.
- [30] D. Jaksch et al. “Entanglement of Atoms via Cold Controlled Collisions”. In: *Phys. Rev. Lett.* 82 (9 1999), pp. 1975–1978. DOI: 10.1103/PhysRevLett.82.1975. URL: <https://link.aps.org/doi/10.1103/PhysRevLett.82.1975>.

- [31] Maja Juhl and Julie Kryger. “Optimisation Method Development and Testing for Highly Complex Quantum Dynamics”. MA thesis. Department of Physics and Astronomy, Aarhus University, 2018.
- [32] Navin Khaneja et al. “Optimal control of coupled spin dynamics: design of NMR pulse sequences by gradient ascent algorithms”. In: *Journal of magnetic resonance* 172.2 (2005), pp. 296–305.
- [33] C. Kittel. *Introduction to Solid State Physics*. Wiley, 2004. ISBN: 9780471415268. URL: <https://books.google.dk/books?id=kym4QgAACAAJ>.
- [34] Charles Kittel and Ching-yao Fong. *Quantum theory of solids*. Vol. 3. Wiley New York, 1963.
- [35] Walter Kohn. “Analytic properties of Bloch waves and Wannier functions”. In: *Physical Review* 115.4 (1959), p. 809.
- [36] Till D. Kühner, Steven R. White, and H. Monien. “One-dimensional Bose-Hubbard model with nearest-neighbor interaction”. In: *Phys. Rev. B* 61 (18 2000), pp. 12474–12489. DOI: 10.1103/PhysRevB.61.12474. URL: <https://link.aps.org/doi/10.1103/PhysRevB.61.12474>.
- [37] Cornelius Lanczos. “An iteration method for the solution of the eigenvalue problem of linear differential and integral operators”. In: *J. Res. Natl. Bur. Stand. B* 45 (1950), pp. 255–282. DOI: 10.6028/jres.045.026.
- [38] Maciej Lewenstein et al. “Ultracold atomic gases in optical lattices: mimicking condensed matter physics and beyond”. In: *Advances in Physics* 56.2 (2007), pp. 243–379. DOI: 10.1080/00018730701223200. eprint: <https://doi.org/10.1080/00018730701223200>. URL: <https://doi.org/10.1080/00018730701223200>.
- [39] Dong C Liu and Jorge Nocedal. “On the limited memory BFGS method for large scale optimization”. In: *Mathematical programming* 45.1-3 (1989), pp. 503–528.
- [40] S Lloyd and S Montangero. “Information theoretical analysis of quantum optimal control”. In: *Physical review letters* 113.1 (2014), p. 010502.
- [41] L. Mandelstam and Ig. Tamm. “The Uncertainty Relation Between Energy and Time in Non-relativistic Quantum Mechanics”. In: *Selected Papers*. Ed. by Boris M. Bologovskii, Victor Ya. Frenkel, and Rudolf Peierls. Berlin, Heidelberg: Springer Berlin Heidelberg, 1991, pp. 115–123. ISBN: 978-3-642-74626-0. DOI: 10.1007/978-3-642-74626-0_8. URL: https://doi.org/10.1007/978-3-642-74626-0_8.
- [42] Ian P McCulloch. “From density-matrix renormalization group to matrix product states”. In: *Journal of Statistical Mechanics: Theory and Experiment* 2007.10 (2007), P10014.
- [43] Jorge Nocedal and Stephen J. Wright. *Numerical Optimization*. second. New York, NY, USA: Springer, 2006.
- [44] D. van Oosten, P. van der Straten, and H. T. C. Stoof. “Quantum phases in an optical lattice”. In: *Phys. Rev. A* 63 (5 2001), p. 053601. DOI: 10.1103/PhysRevA.63.053601. URL: <https://link.aps.org/doi/10.1103/PhysRevA.63.053601>.
- [45] Stellan Östlund and Stefan Rommer. “Thermodynamic limit of density matrix renormalization”. In: *Physical review letters* 75.19 (1995), p. 3537.
- [46] Anirban Pathak. *Elements of quantum computation and quantum communication*. Taylor & Francis, 2013.
- [47] Oliver Penrose and Lars Onsager. “Bose-Einstein Condensation and Liquid Helium”. In: *Phys. Rev.* 104 (3 1956), pp. 576–584. DOI: 10.1103/PhysRev.104.576. URL: <https://link.aps.org/doi/10.1103/PhysRev.104.576>.

- [48] Christopher J Pethick and Henrik Smith. *Bose-Einstein condensation in dilute gases*. Cambridge university press, 2002.
- [49] L.P. Pitaevskii. “Vortex Lines in an Imperfect Bose Gas”. In: *Soviet Physics JETP* 13.2 (1961), pp. 451–454.
- [50] M. Plischke and B. Bergersen. *Equilibrium Statistical Physics*. World Scientific, 2006. ISBN: 9789812560483. URL: <https://books.google.dk/books?id=KYu7igYEkhwC>.
- [51] Niklas Rach et al. “Dressing the chopped-random-basis optimization: A bandwidth-limited access to the trap-free landscape”. In: *Physical Review A* 92.6 (2015), p. 062343.
- [52] Viswanath Ramakrishna et al. “Controllability of molecular systems”. In: *Physical Review A* 51.2 (1995), p. 960.
- [53] Stuart Alan Rice, Meishan Zhao, et al. *Optical control of molecular dynamics*. John Wiley, 2000.
- [54] Robert Robere. *Interior Point Methods and Linear Programming*. 2012.
- [55] Subir Sachdev. *Quantum phase transitions*. Wiley Online Library, 2007.
- [56] M. Saffman, T. G. Walker, and K. Mølmer. “Quantum information with Rydberg atoms”. In: *Rev. Mod. Phys.* 82 (3 2010), pp. 2313–2363. DOI: [10.1103/RevModPhys.82.2313](https://doi.org/10.1103/RevModPhys.82.2313). URL: <https://link.aps.org/doi/10.1103/RevModPhys.82.2313>.
- [57] Sonia G Schirmer, H Fu, and Allan I Solomon. “Complete controllability of quantum systems”. In: *Physical Review A* 63.6 (2001), p. 063410.
- [58] Ulrich Schollwöck. “The density-matrix renormalization group in the age of matrix product states”. In: *Annals of Physics* 326.1 (2011). January 2011 Special Issue, pp. 96 –192. ISSN: 0003-4916. DOI: <https://doi.org/10.1016/j.aop.2010.09.012>. URL: <http://www.sciencedirect.com/science/article/pii/S0003491610001752>.
- [59] Norbert Schuch et al. “Entropy Scaling and Simulability by Matrix Product States”. In: *Phys. Rev. Lett.* 100 (3 2008), p. 030504. DOI: [10.1103/PhysRevLett.100.030504](https://doi.org/10.1103/PhysRevLett.100.030504). URL: <https://link.aps.org/doi/10.1103/PhysRevLett.100.030504>.
- [60] Moshe Shapiro and Paul Brumer. “Principles of the quantum control of molecular processes”. In: *Principles of the Quantum Control of Molecular Processes, by Moshe Shapiro, Paul Brumer, pp. 250. ISBN 0-471-24184-9. Wiley-VCH, February 2003.* (2003), p. 250.
- [61] Jonathan Simon et al. “Quantum simulation of antiferromagnetic spin chains in an optical lattice”. In: *Nature* 472.7343 (2011), pp. 307–312.
- [62] Jens Jakob WH Sørensen et al. “Exploring the quantum speed limit with computer games”. In: *Nature* 532.7598 (2016), p. 210.
- [63] I. B. Spielman, W. D. Phillips, and J. V. Porto. “Condensate Fraction in a 2D Bose Gas Measured across the Mott-Insulator Transition”. In: *Phys. Rev. Lett.* 100 (12 2008), p. 120402. DOI: [10.1103/PhysRevLett.100.120402](https://doi.org/10.1103/PhysRevLett.100.120402). URL: <https://link.aps.org/doi/10.1103/PhysRevLett.100.120402>.
- [64] E. Miles Stoudenmire and Steven R. White. *ITensor Library*. URL: <http://itensor.org/index.html>.
- [65] Masuo Suzuki. “General theory of fractal path integrals with applications to many-body theories and statistical physics”. In: *Journal of Mathematical Physics* (1991).
- [66] Leticia Tarruell et al. “Creating, moving and merging Dirac points with a Fermi gas in a tunable honeycomb lattice”. In: *Nature* 483.7389 (2012), pp. 302–305.

- [67] S Van Frank et al. “Optimal control of complex atomic quantum systems”. In: *Scientific reports* 6 (2016).
- [68] G. Vidal. “Classical Simulation of Infinite-Size Quantum Lattice Systems in One Spatial Dimension”. In: *Phys. Rev. Lett.* 98 (7 2007), p. 070201. DOI: 10.1103/PhysRevLett.98.070201. URL: <https://link.aps.org/doi/10.1103/PhysRevLett.98.070201>.
- [69] Guifré Vidal. “Efficient classical simulation of slightly entangled quantum computations”. In: *Physical review letters* 91.14 (2003), p. 147902.
- [70] Guifré Vidal. “Efficient simulation of one-dimensional quantum many-body systems”. In: *Physical review letters* 93.4 (2004), p. 040502.
- [71] Gregory Von Winckel and A Borzì. “Computational techniques for a quantum control problem with H1-cost”. In: *Inverse Problems* 24.3 (2008), p. 034007.
- [72] Andreas Wächter. “Short Tutorial: Getting Started With Ipopt in 90 Minutes”. In: *Combinatorial Scientific Computing*. Ed. by Uwe Naumann et al. Dagstuhl Seminar Proceedings 09061. Dagstuhl, Germany: Schloss Dagstuhl - Leibniz-Zentrum fuer Informatik, Germany, 2009. URL: <http://drops.dagstuhl.de/opus/volltexte/2009/2089>.
- [73] Andreas Wächter and Lorenz T Biegler. “On the implementation of an interior-point filter line-search algorithm for large-scale nonlinear programming”. In: *Mathematical programming* 106.1 (2006), pp. 25–57.
- [74] J Werschnik and EKU Gross. “Quantum optimal control theory”. In: *Journal of Physics B: Atomic, Molecular and Optical Physics* 40.18 (2007), R175.
- [75] Steven R White. “Density-matrix algorithms for quantum renormalization groups”. In: *Physical Review B* 48.14 (1993), p. 10345.
- [76] Steven R. White. “Density matrix formulation for quantum renormalization groups”. In: *Phys. Rev. Lett.* 69 (19 1992), pp. 2863–2866. DOI: 10.1103/PhysRevLett.69.2863. URL: <https://link.aps.org/doi/10.1103/PhysRevLett.69.2863>.
- [77] Steven R. White. “Density matrix renormalization group algorithms with a single center site”. In: *Phys. Rev. B* 72 (18 2005), p. 180403. DOI: 10.1103/PhysRevB.72.180403. URL: <https://link.aps.org/doi/10.1103/PhysRevB.72.180403>.
- [78] Artur Widera. “Constructing correlated spin states with neutral atoms in optical lattices”. PhD thesis. Ph. D. thesis, Johannes Gutenberg-Universität, Mainz, 2008.
- [79] R. M. Wilcox. “Exponential Operators and Parameter Differentiation in Quantum Physics”. In: *Journal of Mathematical Physics* 8.4 (1967), pp. 962–982. DOI: 10.1063/1.1705306. eprint: <https://doi.org/10.1063/1.1705306>. URL: <https://doi.org/10.1063/1.1705306>.
- [80] William K Wootters. “Statistical distance and Hilbert space”. In: *Physical Review D* 23.2 (1981), p. 357.
- [81] Jakub Zakrzewski and Dominique Delande. “Breakdown of adiabaticity when loading ultracold atoms in optical lattices”. In: *Physical Review A* 80.1 (2009), p. 013602.
- [82] Michael P. Zaletel et al. “Time-evolving a matrix product state with long-ranged interactions”. In: *Phys. Rev. B* 91 (16 2015), p. 165112. DOI: 10.1103/PhysRevB.91.165112. URL: <https://link.aps.org/doi/10.1103/PhysRevB.91.165112>.
- [83] J. M. Zhang and R. X. Dong. “Exact diagonalization: the Bose-Hubbard model as an example”. In: *European Journal of Physics* 31 (May 2010), pp. 591–602. DOI: 10.1088/0143-0807/31/3/016. arXiv: 1102.4006 [cond-mat.stat-mech].

- [84] Dmitry V Zhdanov and Tamar Seideman. “Role of control constraints in quantum optimal control”. In: *Physical Review A* 92.5 (2015), p. 052109.

Appendix A

Example: Quantum Speed Limit in Landau-Zener Model

To illustrate concepts from quantum optimal control theory, a state transfer within the Landau-Zener model is optimized using the GRAPE algorithm.

The Landau-Zener model is a two-level system with the general Hamiltonian

$$\hat{H}_{\text{LZ}} = \begin{pmatrix} \Delta(t) & \Omega_R \\ \Omega_R & -\Delta(t) \end{pmatrix} = \Omega_R \hat{\sigma}_x + \Delta(t) \hat{\sigma}_z , \quad (\text{A.1})$$

where Ω_R is the positive Rabi-frequency, $\Delta(t)$ is the detuning, and $\hat{\sigma}_i$ are the Pauli spin matrices. In such a system the detuning will be the control parameter, as it is easily to manipulate in an experimental setup. An advantage of the Landau-Zener system is that an analytical solution to the control problem exists for arbitrary initial and final states. Two level systems can be illustrated on the Bloch sphere, which depicts the population of the two levels along with the relative phases. Consider the transfer between the initial state

$$|\psi_0\rangle = \cos\left(\frac{\theta_0}{2}\right)|0\rangle + e^{i\phi_0} \sin\left(\frac{\theta_0}{2}\right)|1\rangle \quad (\text{A.2})$$

and final state

$$|\psi_T\rangle = \cos\left(\frac{\theta_T}{2}\right)|0\rangle + e^{i\phi_T} \sin\left(\frac{\theta_T}{2}\right)|1\rangle , \quad (\text{A.3})$$

which are both expressed in terms of the angles of the Bloch sphere. In CITE the quantum speed limit of such a state transfer was derived to be

$$T_{\text{QSL}} = \left| \frac{\theta_T - \theta_0}{2\Omega_R} \right| . \quad (\text{A.4})$$

Consider the case of $|\psi_0\rangle = |0\rangle$ and $|\psi_T\rangle = |1\rangle$, whereby the quantum speed limit is $T_{\text{QSL}} = \frac{\pi}{2\Omega_R}$.

Optimal control using GRAPE

In this example $\Omega_R = 1$ for simplicity. Examining the Hamiltonian of eq. (A.1), it is clear that the state transfer $|0\rangle \rightarrow |1\rangle$ can be achieved efficiently by letting $u(t) \equiv \Delta(t) = 0$ for the entire duration. To avoid this the control is subjected to the boundary conditions $u(0) = 0$ and $u(T) = 2T$.

Figure A.1 displays the results of optimizing the state transfer using the GRAPE algorithm for duration $T_1 = \pi/2$. The algorithm takes an initial linear seed, which clearly does not reach the target state. Clearly, the optimized control achieves perfect transfer. This is as expected, as the quantum speed limit for the transfer is $T_{\text{QSL}} = T_1 = \pi/2$, whereby a solution should exist for this duration. However, any duration shorter should not be

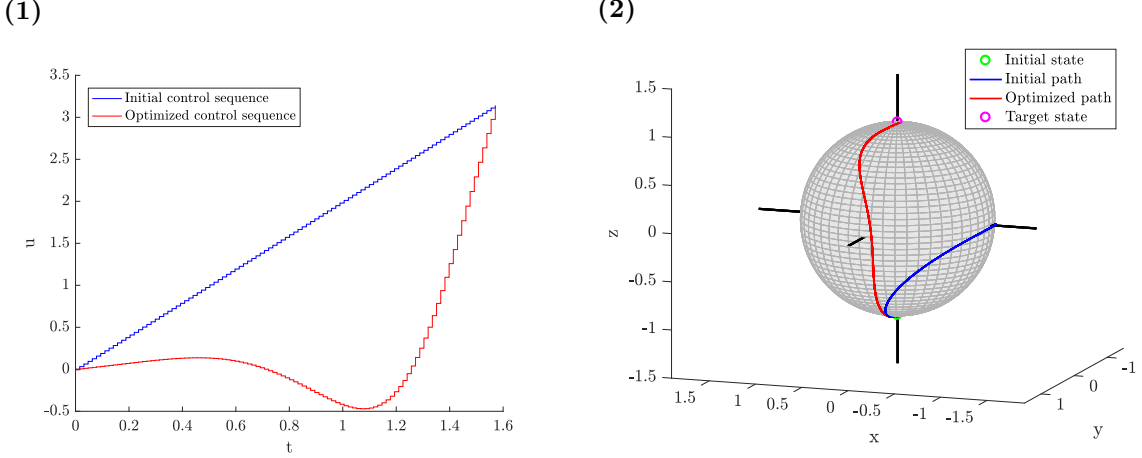


FIGURE A.1: *Optimal control of LZ-system using GRAPE for $T_1 = \pi/2$.* (a): Initial and optimized control sequence. (b): Path traced out on the Bloch sphere by the quantum state, as it is evolved according to the control.

sufficient to reach the target state.

Next, consider figure A.2, which shows the optimization results for duration $T_2 = 2$. As

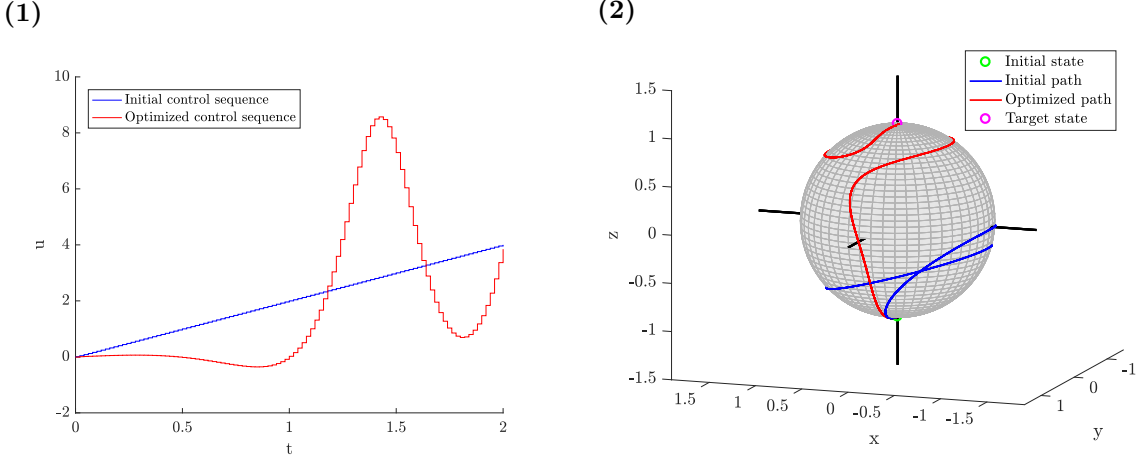


FIGURE A.2: *Optimal control of LZ-system using GRAPE for $T_2 = 2$.* (a): Initial and optimized control sequence. (b): Path traced out on the Bloch sphere by the quantum state, as it is evolved according to the control.

this duration is larger than the quantum speed limit, a solution exist for T_2 . However, the path of the state on the Bloch sphere is much less direct than for the previous case. This is a consequence of how the optimal control is formulated, as one is searching for a control resulting in $|\psi(T)\rangle = |\psi_{\text{Target}}\rangle$. Thus, the path of state has no impact on the cost.

For large duration solutions to the control problem generally become more abundant CITE. Figures A.1 and A.2 illustrate this point, as many different paths from $|\psi_0\rangle \rightarrow |\psi_{\text{Target}}\rangle$ are possible for large durations, whereas only few possible solutions are available at durations close to the quantum speed limit.

Appendix B

Diagrammatic Representation of Matrix Product States

Due to the many indices, equations describing contractions of matrix product states are often quite hard to read. Therefore, the equations are often represented graphically through diagrams. Many variations of diagrams exists, however, they all follow some general rules:

- Tensors are represented by nodes.
- Indices are represented by lines. Horizontal lines are *bond indices*, while vertical lines are *physical indices*.
- Tensors connected by a line are contracted over said bond.

Through these basic rules, most equations involving matrix product states can be expressed through diagrams. In this instance, the color or shape of a node provides information regarding the properties of the tensor. Therefore, the tensors shown in this thesis follow these guidelines:

- Tensors part of an MPS are square-like. The color of the tensor denotes its normalisation, as shown in figure B.1. These different types of normalisation are the essence of MPS canonical forms (see Section 3.3).
- Tensors part of MPO's are grey and circular/elliptical depending on the number of sites they span over. These tensors have two vertical legs compared to the one leg of the MPS tensors.
- Matrices (tensors without any physical index) are depicted as a diamond. These often occur after a singular value decomposition.

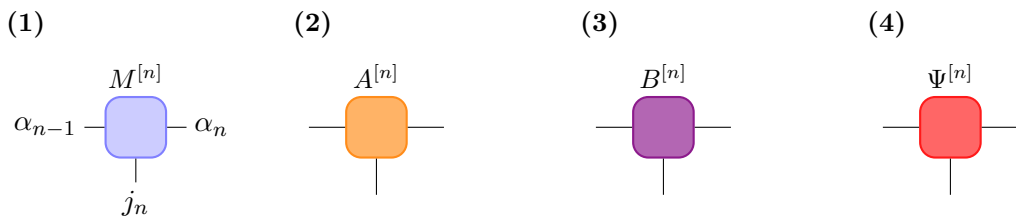


FIGURE B.1: The four different types of MPS tensors used in diagrams. (i) General tensor of unspecified normalisation. The indices corresponding to the tensor are labeled. The remaining tensors are: Left-normalised (ii), right-normalised (iii), central cite (iv).

Appendix C

Example: Building an MPO from a Hamiltonian

Consider the Bose-Hubbard Hamiltonian , which consists of both nearest-neighbour tunneling terms and on-site interactions terms

$$\hat{H} = -J \sum_{\langle i,j \rangle} \hat{a}_i^\dagger \hat{a}_j + \frac{U}{2} \sum_i \hat{n}_i (\hat{n}_i - 1) . \quad (\text{C.1})$$

The Hamiltonian can be expressed as a sum of strings of operators - most of these being identities just like in equation 3.27. Moving through such a string from the right, one will at some point encounter one of 3 non-trivial operators. This can be summarized as 4 different possible states of the string of operators on a given bond:

1. Only identities to the right of the bond.
2. An \hat{a}^\dagger operator just to the right of the bond.
3. An \hat{a} operator just to the right of the bond.
4. A completed tunneling or the interaction term, $\frac{U}{2}\hat{n}(\hat{n}-1)$, somewhere to the right.

When moving through the string of operators from the right, only certain transitions between these state are possible. For instance **1** → **1**, where one starts in state 1, and the next operator is an identity. Likewise, **1** → **2, 3, 4** are all possible, since these transitions represent the next operator being non-trivial. Next, **2** → **4** completes the hopping $-J\hat{a}^\dagger\hat{a}$ - a similar transition exists for the other hopping term **3** → **4**. Finally, the transition **4** → **4** is needed to continue iterating through the operator chain after having passed the non-trivial operators. This can be encoded in the operator-valued matrix

$$W^{[i]} = \begin{pmatrix} \hat{I} & 0 & 0 & 0 \\ \hat{a}^\dagger & 0 & 0 & 0 \\ \hat{a} & 0 & 0 & 0 \\ \frac{U}{2}\hat{n}(\hat{n}-1) & -J\hat{a} & -J\hat{a}^\dagger & \hat{I} \end{pmatrix} , \quad (\text{C.2})$$

which contains all the allowed transitions between the five state [58]. When one starts moving through the operator chain from the right side, one obviously begins in state 1 and ends in state 4. This can be encoded in the two vectors

$$\vec{v}_{left} = (0, 0, 0, 1) , \quad \vec{v}_{right} = (1, 0, 0, 0)^T .$$

Thus, the Bose-Hubbard Hamiltonian can be written as an MPO

$$\hat{H} = \sum_{j,j'} \vec{v}_{left} W^{[1]j_1,j'_1} W^{[2]j_2,j'_2} \dots W^{[N]j_N,j'_N} \vec{v}_{right} |j\rangle \langle j'| . \quad (\text{C.3})$$

Often, the two closing vectors are implicitly multiplied unto the outer matrices for a cleaner notation. Observe how all of this was done without having to do a single numerical computation. The resulting MPO can now readily be applied to an MPS.

Appendix D

Calculation of Condensate Fraction using DMRG Algorithm

To illustrate the power of the DMRG algorithm, the following numerical analysis was conducted. As the system of interest is the Bose-Hubbard model described in eq. (1.39), a suitable benchmark for the algorithm is attempting to calculate the critical point of the phase transition between the superfluid and Mott-Insulator. The critical point was determined using the DMRG algorithm in [36] by studying the correlations of the system. Here, an alternative approach is presented, which examines the condensate fraction. According to the Penrose-Onsager criterion, a system is in the superfluid phase if and only if the largest eigenvalue, λ_1 , of the single-particle density matrix, $\rho^{(1)}$, is macroscopic

$$f_c = \frac{\lambda_1}{N_p} > 0 , \quad (\text{D.1})$$

where f_c is the condensate fraction, and N_p is the total number of particles [47]. The condensate fraction can be used to determine which phase dominates the system, as

$$\lim_{N_p \rightarrow \infty} f_c^{\text{SF}} \rightarrow 1 \quad (\text{D.2})$$

$$\lim_{N_p \rightarrow \infty} f_c^{\text{MI}} \rightarrow 0 , \quad (\text{D.3})$$

when the filling-fraction, $n = N_p/L$, is held constant.

To calculate the condensate fraction, the ground state of the system was found using a version of the DMRG algorithm implemented in the ITensor library [64]. Using the computed ground state, $|\psi\rangle$, the entries of the density matrix were calculated

$$\rho_{i,j}^{(1)} = \langle \psi | \hat{a}_i^\dagger \hat{a}_j | \psi \rangle . \quad (\text{D.4})$$

Lastly, the condensate fraction was determined through eq. (D.1). The calculation was performed with varying U/J for various system sizes of unit occupancy. The DMRG algorithm was set to perform 5 sweeps with a maximum bond dimension of 200. In order to gauge the accuracy of the algorithm, the results for system sizes 4-10 were compared to a similar calculation using exact diagonalisation. The upper part of figure D.1 shows the condensate fraction for various U/J calculated using the DMRG algorithm. In the limit $U/J = 0$, the condensate fraction is unit for the smaller systems, confirming the system is indeed in the superfluid phase. The condensate fraction never reaches zero as U/J increases, since this is only achieved in the thermodynamic limit. However, the condensate fraction does decrease with increasing particle number, as would be expected. The lower half of figure D.1 displays the results of the DMRG calculation compared with exact diagonalisation. For small systems the two approaches obtain very similar results.

Attempting to use exact diagonalisation for large systems is futile, due to the exponential

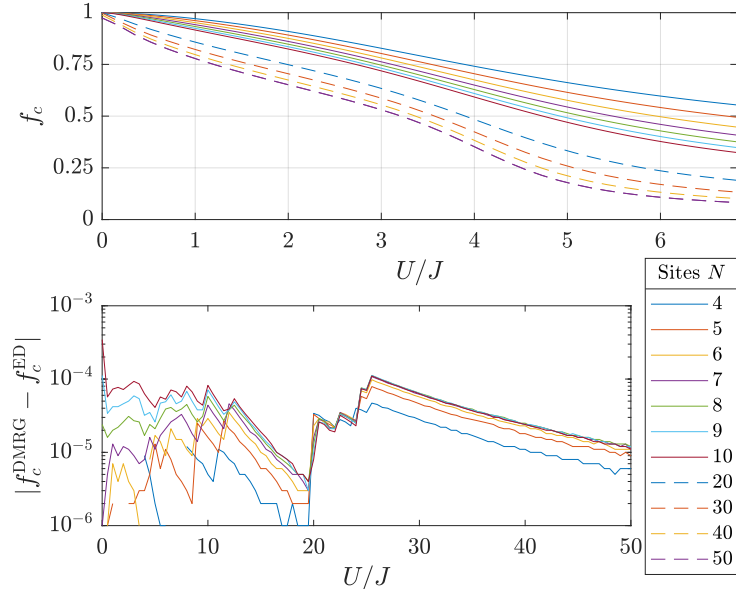


FIGURE D.1: Condensate fraction calculated using the DMRG algorithm with 20 sweeps. The condensate fractions of the smaller systems ($L = 4 \dots 10$) are compared with result obtained through exact diagonalisation.

scaling of the Hilbert space [69]. However, this is not an issue using matrix product states, as the formalism only considers a tiny corner of the Hilbert space by following an area law. The dashed lines of figure D.1 shows the results of the DMRG calculations for up to 50 particles. The condensate fraction behaves as expected in the $U/J \gg 1$ limit, as it tends towards zero for larger particle numbers. Note, in the superfluid limit the condensate fraction does not quite reach 1, which is due to difficulty of describing long-range correlations when using matrix product states as described in section ???. This is not an issue for smaller systems, as the correlation length is limited by the system size.

Some measures can be taken to minimize errors, when using the DMRG algorithm. Accurately describing long range correlations requires multiple sweeps, as the algorithm has to iteratively approximate an almost constant function with a series of exponentials. Figure D.2 displays the condensate fraction in the Superfluid limit as a function of number of sweeps. Clearly, performing more sweeps yields a better result. Furthermore, increasing

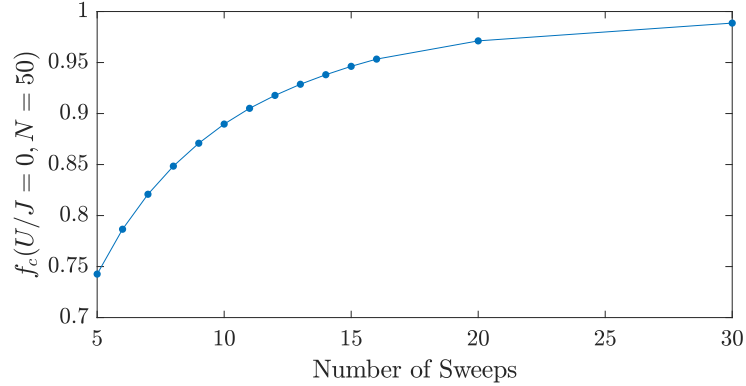


FIGURE D.2: Condensate fraction as a function of number of sweeps of the DMRG algorithm in the superfluid limit. A max bond dimension of $D = 250$ was used.

the maximal bond dimension, D , results in a more accurate long-range representation of

correlations. Thus, calculating correlation functions for various values of D is a great way of estimating the convergence of the correlations for a given length scale [58].

In [36] the critical point of phase transition between the Superfluid and Mott-Insulator is determined as $(\frac{U}{J})_{crit} = 3.37$. The result is achieved through examining the correlations of the systems. While correlations in Mott-Insulators decay exponentially, superfluids have a decay of correlations following the power-law given in eq. (3.6). The interface between the two phases has correlations following a power law determined by the Luttinger liquid parameter. The critical point, which is located at the tip of the Mott-lobes, is computed by determining the point at which the Luttinger liquid parameter is $K = \frac{1}{2}$ [36].

Examining figure D.1, one notices a hump on the graph in the vicinity of the critical ratio, but no clear indication of a phase transition is present. In the thermodynamic limit one would expect the condensate fraction to drop to zero as the critical ratio is reached (as observed in 2D by [63]). However, at 50 particles the condensate fraction is only around $f_c = 0.5$. One could extrapolate data from computations using different particle numbers in order to determine the location of the critical point. However, this would require computations using larger systems in order to minimize the boundary effects.